

UNCLASSIFIED

SECURITY CLASSIFICATION OF THIS PAGE

REPORT DOCUMENTATION PAGE

AD-A204 262

IC
CTE
D

1b. RESTRICTIVE MARKINGS

UIC FILE COPY

2b. DECLASSIFICATION / DOWNGRADING

FEB 17 1989

3. DISTRIBUTION / AVAILABILITY OF REPORT
Approved for public release,
distribution unlimited

(2)

4. PERFORMING ORGANIZATION REPORT NUMBER(S)

CUKD/C-MATS/TR148

D_{CS}

5. MONITORING ORGANIZATION REPORT NUMBER(S)

AFOSR-TR- 89-0108

6a. NAME OF PERFORMING ORGANIZATION
Cambridge University
Engineering Department6b. OFFICE SYMBOL
(If applicable)

7a. NAME OF MONITORING ORGANIZATION

AFOSR/NA

6c. ADDRESS (City, State, and ZIP Code)

Trumpington Street, Cambridge, CB2 1PZ
England

7b. ADDRESS (City, State, and ZIP Code)

AFOSR/PKZ, Building 410, Bolling AFB,
Washington DC 20332-64488a. NAME OF FUNDING / SPONSORING
ORGANIZATION
BOARD8b. OFFICE SYMBOL
(If applicable)

9. PROCUREMENT INSTRUMENT IDENTIFICATION NUMBER

AFOSR-87-0307

8c. ADDRESS (City, State, and ZIP Code)

Same as
7b.

10. SOURCE OF FUNDING NUMBERS

PROGRAM
ELEMENT NO.PROJECT
NO.TASK
NO.WORK UNIT
ACCESSION NO.

61100F

2382

[REDACTED]

[REDACTED]

11. TITLE (Include Security Classification)

DIRECT OBSERVATIONS OF FRACTURE AND THE DAMAGE MECHANICS OF CERAMICS (U)

12. PERSONAL AUTHOR(S)

G Vekinis, M F Ashby and P W R Beaumont

13a. TYPE OF REPORT
Interim13b. TIME COVERED
FROM 87/9/1 TO 88/8/3114. DATE OF REPORT (Year, Month, Day)
88/10/3115. PAGE COUNT
124

16. SUPPLEMENTARY NOTATION

17. COSATI CODES

FIELD GROUP SUB-GROUP

18. SUBJECT TERMS (Continue on reverse if necessary and identify by block number)

Ceramics, Alumina, Fracture, R-curve, Scanning Electron
Microscopy, In-situ observations, Damage Mechanics, Uniaxial
and Hydrostatic compression, Plaster of Paris, Modeling

19. ABSTRACT (Continue on reverse if necessary and identify by block number)

An experimental study of the R-curve behaviour of an Alumina ceramic by in-situ SEM has yielded detailed information on the extent of the R-curve in this material as well as on the actual physical mechanisms responsible for the toughness increase. These have been identified as both ligamentary bridging due to crack bifurcation and bridging by wedged grains between the crack faces which dissipates energy by friction. Simple modelling calculations show that these mechanisms can account for the 75% increase in toughness observed using the double torsion technique.

Further, the feasibility of Plaster of Paris as a model ceramic material for damage mechanic investigations has been examined and extensive mechanical property characterization has been carried out. The initiation and final fracture surfaces have been constructed from uniaxial+ hydrostatic compression and uniaxial tension and the results have been compared with new theoretical models for fracture initiation. The failure characteristics have been studied by in-situ SEM.

20. DISTRIBUTION / AVAILABILITY OF ABSTRACT

☒ UNCLASSIFIED/UNLIMITED ☒ SAME AS RPT. ☒ DTIC USERS

21. ABSTRACT SECURITY CLASSIFICATION

UNCLASSIFIED

22a. NAME OF RESPONSIBLE INDIVIDUAL
Colonel George Haritos22b. TELEPHONE (Include Area Code)
202-767-046322c. OFFICE SYMBOL
NA

DD FORM 1473, 84 MAR

83 APR edition may be used until exhausted.
All other editions are obsolete.

SECURITY CLASSIFICATION OF THIS PAGE

UNCLASSIFIED

89 2 16 088

031221 1041

Air Force Office of Scientific Research
United States Air Force

Grant AFOSR-87-0307

An Interim Scientific Report
1 September 1987 - 31 August 1988

DIRECT OBSERVATION OF FRACTURE AND THE
DAMAGE MECHANICS OF CERAMICS

G Vekinis, M F Ashby and P W R Beaumont

Engineering Department
Cambridge University
Trumpington Street
Cambridge, CB2 1PZ, England.
CUED/C-MATS/TR 148. October 1988.

031221 1041

SUMMARY

The project research activities concentrated on three main aspects:

(1) Literature survey of published work on the experimental and theoretical aspects of fracture of brittle materials under compression and the R-curve behaviour of ceramics.

(2) The development of SEM techniques for in-situ dynamic observation of fracture in ceramics. The emphasis of this part of the work was on the investigation of the fracture micromechanics of ceramics and in particular the influence of microstructural parameters on the shape of the R-curve of 96% Al_2O_3 and the determination of the physical mechanisms responsible for the R-curve behaviour in non-transforming ceramics. The direct observation of the wake processes taking place between the crack faces during crack propagation, showed conclusively that R-curve behaviour, at least in this material, is due to very extensive grain bridging behind the crack tip. By considering the energy dissipation characteristics of various possible bridging mechanisms, it was shown that the major contribution to the stress intensity increase observed appears to be due to wedged grains expending energy against friction as the crack faces separate. It was also shown that the contribution of the elastic bending of bridging ligaments created by crack-bifurcation, to the energy dissipation is very small.

(3) The investigation of the fracture and damage micromechanics of CaSO_4 as a model ceramic material with the aim of elucidating the micromechanics of compressive fracture in brittle materials. To this end, the properties of Plaster of Paris specimens were extensively investigated, and the failure initiation and final failure surfaces have been constructed and compared with the predictions of new theoretical models. The micromechanics of fracture have been investigated with the aid of in-situ SEM investigations.



Accession For	
NTIS CRA&I	<input checked="" type="checkbox"/>
DTIC TAB	<input type="checkbox"/>
Unannounced	<input type="checkbox"/>
Justification	
By	
Distribution /	
Availability Codes	
Dist	Avail and/or Special
A-1	

CONTENTS

Page

SUMMARY	
CONTENTS	
INTRODUCTION	1
PART 1: DIRECT OBSERVATION OF FRACTURE IN Al_2O_3 CERAMICS AND THEIR R-CURVE BEHAVIOUR.	
1.1. Review of R-curve behaviour of non-transforming ceramics.	5
1.2. Experimental aspects.	15
1.2.1. The material.	15
1.2.2. The Double-Torsion technique.	16
1.2.3. Grain growth studies.	20
1.3. In-situ observation of fracture and the R-curve behaviour of 96% Al_2O_3 .	22
1.3.1. General considerations.	22
1.3.2. Dynamic observation of fracture processes in the SEM.	24
1.3.3. The R-curve behaviour of 96% Al_2O_3 .	25
1.4. Discussion.	33
PART 2: COMPRESSIVE FRACTURE OF CERAMICS	
2.1. Fundamentals of compressive fracture of brittle materials and related theoretical developments.	43
2.2. Review of compressive fracture of ceramics.	57
2.3. Experimental study of the failure characteristics of a model brittle material.	65
2.3.1. The material.	65
2.3.2. The mechanical and elastic properties of the material.	70
2.3.3. The failure surface.	86
2.3.4. In-situ optical and SEM observations of fracture under compression and the compressive failure characteristics of $\text{CaSO}_4 \cdot \frac{1}{2} \text{H}_2\text{O}$.	95
PLANS FOR FUTURE WORK.	102
ACKNOWLEDGEMENT	102
REFERENCES	103
APPENDIX	110

INTRODUCTION

The fracture and failure characteristics of ceramics under tensile stresses have been studied extensively in the past. A large body of work exists which attempts to relate the bulk fracture properties of ceramics such as fracture toughness, crack propagation resistance, delayed fracture, etc, to their microstructural parameters such as grain size, grain contiguity, defect size, microcrack size and distribution and residual stresses (e.g. [1-17]).

During the past two decades a number of important phenomena relating to the fracture of ceramics have been observed and are being studied with the aim of understanding the physical processes of fracture of brittle materials and their influence on fracture toughness. Examples are:

(1) The R-curve behaviour of non-transforming ceramics, in particular that of Al_2O_3 [12,13,18-34]. A physical understanding of the observed increase in fracture toughness with increasing crack length will provide critical insight into the microstructural aspects of strength and critical flaw management. The incorporation of this knowledge into manufacturing processes will no doubt aid the attempts at improving the flaw tolerance of ceramics. The present work has attempted to address this question by direct observation of the fracture process in an SEM.

(2) The various toughening mechanisms which exist in some ceramic materials such as microcracking, phase transformation and crack-tip plasticity. These have been investigated extensively (e.g. [1,2,4,7,18,22,35-39] and a great deal of progress has been achieved in understanding the various physical processes involved and their incorporation into manufacturing processes.

(3) Delayed fracture in some ceramic systems, most notably the alumina system [e.g. 1,2,4,40-44]. This has been shown to be related to subcritical crack growth during which the crack grows at crack tip stress intensity values, K_I , significantly lower than the critical stress intensity K_{IC} (fracture toughness) of the material. Understanding the physical mechanisms underlying this phenomenon will aid in the explanation of a number of time-dependent fracture effects that have been observed in ceramics.

The successful explanation of various fracture phenomena and processes such as these, require an in-depth understanding of the dynamic development and propagation of cracks under load. To this end, part of the present study deals with the direct observation of crack initiation and propagation in a scanning electron microscope. The experiments involve the controlled loading of ceramic specimens during SEM observation on instrumented rigs specifically designed for particular loading conditions. Each experiment can be recorded on video tape and important parameters can be measured directly or calculated subsequently such as crack tip opening displacement, crack length, crack path characteristics, crack velocity, defect size and crack-defect interactions, microcrack initiation and interaction. Since the rigs are instrumented with calibrated load cells, the stress-strain characteristics of the specimen and the influence of the fracture processes on them can be calculated directly as well as the crack tip stress intensity during the fracture process.

Whereas the great majority of fracture investigations of ceramics have dealt with fracture under tensile stresses, relatively little has been reported on the compressive fracture characteristics of ceramic [84-90], although the compressive failure of brittle materials in general has been dealt with in the past e.g. [61-65, 72-80]. Unlike tensile fracture, where a single most severe flaw initiates a crack which propagates unstably to cause complete failure, compressive fracture is a stable process, i.e. energy input is required to propagate the crack(s). Only two attempts at modelling compressive fracture of brittle materials can be found in the literature: a phenomenological model mainly due to Costin [69-71] and the physical model of Ashby and co-workers [66-68]. The direct observation of the fracture processes that take place during compression of brittle materials will aid greatly the understanding of their compressive failure characteristics. This has been initiated in the present work using both model ceramic materials and standard structural ceramics.

The research carried out during the first year of the work has concentrated on three main aspects:

- (1) Literature survey of, (a): crack path analysis during tensile fracture

of ceramics and specifically of R-curve behaviour of Al_2O_3 based ceramics and (b): theoretical and experimental developments in the field of the compressive fracture of brittle materials and specifically ceramics, with emphasis on the micromechanics of compressive fracture.

(2) In-situ investigations of fracture processes in Al_2O_3 ceramics and their R-curve behaviour. The existing in-situ SEM facilities of the Materials Group were extensively modified and new rigs were designed and built in order to carry out Double Torsion (DT) and Double Cantilever Beam (DCB) slow fracture experiments on ceramic specimens. The in-situ facilities have enabled accurate measurements of the crack length and high magnification studies of the crack path and the physical processes which give rise to the "closure stress" between the crack faces during fracture have been identified. By considering the energetics of each of the possible processes, it was possible to determine the most likely sources of the energy dissipation observed.

(3) Modelling of compressive fracture of ceramics using CaSO_4 as a model brittle material. CaSO_4 was chosen due to its inherent high degree of brittleness combined with its ease of manufacture and the possibility of incorporating flaws of known distribution. Extensive characterization was carried out: the processing parameters and environmental effects were investigated in detail to ensure reproducibility of properties, and the mechanical and elastic properties of the materials were measured to ascertain the structure-property relationships. The main body of this part of the work involved the measurement of the compressive properties of the material such as Young's modulus in compression, the uniaxial, hydrostatic and axisymmetric compressive strength and the identification of the fracture processes during compression. The results have been compared with predictions of the damage mechanics models that have been developed recently for brittle materials [66-68,82] and a new model has been proposed for fracture initiation of brittle materials containing spherical flaws under hydrostatic compression. The investigations of the fracture mechanisms during compression were carried out by in-situ SEM.

The main emphasis of the work planned for the future is on the completion of the above tasks and on investigations of fracture and damage mechanics of ceramics under compression. To that end extensive preparatory work has been carried out in designing and building equipment for in-situ SEM uniaxial compression investigations as well as for hydrostatic and axisymmetric compression experiments.

PART 1: DIRECT OBSERVATION OF FRACTURE IN Al_2O_3 CERAMICS AND THEIR R-CURVE BEHAVIOUR.

1.1 Review of R-curve behaviour of non-transforming ceramics.

The term R-curve refers to the increase of the fracture surface energy, R , of a material, with increasing crack length i.e. the resistance to crack propagation of the material apparently increases with increasing crack length. The equilibrium condition is usually obtained by equating R to the mechanical energy release rate G , derived from the work done by the applied loading during crack extension. This phenomenon has been predominantly studied in the case of relatively ductile materials such as metals and fiber-reinforced composites (see e.g. [3]), but a number of investigations during the past decade [12-39] have shown that an equivalent increase in crack propagation resistance with increasing crack length is displayed by ceramic materials, especially ceramics that can undergo toughness-enhancing martensitic transformations during fracturing, such as Partially Stabilized Zirconia, as well as non-transforming polycrystalline ceramics such as the Alumina system.

Whereas the toughening phenomenon observed in the transformation toughening ceramics has been partly explained by considering the energy dissipation in the transformation process, the observations reported on the fracture resistance characteristics of non-transformable ceramics have not been successfully explained as yet.

The first systematic observations of R-curve behaviour in non-transforming ceramics were reported in 1977 by Hubner and Jillek [19] who were studying sub-critical crack growth in pure Al_2O_3 samples by 4-point bending. They found that the stress intensity factor per unit crack extension increases considerably with increasing crack extension. They related the observed increase in fracture resistance with the equivalent phenomenon found in other materials and explained their observations by assuming multiple crack formation and interference of the fracture surfaces due to the angular

development of the crack front. A few years later, a number of workers [12-15] found indirect evidence for the phenomenon. Evans and co-workers [20-22] attempted to explain the toughness increase observed by considering the dissipation of energy during the nucleation and growth of numerous microcracks around the propagating crack tip as well as the effect of a "process-zone wake" behind the crack tip due to the associated stress/strain hysteresis.

In 1982, Knehans and co-workers [23,24] studied the R-curve behaviour exhibited by pre-notched pure polycrystalline alumina specimens loaded in 3-point bending. They investigated the influence of notch depth, specimen geometry, mean grain size and deformation rate on the behaviour of the crack resistance. They reported that R increased by up to a factor of 4 within one specimen and that no unique R-curve exists for that material. Furthermore, they found that the slope of the R-curve was significantly affected by notch depth and they concluded that this "notch-depth" memory of the crack cannot be explained in terms of any energy dissipation mechanisms in front or around the crack tip. By cutting away material behind the crack tip, they showed conclusively that the phenomenon observed must be due to events occurring behind the crack tip over a distance of the order of millimetres. As possible explanations for the increase in crack resistance (but not of the notch-depth effect) they suggested that consideration should be given to friction of serrated crack walls or the presence of microcracks in the volume close to the crack walls.

In 1985, Cook and co-workers [25] carried out a systematic investigation of the inert strength characteristics of ceramics (concentrating on aluminas) as a function of indentation crack size relative to grain size. On progressively decreasing the indentation load, the strengths (measured under both biaxial and uniaxial bending conditions) first showed a steady increase, but subsequently tended to a plateau, as the contact size began to approach the characteristic grain size. By postulating the existence of a "microstructural driving force", they analysed the data in terms of an apparent R-curve function using a simple extension of conventional indentation fracture mechanics theory incorporating residual contact stresses. They found that, for

large flaws, the strengths tend to an ideal $-1/3$ power law dependence on indentation load, which suggested a constant toughness. At small crack sizes however, the strengths decrease markedly and tend to a load-independent plateau. Their study emphasized the need for more information into the underlying physical processes actually responsible for the microstructural driving forces (especially at the weak grain boundaries which are responsible for the intergranular fracture mode observed). Their analysis cautions against the indiscriminate extrapolation of strength data obtained by large crack-length techniques to the microcrack regime.

Swain [26] has reported on the extent of the R-curve behaviour by using a Double Cantilever Beam method to measure the stress intensity factor of pure Al_2O_3 specimens of the same batch as that used by Steinbrech et al [24]. The use of DCB specimens enabled the measurement of the R-curve behaviour over a longer crack length than previously reported. He found that the "wake zone" over which crack bridging occurs for this material extends up to 8mm behind the crack tip as shown in fig.1.1., i.e. the stress intensity factor was observed to increase to a steady-state value (the fracture toughness) over a distance of approximately 8 mm. As a possible explanation for the phenomenon he proposed that the crack bridging is due to compressional thermal-expansion anisotropy stresses exhibited by larger than average grains intersected by the propagating crack. This of-course cannot explain the notch-depth effect or some of the other observations reported.

In 1987, Swanson and co-workers [27] reported the results of optical microscopic examinations of the crack paths in coarse-grained alumina specimens loaded under tapered cantilever beam and indented flexure conditions. They found that the fractures were highly stable (indicative of strong R-curve behaviour) but discontinuous at the microstructural level due to grain-localized bridging across the newly formed crack interface. They suggested the existence of "activity sites" along the crack with a spacing of 2 to 5 grain diameters consisting of overlapping segments around bridging grains. They theorised that these segments link-up with the primary crack beneath the specimen surface and continue to evolve toward rupture of the

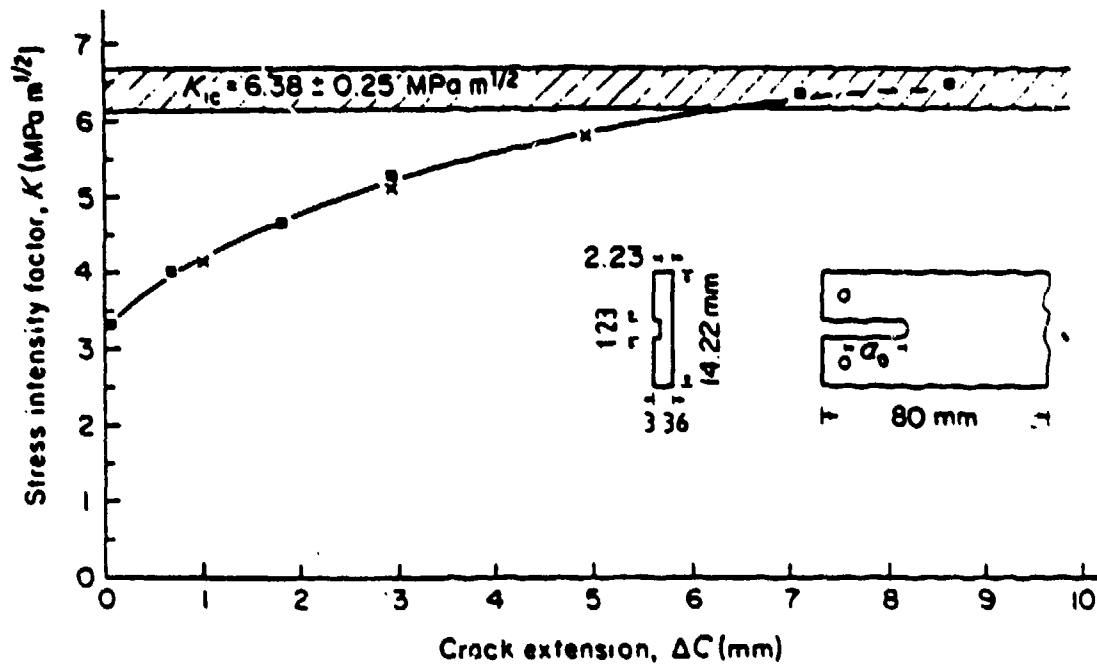


Fig.1.1.R-curve behaviour of coarse-grained AD96 alumina as reported by Swain [26]. The hatched region is the steady-state K_{IC} value for stable extension of large cracks. (x) 1st notch, $a_0 = 10.8 \text{ mm}$, (•) 2nd notch, $a_0 = 19 \text{ mm}$.

bridge as fracture proceeds (the same physical process has also been conclusively identified in the present work, see later). By carrying out post-fracture scanning electron microscopy they found that interface-adjacent microfracture and frictional tractions were important aspects of the bridging process. They were unable to find evidence for frontal-zone microcracking and crack-tip/internal-stress interaction which, as mentioned, have been postulated as possible sources for the energy dissipation.

Following on from that work, Mai and Lawn [28], developed a fracture mechanics model to explain their observations. They treated the increased crack resistance as the cumulative effect of grain-bridging restraints operating behind the crack tip and used a discrete distribution function for the crack-plane restraining stresses. They assumed that a general expression for the net stress intensity factor for a crack in equilibrium is:

$$K = K_a + \sum K_i = T_o \quad 1.1a$$

$$\text{or: } K_a = T = T_o - \sum K_i \quad 1.1b$$

where:

K_a is the contribution from the applied loading,

K_i represent contributions from the discrete internal forces acting on the crack,

T_o is the intrinsic material toughness (i.e. the effective K_{Ic} for bulk cleavage or grain boundary fracture) independent of crack size, and

$T = T(c)$ the effective toughness function which has replaced the traditional R .

By considering the stability criterion for a propagating crack under these conditions and assuming that the K_i functions are positive decreasing functions of the crack size, they used the Green's function solution for line cracks to represent the microstructure associated stress intensity factor

along the crack as:

$$K_{\mu} = 0 \quad (d_0 > c) \quad 1.2a$$

$$K_{\mu} = -(2\tau/\pi)c^{1/2} \int_{d_0}^c p(x)/(c^2-x^2)^{1/2} dx \quad (d_0 \leq c \leq c^*) \quad 1.2b$$

$$K_{\mu} = -(2\tau/\pi)c^{1/2} \int_{d_0+c-c^*}^c p(x)/(c^2-x^2)^{1/2} dx \quad (c > c^*) \quad 1.2c$$

where: c = the distance from the mouth to the front of the crack,

d = mean separation between "closure force centres",

d_0 = distance to the first bridge from the specimen edge,

τ = crack geometry term = $\pi^{1/2}$ for sharp line cracks,

$p(x)$ = approximate continuous closure stress function replacing the discrete force function due to the bridges $p(x)$ and $\tau = p(x)/d^2$, and

c^*-d_0 = extent of the bridging region.

Since the function $p(x)$ is unknown, they replaced it by $p(u(x))$ where u is the crack opening displacement and used the far-field solution for a slit-like crack in equilibrium ($K = T_0$):

$$u(x,c) = (\sqrt{8\tau}T_0/\pi E)(c-x)^{1/2} \quad 1.3$$

where E is the Young's modulus, and a trial stress separation function:

$$p(u) = p^*(1-u/u^*)^m \quad (0 \leq u \leq u^*) \quad 1.4$$

where p^* and u^* are limiting values of the stress and separation respectively and m is an exponent. It must be noted that since $p(0) = 0$, this form of the separation function is incorrect for low values of u (near the crack tip)-important in the case of brittle fiber-reinforced composites, but may be used to represent p at larger values of u . The exponent m reflects the way p is distributed over the bridging zone: $m=0$ represents a uniformly distributed

stress, $m=1$ represents the stress in the case of a frictional grain pullout mechanism and $m=2$ is used for fiber-reinforced concrete.

By substitution of equations 1.3 and 1.4 into equations 1.2 and 1.1 they finally obtained the form of the effective toughness function, T , in terms of the parameters T_0 , T_∞ , c^* , d_0 and m (transforming the coordinates such that $c=c_0+\Delta c$ and $d_0=c_0+d$, where c_0 is the notch length):

$$T(\Delta c) = T_0 \quad (d > \Delta c) \quad 1.5a$$

$$T(\Delta c) = T_\infty - (T_\infty - T_0) \{1 - [(\Delta c - d)/(\Delta c^* - d)]^{1/2}\}^{m+1} \quad (d \leq \Delta c \leq \Delta c^*) \quad 1.5b$$

$$T(\Delta c) = T_\infty \quad (\Delta c > \Delta c^*) \quad 1.5c$$

where

$$T_\infty = \text{fracture toughness of the material (plateau region)} = T_0 + E p^* u^* / (m+1) T_0$$

$$c^* = d_0 + (\pi E u^* / 2\sqrt{2} T_0)^2$$

$$\Delta c^* = \text{steady state bridging zone length} = d + (\pi E u^* / 2\sqrt{2} T_0)^2$$

Thus the T equations and the spatial extent, Δc^* , are geometry insensitive.

They accordingly used these modelling equations to compare with the results of Swain [26] on 99% Al_2O_3 and found that a good fit was obtained for $m=0$ with T_0 and T_∞ used as regression variables as shown in fig.1.2. They calculated that those data gave $p^* \approx 25$ MPa for $m=0$ and $p^* u^* / (m+1) =$ work per unit area to separate the bridges ≈ 20 J/m² which is comparable with fracture surface energies and thus demonstrated consistency between calculated and measured R-(or T-)curve behaviour for that material. Finally, although they emphasized that caution should be exercised in using these best fit procedures for generating the parameters, they nevertheless suggested that these parameters could be used in materials characterization and design especially in strength analysis where short crack configurations are important.

The above model has been used to analyse the results obtained in the present work on the R-curve behaviour of 96% Al_2O_3 but the results do not fully support the model predictions, as discussed later.

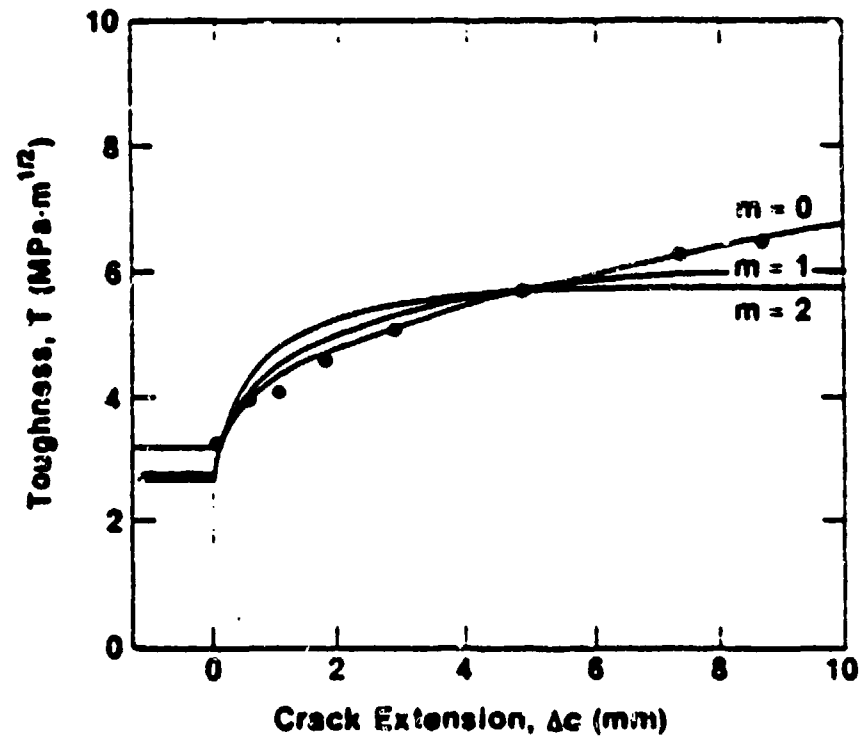


Fig.1.2. Fit of Swain's results [26] (shown in fig.1.1) and theoretical model predictions of Mai and Lawn as presented by Mai and Lawn [28].

Soon afterwards Cook et al [29] applied the Mai and Lawn model to the mechanics of the indentation strength test and in particular to the measurements of Cook et al [25]. They found that materials with pronounced T-curves (as they call the R-curves) have the qualities of flaw tolerance and enhanced crack stability. They suggested that the indentation-strength methodology in combination with the bridging model could be used in the development and characterization of structural ceramics particularly with regard to grain boundary structure (since most observations of R-curve behaviour have been carried out on intergranularly fracturing material).

The R-curve behaviour of Al_2O_3 three-point bend specimens at high temperatures has been reported by Wieninger et al [30] who found that the toughness increase was much steeper at temperatures above 1000°C , although their measurements only extended for 2-3mm. They attributed the effect to "friction effects" and "adhesive forces" behind the crack tip.

During the past year a number of studies have been reported on the R-curve behaviour of ceramics dealing with the determination of the curve details as well as the evaluation of the crack bridging stress. Steinbrech and Schmenkel [31] studied "naturally-occurring" flaws on the surface of alumina bend specimens and found that they displayed R-curve behaviour but with lower initial R values than found in the case of longer cracks in SENB specimens. They suggested that this could be due to the influence of surface residual stresses.

Hsueh and Becher [32] presented a simple approach to calculating the bridging stresses by starting with the experimentally determined R-curve and evaluating empirically the bridging stress instead of assuming the existence of the force-crack-opening relation as used by Mai and Lawn. They assumed that the pre-crack length is much longer than the bridging zone and that the bridging stress maintains a constant profile as the crack propagates and found that the bridging stress can be represented in terms of the derivative of the

R-curve $dK/d\ell$:

$$\begin{aligned} p(x) &= (\pi x/2)^{1/2} (dK/d\ell) & (0 \leq x = \ell \leq \ell_0) & & 1.6a \\ p(x) &= 0 & (x = \ell \text{ or } x = \ell > \ell_0) & & 1.6b \end{aligned}$$

where ℓ is the crack extension.

Application of their technique to SiC-whisker-reinforced Al_2O_3 indicated that the bridging stress has a maximum value within a short distance behind the crack tip decreasing to 0 or leveling off to a finite value at the end of the bridging zone, depending on the nature of the R-curve behaviour.

Krause [33] reported measurements of R-curve behaviour in coarse-grained 96% Al_2O_3 by measuring the strengths of indented 4-point bend specimens against indentation crack size for both as-sintered and annealed specimens. His results are at variance with the results of the similar experiments of Cook et al [25] in that he did not find the $-1/3$ dependence reported by Cook et al. He pointed out that if the lowest load point of Cook et al was excluded from their work their results would be easily described by a straight line.

Finally, Reichl and Steinbrech [34] reported the results of a novel experiment to illustrate conclusively the existence of the bridging stress behind the crack tip. They used notched short double cantilever beam specimens to show that, if a second notch is introduced at the back face of the specimen, then, when the crack reaches that notch under very stable crack propagation conditions, the specimen still retains load carrying capacity wholly due to the bridging ligaments. They succeeded in measuring the load at that point and thus were able to calculate the actual magnitude of the bridging stress. Their experimentally determined value of ≈ 30 MPa ($\approx 1/7$ of the flexure stress indicates that about 14% of the zone area is effectively ligamented which agrees with the results obtained in the present work) agrees with theoretically determined values of $p(x)$ and the best-fit value of 25 MPa calculated by Mai and Lawn [28].

1.2. Experimental aspects.

1.2.1. The material

The material chosen for these investigations was an Al_2O_3 -glass matrix ceramic : ADS96R provided by COORS Ceramics, Wales. It is a grade used extensively in the electronics industry as substrate material and (as grade AD96) as a wear resistant material in valves and pipelines in the coal mining industry. It consists of 96wt% Al_2O_3 in a $\text{MgO-SiO}_2\text{-Al}_2\text{O}_3$ glass matrix. Some of the properties of the material as provided by the manufacturers (and measured in this work) are tabulated in Table 1.1.

Table 1.1 Properties of the ADS96R specimens as supplied by the manufacturers (COORS Ceramics, Wales).

Physical properties.

Al_2O_3 content, wt %	96
Density, kg/m^3	3.75 (3.74*)
Porosity, %, open	0
total	≈ 0.5
Grain size, μm , range	2-35 (2-12*)
mean	7 (4.1*)
Coefficient of thermal expansion, $^\circ\text{C}^{-1}$	6.3×10^{-6}

Elastic and Mechanical properties.

Young's modulus, GPa	303
Shear modulus, GPa	124
Bulk modulus, GPa	172
Poisson's ratio	0.21
Modulus of rupture (3-point), MPa	399
Compressive strength, MPa	2070
Hardness, GPa	11.1 (11.4*)
Fracture toughness, $\text{MPa}\sqrt{\text{m}}$	2.3 ± 0.2 *

* : measured in this work.

The specimens were manufactured by a rolling process for use as electronic substrates and thus were provided in a final thickness of $0.64 \pm 0.01\text{mm}$. This enabled the use of the specimens directly without the necessity of cutting and grinding which always introduce surface residual stresses. This was an important consideration since residual stresses are known to influence significantly the crack propagation resistance of most materials (see for example [45]). The morphology of the microstructure of the material is shown in fig.1.3. The fracture mode of the material is predominantly transgranular as shown clearly in fig.1.4 where brittle fracture of the glass phase is clearly visible as well. This agrees with the findings of Mussler and co-workers [13] for pure alumina of the same grain size. Some workers however have reported predominantly intergranular fracture surfaces for even larger grain-sized pure alumina e.g.[26].

1.2.2. The double torsion technique.

The majority of the techniques used in the measurement of the fracture toughness of ceramic materials have a crack length dependence on K_I [95] which necessitates the measurement of the crack length during testing or the making of a number of assumptions about the crack length characteristics. The Double-Torsion (DT) technique however, has been shown by compliance analysis [48], to be a "constant K" technique, i.e. the stress intensity K is independent of the crack length (assuming that there is no crack tip shielding or other crack path-related effect on the total stress intensity).

The technique was first introduced by Outwater and Gerry [46] and was subsequently developed by Kies and Clark [47] and later by Williams and Evans [48] and Pletka and co-workers [49]. The early developments showed that the crack velocity was constant for a constant load and that there was good correlation between crack length derived from compliance analysis and that measured by direct methods. A schematic diagram showing the typical specimen shape and loading configuration (used in this work) is shown in fig.1.5. The side groove is cut onto the specimen in order to facilitate straight crack propagation. The stress intensity K_I under this loading geometry (assuming

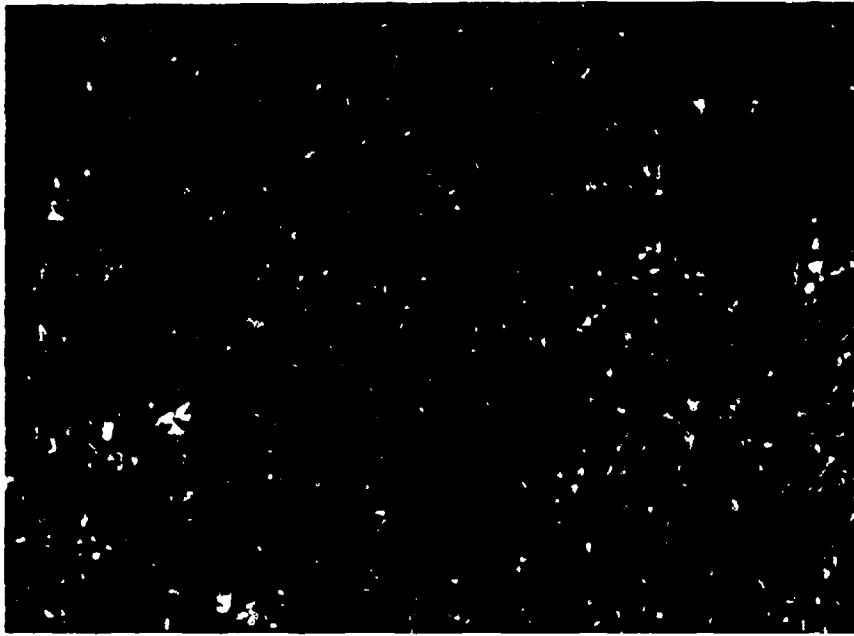


Fig.1.3.Morphology of the ADS96R alumina used in his work. Optical micrograph x1000.



Fig.1.4. Typical fracture surface of ADS96R illustrating the transgranular fracture mode. Fracture of the glass phase is also visible.

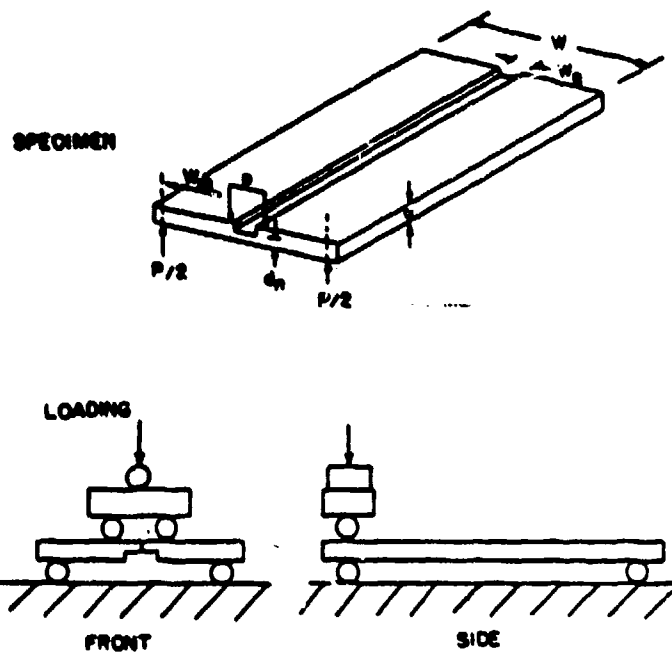


Fig.1.5. Schematic diagram illustrating specimen and loading geometry of the double torsion specimen as utilised by Pletka et al [49] and in this work.

plane strain conditions at the crack tip) is given by [48,50]:

$$K_I = PW_m \left[\frac{3}{Wd^3d_n(1-\nu)\xi} \right]^{1/2} \quad 1.7$$

where P = the load

ν = Poisson's ratio

W_m, W, d, d_n = geometric parameters defined in fig. 1.5.

$\xi = 1 - 0.6302t + 1.20te^{-\pi/t}$ = a correction factor for thick specimens [49]
($t = 2d/W$).

The critical stress intensity factor K_{IC} (fracture toughness) can be calculated using equation 1.7 when fracture is entirely mechanical, i.e. by carrying out the test at relatively high strain-rates [48,50].

The technique has been used widely because of a number of other advantages other than the independence of K_I on crack length : the loading configuration is very simple and lends itself to testing at high temperatures or hostile environments or in-situ measurements (such as those used in this work). Also, the sample preparation is particularly simple and lends itself to routine use. The utilization of compressive loading, as compared to tensile loading needed in other tests such as the DCB configuration, makes the DT technique ideal for slow crack growth investigations. This can be carried out by a load-relaxation experiment or by an incremental method and since the crack velocity, v , is related to the instantaneous load and the corresponding load relaxation rate, it can be measured over a range of K_I [48,50,51].

A number of questions have been raised as to whether the mode of fracture in the double torsion specimen is indeed Mode I, but Evans and co-workers [48,50] showed that the correlation between G_c values measured by other techniques with values calculated using the analysis given above support the conclusion that DT specimens fail in Mode I fracture.

The crack front of the double torsion specimen is curved and extends further along the tensile surface than the compressive surface. Michalske and co-workers [52] showed by measuring the crack velocity as a function of the

position along the crack front, that the crack front shape remains constant over the load plateau region. They showed also that this satisfies the assumption that $\partial A / \partial \ell$ = thickness, where A = crack surface area and ℓ = crack extension which is central to the analysis of the DT technique. In addition, the range of K_I along a DT crack front was nearly equal to the experimental scatter in a double-cantilever-beam type test which agrees with the findings of Evans [50].

Because of the stability of crack propagation, the simple loading geometry and the capability of long crack lengths the DT technique lends itself very easily to R-curve behaviour investigations. This has been done in the present work by using a specially designed rig in a scanning electron microscope. The K_I at various crack lengths was determined using eqn.1.7 by following the loading procedure discussed later.

1.2.3. Grain growth studies.

In order to study the influence of grain size on the R-curve characteristics of the material, specimens with different average grain size were prepared by aging ADS96R specimens at 1500°C and 1550°C. for varying periods of time. The average grain size was determined by the linear intercept method over a large number of grains. The results obtained are plotted in fig.1.6. against \sqrt{t} according to the grain growth relation [53]:

$$d^2 = d_0^2 + \frac{Ct}{T} \exp(-Q/RT) \quad 1.8$$

where:

d_0 = initial grain size.

T = Temperature,

Q = activation energy and

C = a constant dependent on the surface energy.

The present report deals with the results obtained on specimens with a small difference in grain size (up to 1.5 variation) but these will be extended in the near future to include specimens with coarser grain structure.

Effect of aging on grain size of ADS96R

21

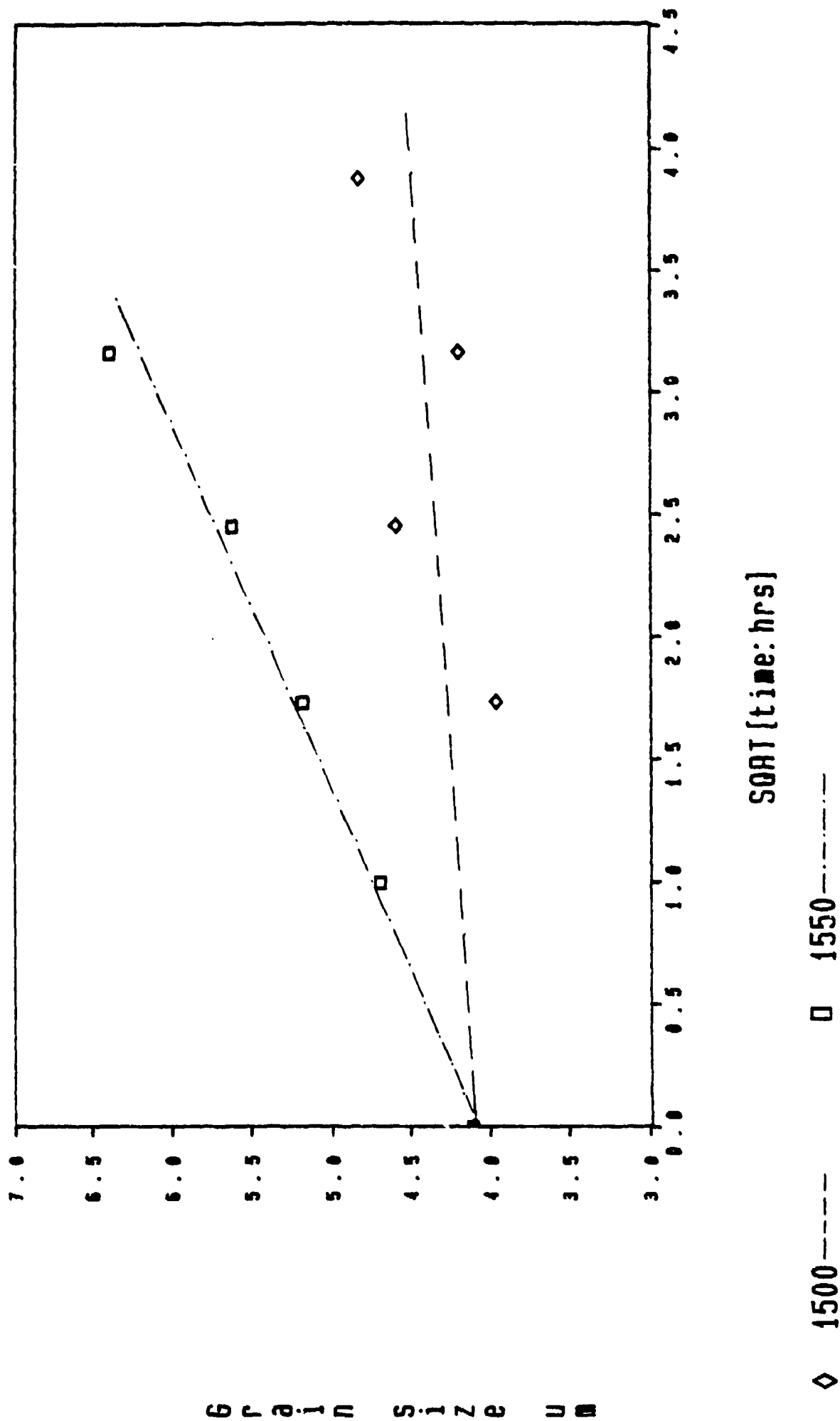


Fig.1.6.Effect of aging at 1500 °C and 1550 °C on the average grain size of ADS96R.

1.3. In-situ dynamic observations of fracture in 96% Al_2O_3 by DT and its R-curve behaviour.

1.3.1. General Considerations.

Understanding of the micromechanics of the fracture process can be aided substantially by observing dynamically the actual mechanics of crack propagation. In this way a large number of questions pertaining to the fracture process can be successfully addressed and the various theories on the fracture micromechanics and failure modes can be tested. For this reason we have developed an in-situ facility for fracturing specimens under various loading conditions and has used it successfully for investigating the fracture process of polymeric composites and other materials [54-56]. This facility has now been improved by the development of further loading configurations (such as a high stress compression rig) and the stiffening of the existing rigs to enable the investigation of the fracture processes of very rigid materials such as ceramics. The only other similar rig described in the literature was used by Wu and co-workers [57] to study the character of cracks in conjunction with an X-ray microradiographic technique but it did not have any capability for dynamic testing and observation of crack growth dynamics but only for static observation under load.

Due to the simplicity of the loading configuration and the stability of crack propagation in the double torsion technique, the in-situ SEM investigations of crack propagation and R-curve behaviour of 96% Al_2O_3 were carried out using the DT configuration in a specially constructed instrumented 4-point rig shown in fig.1.7. This is the first time that this technique has been used to investigate the R-curve behaviour of ceramics. The majority of the work reported in the literature involved the use of either a 3-point bend specimen (which limits one to very short crack lengths) or the double cantilever beam technique which, although it allows measurements of K_I at long crack lengths, is dependent on accurate measurement of the crack length for the calculation of K_I . In addition, this is the first time that the crack length has been measured very accurately using a scanning electron microscope during loading.



Fig.1.7. The double-torsion testing rig used for in-situ dynamic testing in an SEM.

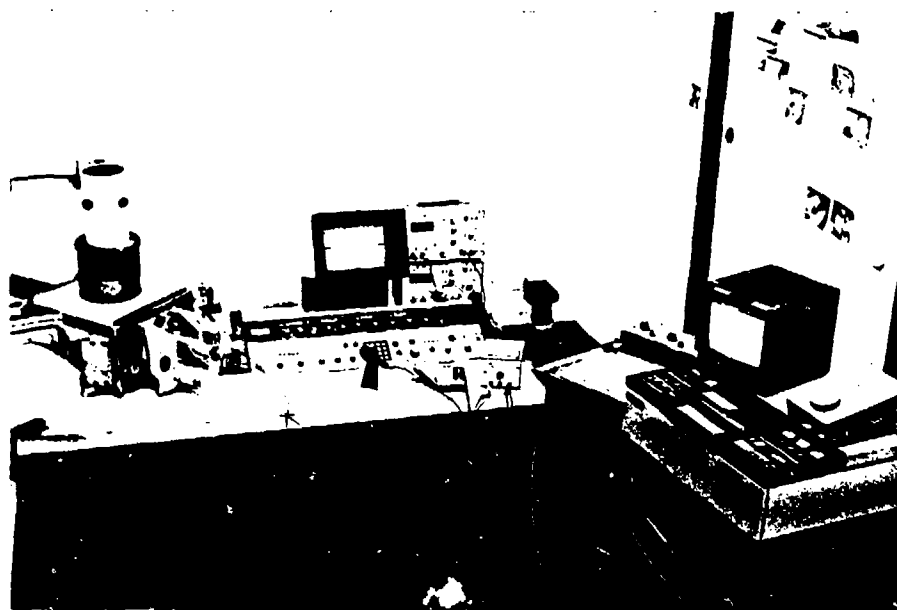


Fig.1.8. The in-situ testing arrangement showing the SEM, the strain gauges, the recorder, the power supply and the video equipment.

The rig is instrumented for both stress and strain using strain gauges with capabilities for loading at a wide range of strain-rates via two reducers connected to a DC motor. The experiments are recorded on video tape which enables the direct correlation of physical events with variations in load etc and subsequent detailed study of the physical processes involved. The rig and accompanying equipment used during testing is shown in fig.1.8.

The DT specimens used were cut from the substrate material to a final size of approximately 25x55mm, were grooved along one side using a 0.4mm diamond wheel and a narrow notch was cut using a 0.15mm high speed diamond wheel with the geometry suggested by Pletka and co-workers [49]. Following notching, an initial crack was introduced by driving a small wedge into the notch. The loading conditions as suggested by Pletka and co-workers [49] were followed in all experiments and the loading-rate was varied from approximately 10 μ m/min in the case of the crack path observations up to approximately 50 μ m/min for the measurements of K_I in the R-curve studies. The specimens were very accurately aligned in the rig and preloaded to approx. 20% of maximum load prior to the start of the experiments. The loading symmetry between the sides of the specimens was monitored continuously during the tests to ensure straight crack propagation (which was not always achieved). For the R-curve investigations only the undeviated portion of the cracks was used in the calculations. Furthermore, in a number of cases the crack initiated by popping-in to a length of few mm and thus not all specimens in the R-curve studies yielded results in the low-crack length regime. Even with the strictest alignment and monitoring procedures only about 30% of the specimens used for the R-curve tests yielded acceptable results due to either a very long pop-in crack or too-early crack deviation.

1.3.2. Dynamic observations of fracture in ADS96R Al₂O₃.

Using the in-situ rig described above with the DT configuration it has been possible to monitor the growth and propagation of cracks through the material very accurately (practically "grain by grain") in conjunction with the video

recordings. Although it is not possible to fully describe these observations using "still" photographs, the salient features of the observations can nevertheless be easily appreciated.

The crack was observed in all cases to be particularly straight and transgranular, deviating or becoming intergranular only on interaction with particularly small grains or when grain boundaries were encountered at a small angle to the crack path. This is illustrated in fig.1.9. where the sequence of photographs show the advancing transgranular crack meeting a low-angle grain boundary resulting in deviation and subsequent return to a transgranular fracture mode.

Extensive crack bifurcation was observed in all specimens and some examples are shown in fig.1.10. This phenomenon has been observed before and is believed to be one of the bridging mechanisms involved in R-curve behaviour by providing a larger real fracture surface area than that calculated from the apparent crack length. This is discussed with more examples in the next section. Some, but by no means extensive, secondary microcracking was also observed propagating from the primary crack and one example is shown in fig 1.11.

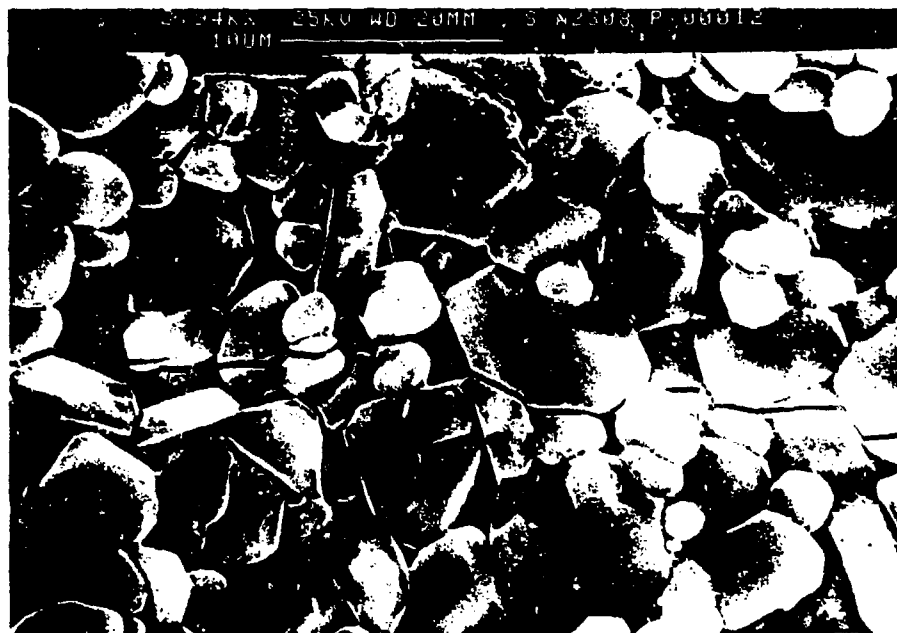
Elastic crack tip closure was observed in all specimens by reducing the load to approximately 10% of maximum and an example is shown in fig.1.12. The crack was observed to close almost completely up to a distance of approximately 0.5 mm from the crack tip. On reloading the crack was observed to follow the same primary crack path except in cases of crack bifurcation when it was sometimes observed to follow a new crack path as will be discussed in the next section.

1.3.3. The R-curve characteristics of 96% Al_2O_3 .

The DT configuration has enabled measurements of K_I as a function of crack length extension to be obtained for longer cracks than in any other work in the literature. We have shown, by reaching well into the steady-state region (K_{IC}), that, at least in this material, the crack length over which crack surface interactions act, is very extensive and depends on the microstructure.

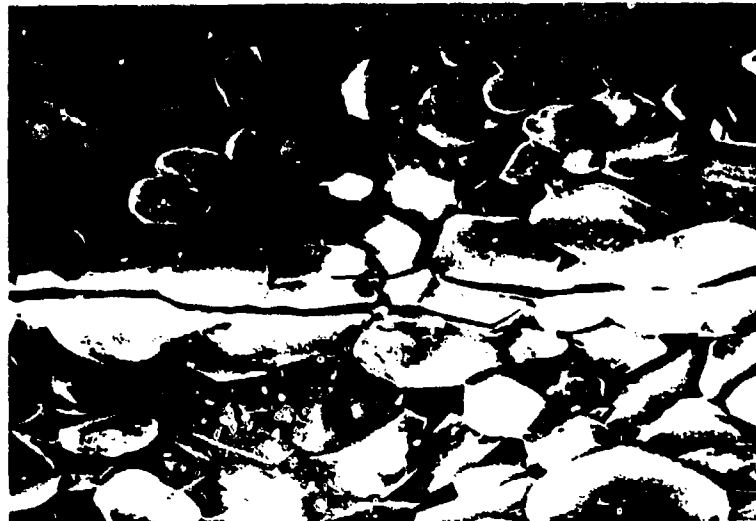


a.

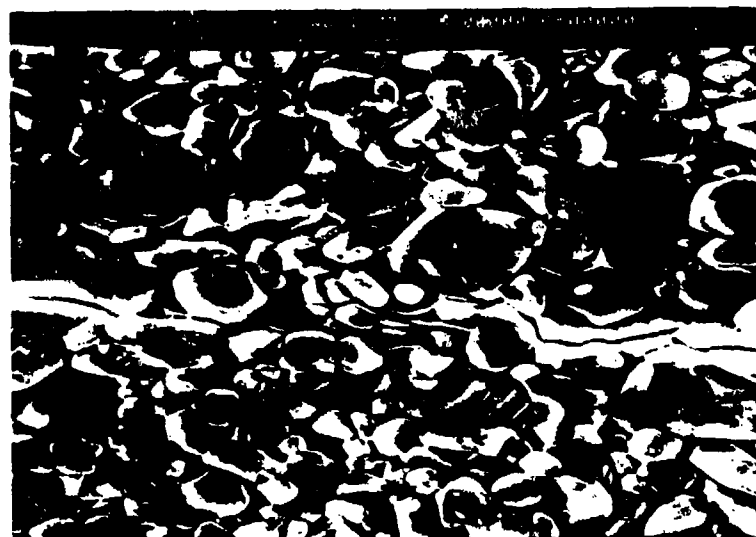


b

Fig.1.9a,b.Example of crack mode change from transgranular to intergranular on encounter with a grain boundary at a low angle (near centre) and subsequent return to transgranular fracture mode.



a



b

Fig.1.10a,b.Two examples of crack bifurcation.

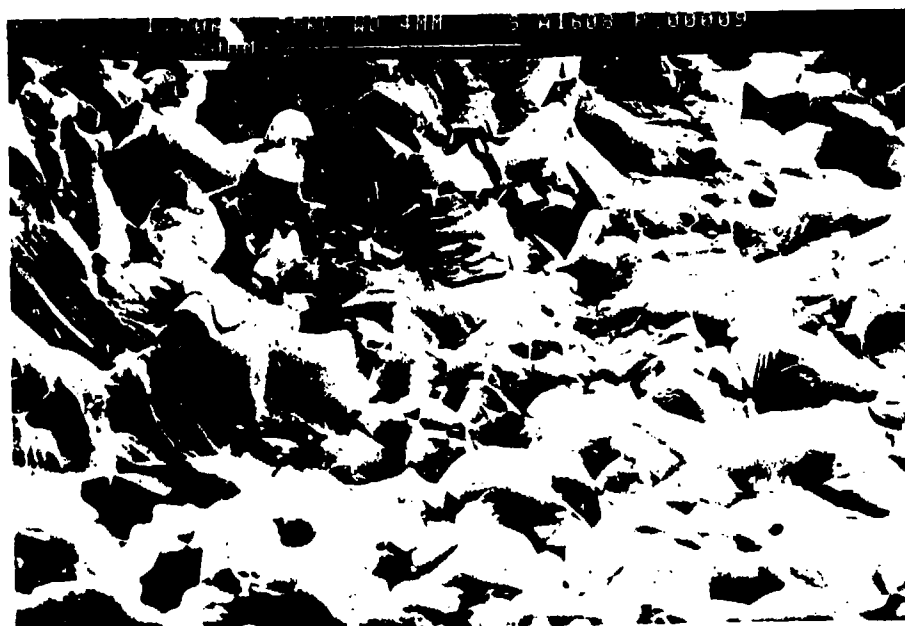


Fig.1.11.An example of secondary microcracking on a fracture surface.



a

Under load



b



c

Unloaded



d

Fig.1.12a-d. An example of elastic relaxation and crack-tip closure. The crack tip is almost invisible even under higher magnification as shown in (d).

The combined results of K_I versus crack length (measured from the notch tip) for 6 as-sintered specimens are shown in fig.1.13. Preliminary results for aged specimens with mean grain size of $5.6\mu\text{m}$ and $6.6\mu\text{m}$, are shown in fig.1.14, where a close-fit line for the as-sintered results has been included for comparison. It is difficult to make a comparison between these results and others reported in the literature because no work has been reported in the literature on the R-curve behaviour of this particular material for large crack lengths, but a number of observations may be made by examining the results obtained:

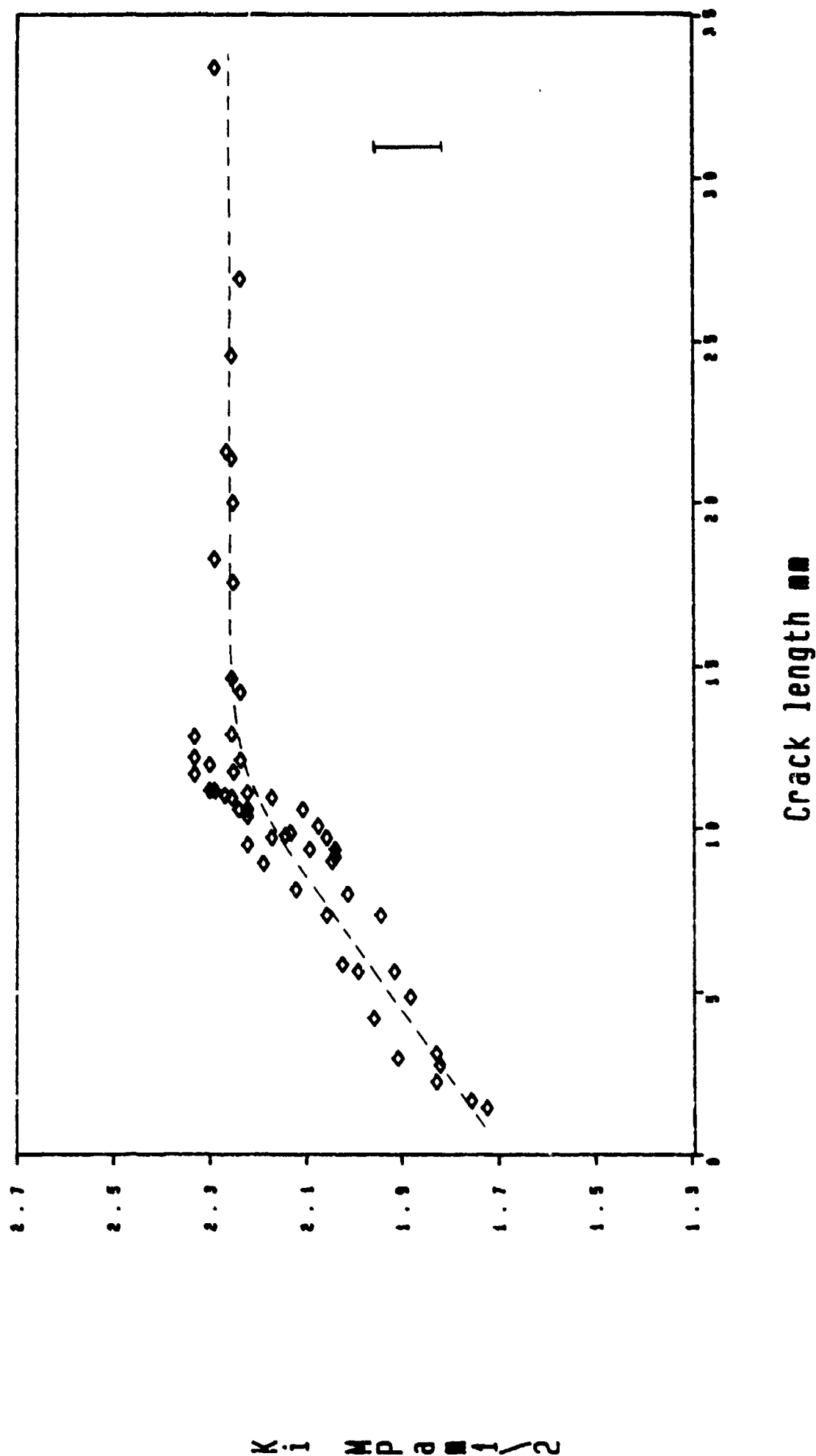
(1) The Double Torsion technique can be used successfully to investigate the R-curve behaviour of ceramics. Since the measurement of K_I is independent of crack length, the increase in K_I with crack length observed is indeed due to a physical process involving the crack faces behind the crack tip.

(2) There is a very large "crack-wake bridging zone" (up to 12mm in the case of the as-sintered specimens) of the order of 200 grain diameters. Large bridging zones of the same order of magnitude have also been observed before by Swain [26] and Swanson and co-workers [27] for coarse grained pure alumina. However, the present material displays predominantly transgranular fracture behaviour (approximately 80%), whereas most of the observations of R-curve behaviour reported in the literature were on materials displaying predominantly intergranular fracture behaviour (e.g. [24-26,34]).

(3) There appears to be an almost linear increase of K_I with crack length up to the steady state value (K_{IC}). This appears to be at variance with the results obtained for other materials which show a smoother increase and transition between the increasing K_I region and the plateau region. The gradient of the increasing portion of the curve appears to increase significantly with increasing grain size. This agrees qualitatively with the results of Steinbrech and co-workers [24]. Further work is planned in order to fully characterise this phenomenon and the influence of grain size.

(4) The steady-state fracture toughness of the material appears to be a

R-curve of as-sintered ADS96R ($d=4.1\mu\text{m}$)



◇ 4.1 μm

Fig.1.13. Summary of the results obtained on the R-curve behaviour of as-sintered ADS96R. K_I increases almost linearly with crack length extension up to K_{IC} .

R-curves of aged ADS96R (line: as-sintered)

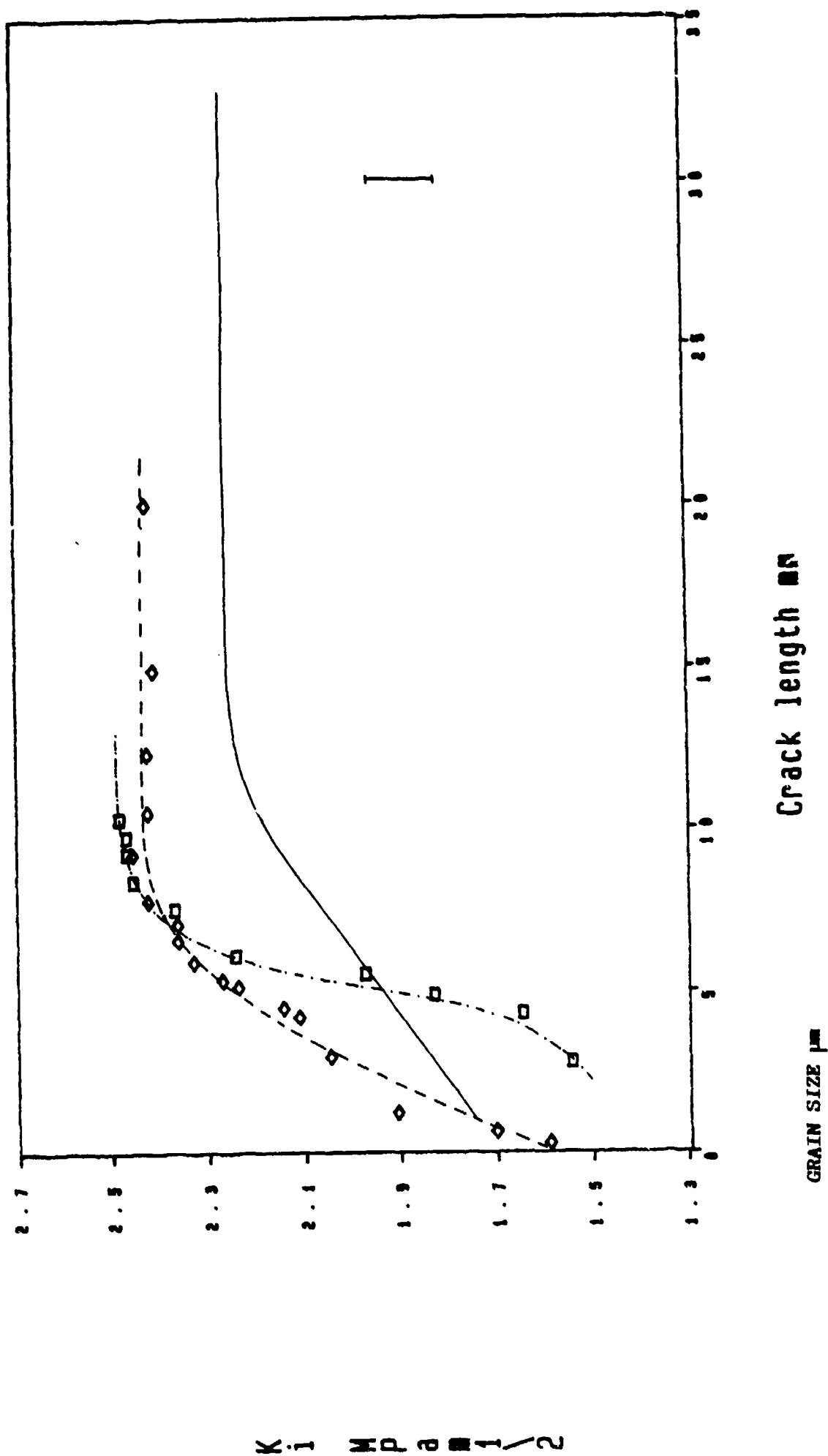


Fig.1.14. The results obtained on the R-curve behaviour of aged ADS96R specimens compared with the results of the as-sintered specimens (solid line).

weakly increasing function of grain size which agrees with the results of Mussler et al [13]. This observation will be examined fully in the next phase of the work. By extrapolation, the K_{IC} for the as-sintered material measured in this work ($2.3 \pm 0.2 \text{ MPa}\sqrt{\text{m}}$) is close to the result ($\approx 2.8 \text{ MPa}\sqrt{\text{m}}$) obtained by Cook et al [29] for a coarse-grained AD96 alumina.

The phenomenological model of Mai and Lawn [28] (described in section 1.1) has been used to analyse the results obtained in this work for the as-sintered specimens. Using trial values of bridge spacing $d = 50\mu\text{m}$ (from observation ≈ 10 grain diameters) and steady-state bridging length, $\Delta c^* = 12\mu\text{m}$ (from the results), approximate iteration of the T equations gave the best fit for $m = 0$ as found also by Mai and Lawn [28] for the results of Swain [27], with $T_0 \approx 1.4 \text{ MPa}\sqrt{\text{m}}$ and $T_{\infty} \approx 2.5 \text{ MPa}\sqrt{\text{m}}$ which are close to the experimental results shown in fig.1.13. However, using the experimentally determined values, we obtain that, for ideal line cracks, $u^* \approx 1\mu\text{m}$ which appears to be significantly smaller than that observed by in-situ SEM (see micrographs presented in the next section). The bridging stress, p^* also appears to be low ($\approx 5\text{MPa}$ for $m=0$ to $\approx 15\text{MPa}$ for $m = 2$), although the fracture energy of the bridges was found to be of the order of 5 J/m^2 which is comparable with typical fracture surface energies. Thus it appears that the model proposed by Mai and Lawn is capable of giving approximate estimates of the R-curve parameters but needs to be refined further. The main problem appears to be their choice of the stress separation function (equation 1.4). A better choice for this function may possibly be made by consideration of the actual physical processes involved in the bridging effect. This aspect is being dealt with in the present work by in-situ SEM observations and a number of possible mechanisms have been proposed, as detailed in the next section. The question of the correct separation function will be addressed in the near future.

1.4. DISCUSSION

This part of the report presents preliminary results on the R-curve characteristics of 96% Al_2O_3 -glass system. Consequently it is not yet possible to arrive at a definite relationship between the R-curve behaviour of the material and its microstructural parameters. However the R-curve behaviour of the as-sintered material has been well-characterised and the in-situ dynamic SEM investigations have provided a great deal of information on the actual physical processes that occur behind the crack tip in the crack wake which give rise to the R-curve behaviour.

As mentioned in the review section, three completely independent mechanisms have been proposed as explanations for the R-curve behaviour: (i) a microcracking process zone around the crack tip as discussed by Kreher and Pompe [18], (ii) bridging due to unbroken ligaments behind the crack tip as proposed by Swanson and co-workers [27] and, to a lesser extent, (iii) bridging due to compressional thermal expansion anisotropy stresses exhibited by abnormally large grains as suggested by Swain [26]. All three of these possible processes have been studied during the in-situ investigations but no evidence at all has been found for the first and third mechanisms: no extensive microcracking was evident anywhere near the crack tip even at the highest magnification examinations. It must be noted that dissipation of the large amounts of energy that is needed to explain the results (discussed later) would result in very extensive microcracking especially close to the crack tip, if this mechanism is indeed present. By considering the crack closure microphotographs in fig.1.12 it is evident that if there was any extensive transgranular microcracking present it would probably have been observed. Furthermore, no evidence of any abnormally large grains was found along the crack path, at least in such densities as to contribute significantly to the energy dissipation observed as hypothesised by Swain [26].

However, strong evidence has been found for the second type of mechanism proposed: bridging due to unbroken ligaments behind the crack tip. This has

been observed in numerous regions along all the cracks examined during crack opening and propagation. Figs. 1.15 and 1.16. show clearly two examples of crack bifurcation resulting in a ligament which is still attached strongly to the (apparently) separated crack face so as to result in crack path deviation on further increase in load. Some evidence of crack bifurcation similar to that shown in figs. 1.15 and 1.16 has also been observed by Swanson et al [27] and Reichl and Steinbrech [34], by optical microscopy of cracks in Al_2O_3 . In some cases of grain bridging, the eventual fracturing of the bridge was accompanied by substantial energy release, resulting in actual loss of a part of the bridging ligament as illustrated in the example shown in fig.1.17.

In addition to bridging ligaments, wedged grains acting also as bridging elements were observed between the crack faces as shown clearly in fig.1.18. The microcracking evident on the bridging ligament shown in fig.1.18a (arrowed), for example, indicates that there are high bending and frictional stresses on the ligament due to the movement of the separating faces and the wedging action of the surrounding grains. This mechanism would thus be expected to contribute substantially to energy dissipation and is discussed in some detail later.

Another possible mechanism of energy dissipation observed was tractional forces between irregular protuberances on the separating faces. A possible example is shown in fig.1.19. where the area of contact between the two opposing grains is clearly visible. However, because of the predominantly regular nature of the transgranular cracks in this material, this particular event was observed only infrequently and thus it is not thought to contribute a significant amount to the energy dissipation.

Prior to attempting an analysis of the various mechanisms in terms of their energy dissipation characteristics, it is instructive to consider the possible contribution of the bridging ligaments observed to the total stress intensity measured. By accurate examination of the video tapes and the evidence obtained during the tests, it appears that the area density of unbroken ligaments distributed about the crack faces may be as high as 10-15%, which agrees with



a



b

Fig.1.15. An example of bridging by crack bifurcation. The lower crack path in a) has remained intact due to bridging.



a



b

Fig.1.16. Another example of bridging by crack bifurcation. The main crack has followed the lower crack path.



a



b

Fig.1.17. Complete loss of upper half of bridging grain in a) due to large energy release following bridge fracture.



a



b



c



d

Fig.1.18.Examples of bridging due to wedged ligamentary grains. Note the microfracture of the bridging grains especially evident in a).

the calculations of Reichl and Steinbrech [34]. From the basic energy equation for the amount of energy needed per unit area for fast fracture:

$$G_c = K_{Ic}^2 / E \quad 1.9$$

where G_c = Energy per unit area needed for the formation of new crack surface
 E = Young's modulus of the material,

it can be seen that the observed increase of K_I from 1.7 to 2.25 (a ratio of 1.3) over the interaction zone requires an additional energy input of the order of $\approx 1.2 \text{ J/m}^2$ (75%). This must be provided by, firstly, fracturing of the unbroken ligaments which, by fracture area considerations, appear to contribute possibly 1/4 to 1/3 of the total needed. The balance must be provided by other mechanisms such as elastic bending of the ligaments, friction of "locked" grains and friction and bending of the wedged grains observed. The area density of these wedged ligamentary grains appears to be at

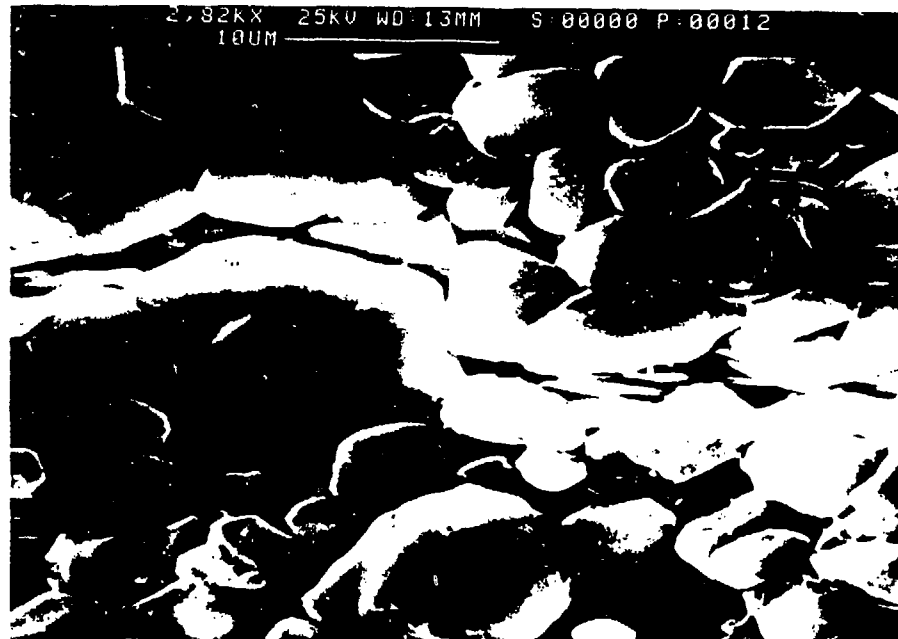


Fig.1.19. An example of tractional interaction between grains on the crack surfaces.

least 0.5-2%. and their contribution to the energy dissipation is discussed below.

A simple analysis of the forces involved under these circumstances indicates that there are three possible modes of energy dissipation whose relative contributions would be dictated by the particular configuration of the wedged grain:

1. Energy dissipated in bending of an elastic ligament up to fracture.

This mechanism has been alluded to by a number of workers in the past in terms of bending of the bridging ligaments by the movement of the separating crack faces. It is of-course also present in the case of the wedged grains. However, a simple model of the maximum energy dissipation that can be expected shows that the contribution of this mechanism to the energy dissipation is extremely small and cannot account by any means for the G_I increase observed:

Consider an elastic bridging ligament in the form of the elastic beam shown in fig.1.20. The aim is to calculate the work done in bending the beam until

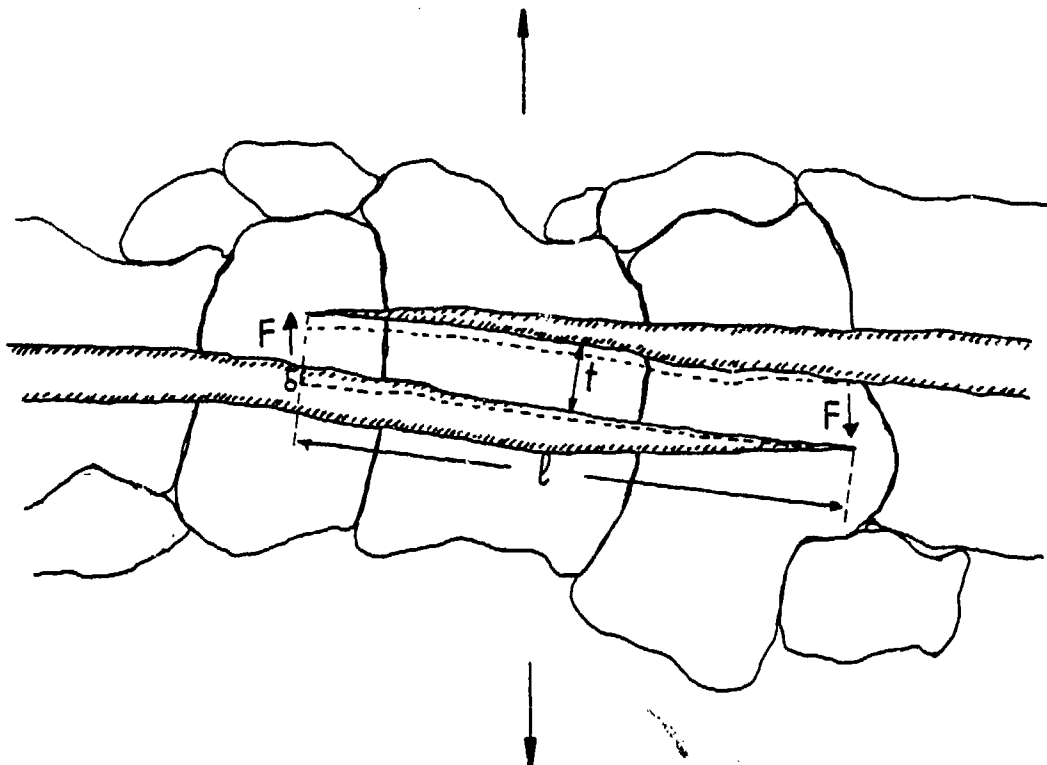


Fig.1.20. Schematic diagram of an elastic bridging ligament.

it breaks. For this configuration:

$$\delta = \frac{F\ell^3}{12EI} \quad 1.10$$

where E = Young's modulus of the material and

$$I = \text{Moment of inertia} = \frac{bt^3}{12}$$

The energy stored in the beam when loaded by a force F is:

$$g = \frac{1}{2} F \delta = \frac{F^2 \ell^3}{24EI} \quad 1.11$$

The maximum force is that which will just break the beam. The stress at the beam surface is:

$$\sigma = \frac{M t}{I} = \frac{F \ell t}{4I} \quad 1.12$$

This will be maximum at fracture (approximately equal to the modulus of rupture of the bulk material). Substituting for F in eqn.1.11. we get at fracture:

$$g = \frac{2}{3} \frac{\sigma_{\max}^2}{E} \frac{\ell I}{t^3} \quad 1.13$$

Now the increase in toughness ΔG observed in this work ($=K^2/E$) is:

$$\Delta G = N_a g = \frac{2}{3} N_a \frac{\sigma_{\max}^2}{E} \frac{\ell I}{t^3} \quad 1.14$$

where N_a = number of ligaments or wedged grains per unit area = $f/\ell b$
(f =fraction of area of interface covered by bridging ligaments)

Substituting for I , N_a and setting $t = \text{grain size} = d$ we obtain:

$$\Delta G = \frac{1}{18} f \frac{\sigma_{\max}^2}{E} d \quad 1.15$$

Taking $E = 300 \text{ GPa}$, $\sigma_{\max} = 400 \text{ MPa}$, $\Delta G \approx 1.2 \text{ to } 4.0 \text{ J/m}^2$ and $d = 5 \mu\text{m}$ and solving for f we find:

$$f \approx 8 \text{ to } 27 \quad 1.16$$

which obviously shows that the elastic bending of the bridging ligaments cannot account for the increase in G_I observed.

2. Energy dissipated by a wedged grain against friction.

A wedged grain locked into both crack faces, as shown schematically in fig.1.21, would be expected to dissipate energy in the form of work done against friction by its motion relative to the constraining grains. The frictional stress under these circumstances is:

$$\sigma_f = \mu \sigma \quad 1.17$$

where μ is the coefficient of friction and σ the average stress exerted by one grain on another

Then the increase in toughness ΔG is given by:

$$\Delta G = N_a \mu \sigma 4\ell h^2 \quad 1.18$$

Setting $N_a = f/d^2$, $h \approx d/4 \text{ to } d/8$ (from SEM observations) and $\ell \approx d$, we

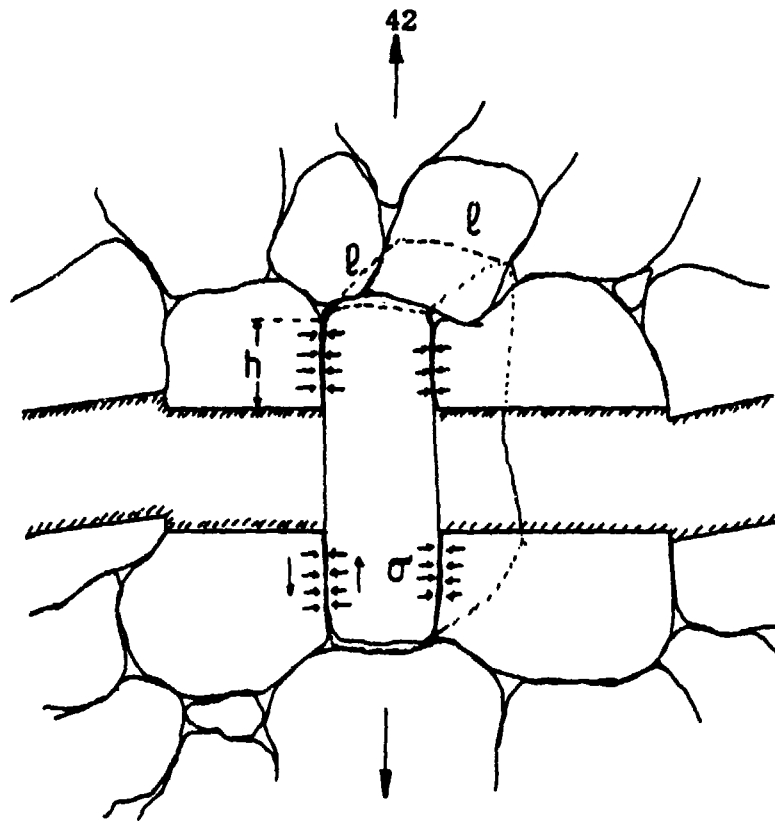


Fig.1.21.Schematic diagram of a wedged grain working against friction due to the relative motion of the crack faces.

find:

$$\Delta G = \frac{\mu}{4} f \sigma d \quad \text{to} \quad \frac{\mu}{16} f \sigma d \quad 1.19$$

and taking values of $\mu = 0.5$, $d \approx 5 \mu\text{m}$, $\Delta G \approx 1.2 \text{ J/m}^2$ and $\sigma \approx 400 \text{ MPa}$ as the maximum stress exerted by the restraining material, possibly due to the thermal expansion anisotropy exhibited by the material, as before, we find:

$$f \approx 5 \times 10^{-3} \quad \text{to} \quad 2 \times 10^{-2} \quad 1.20$$

Thus only 0.5 to 2% of the grains need to be interlocked and subject to frictional forces to account for the energy dissipation measured.

3. Energy dissipated by friction due to an angled wedged grain rotating against the restraining material.

In the case of a grain wedged at an angle between other grains on both sides of a crack as shown schematically in fig.1.22 and observed in this work (fig.1.18), work is done against friction between the grain and the restraining material on both sides of the crack as the grain rotates and finally pulls free. The frictional forces would be expected to be present at the areas marked by arrows in fig.1.22 and increase in magnitude as the crack opens and the grain rotates. In addition, it is possible that the bending stresses induced by the rotating grain may result in the nucleation of secondary cracks in the restraining material, as was observed in fig.1.18a.

If the maximum stress acting across the sliding surface is σ_{\max} , and the area over which these frictional forces act is αd_{\min}^2 (where d_{\min} is the smaller dimension of the grain and α the area fraction subject to frictional forces $\approx 1/4$), then the work done against friction at both sides of the crack in rotating the grain through an angle θ is:

$$g = 2 \mu \sigma_{\max} \alpha d_{\min}^2 \ell \theta \quad 1.21$$

where μ is the coefficient of friction and ℓ the moment arm $\approx d_{\min}/2$

The total work done in rotating the grain over $\pi/4$ (average over all possible rotations between 0 and $\pi/2$) is:

$$\Delta G = N_a g = \frac{4}{\pi} \frac{f}{d_{\min} d_{\max}} g$$

where N_a and f are defined as before and the area of an elliptical grain has been taken as $\frac{\pi}{4} d_{\min} d_{\max}$.

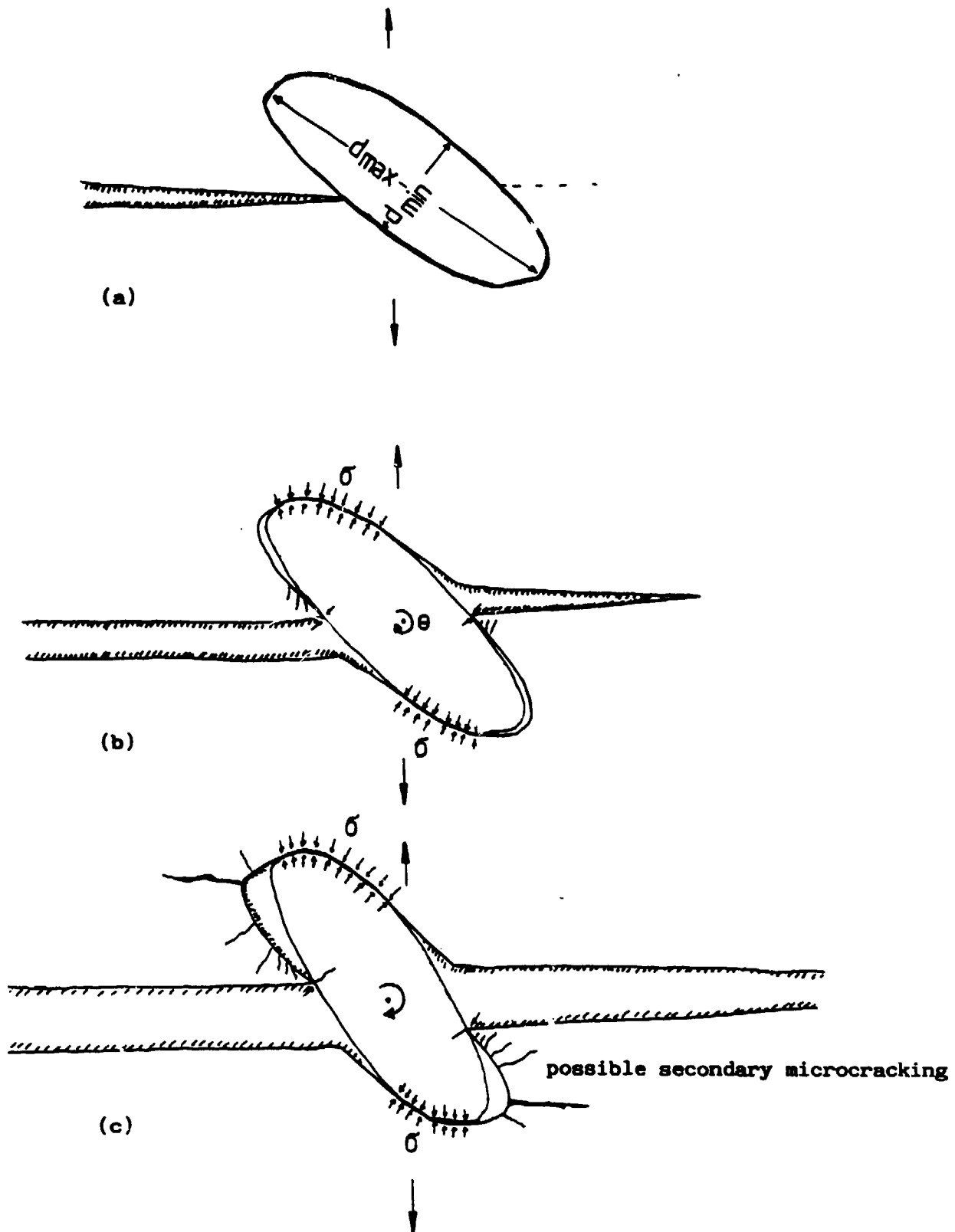


Fig.1.22. Schematic of an angled wedged grain rotating against friction by the relative motion of the crack faces.

After a rotation of $\pi/4$ the grain would possibly be subject to the frictional mechanism proposed in (2) above. If it pulls free the total energy dissipated would be:

$$\Delta G = \alpha \mu f \sigma_{\max} \frac{d_{\min}}{d_{\max}} d_{\min} \quad 1.22$$

Taking $d_{\max}/d_{\min} \approx 4$ and $\alpha \approx 1/4$ we find:

$$\Delta G = \frac{\mu}{16} f \sigma_{\max} d_{\min}$$

Taking $\sigma_{\max} \approx 400$ MPa $d_{\min} \approx 5 \mu\text{m}$ and $\Delta G \approx 1 - 2$ J/m² we obtain finally:

$$f = 0.02 \text{ to } 0.08 \quad 1.23$$

which thus indicates that only 2 to 8% of the grains need be wedged as above to account for the phenomenon.

From the in-situ SEM observations and the simple analysis presented above, it would appear that the mechanism proposed in (3) above in conjunction with that analysed in (2) may account for the R-curve phenomenon in non-transforming ceramics. Furthermore, the similarities between the microstructures in most types of ceramics indicate that the above mechanisms may be active in all ceramics containing elongated grains.

The feasibility of the mechanisms discussed in (2) and (3) above will be further investigated by measuring the energy dissipation per cycle (during a loading/unloading cycle with and without primary crack propagation) and by quantitative examinations of the final fracture surface topology by three-dimensional SEM imaging.

PART 2. COMPRESSIVE FRACTURE OF CERAMICS

2.1. Fundamentals of compressive fracture of brittle materials and related theoretical developments.

The mechanical behaviour of brittle materials both under tension and compression have been of interest to engineers and architects since very early times. Although research on the properties of materials in the modern sense only developed during the past two to three centuries, the monumental structures that have remained since ancient times such as the monuments of Mesopotamia and Ancient Egypt, indicate some empirical knowledge of the comparative properties of the materials which were used. Later, the Ancient Greeks and the Romans actively studied engineering and there is evidence to suggest that some knowledge of the comparative properties of materials was being used in everyday life.

Although the mechanical properties of materials have been studied extensively during the past three centuries, the elucidation of the mechanics of brittle fracture in tension is mainly due to the pioneering work of Griffith [58] in 1920 and, later, Orowan [59] and Irwin [60] and has been expanded during the last few decades by many workers [3] to form a new branch of Engineering: Fracture Mechanics. It is now well understood that fracture on the atomic scale is always a tensile process in which opening displacements result in separation of the crack faces. In brittle materials i.e. materials which display almost no plasticity at normal temperature and pressure conditions, such as most silicate rocks, ceramics etc, separation of the crack faces requires the attainment of the cohesive strength of the solid by concentrating tensile stresses in localised regions such as sharp flaws, pre-existing microcracks, micropores etc. Initiation and propagation of cracks from such regions of stress concentration takes place when the Mode I stress intensity K_I reaches a critical value K_{IC} , known as the fracture toughness of the material and is governed by the elastic and cohesive properties of the material. Thus, although the material parameters that affect K_{IC} are still the

subject of much research, the phenomenology and mechanisms of brittle fracture under tension are quite well understood (see e.g. [3]).

In contrast however, although the mechanical behaviour of brittle structural materials such as stone, brick and cement were of interest to early civil engineers, the systematic study of their compressive properties, such as their strength, only dates from the 2nd half of the 19th century [61]. The first attempt at a theoretical understanding of compressive fracture was also carried out by Griffith in 1924 [62] who was the first to consider the effects of cracks in brittle solids subjected to compression. The main difference between tensile and compressive fracture is that in tension, fracture is unstable due to the energetically favourable propagation of a single crack, whereas in compression, fracture is initially stable due to the slow propagation of initiated cracks until they interact to cause final failure.

In a solid with randomly oriented stress concentrating flaws, such as pre-existing microcracks, under triaxial compression, fracture can take place locally when shear stresses produced by unequal stress levels displace the surfaces of the pre-existing microcracks against facial frictional forces [63,64] and produce tensile stresses near the tips of the microcracks as shown schematically in fig 2.1 [65-67]. In general, when the stress intensity at the tips exceeds the critical stress intensity of the material (in most materials at a stress approx. half their uniaxial compressive strength), secondary cracks (wing or sigmoidal cracks) initiate at the tips and propagate parallel to the direction of maximum compressive stress (σ_1 in fig 2.1) and perpendicular to the direction of minimum compressive stress (σ_3 in fig 2.1). As the applied axial compressive stress increases, the number of secondary cracks that initiate increases and, macroscopically, the specimen displays substantial dilatancy. If $\sigma_3 = 0$, i.e. under purely uniaxial compression, the secondary cracks can grow to tens of times the size of the original microcrack until eventual overall fracture of the body by "slabbing" parallel to the direction of maximum compressive stress as shown schematically in fig 2.2a. When the transverse confining compressive stress, σ_3 is greater than zero, the number of secondary microcracks initiating at regions of stress concentrations increases but they grow to only a few times the length of the original

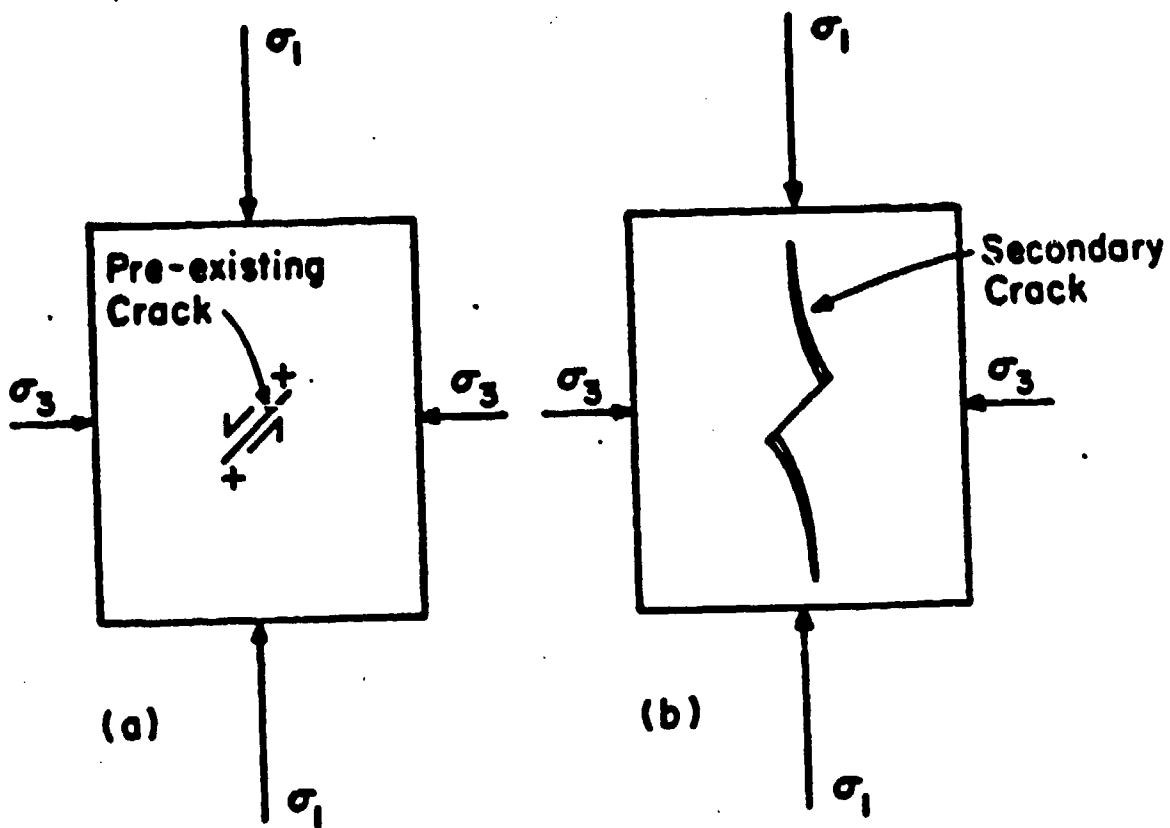


Fig.2.1. Schematic diagram of Mode I crack initiation (a) due to a pre-existing inclined crack in a brittle material, and (b) its propagation parallel to the principal compression direction (σ_1). (From [65]).

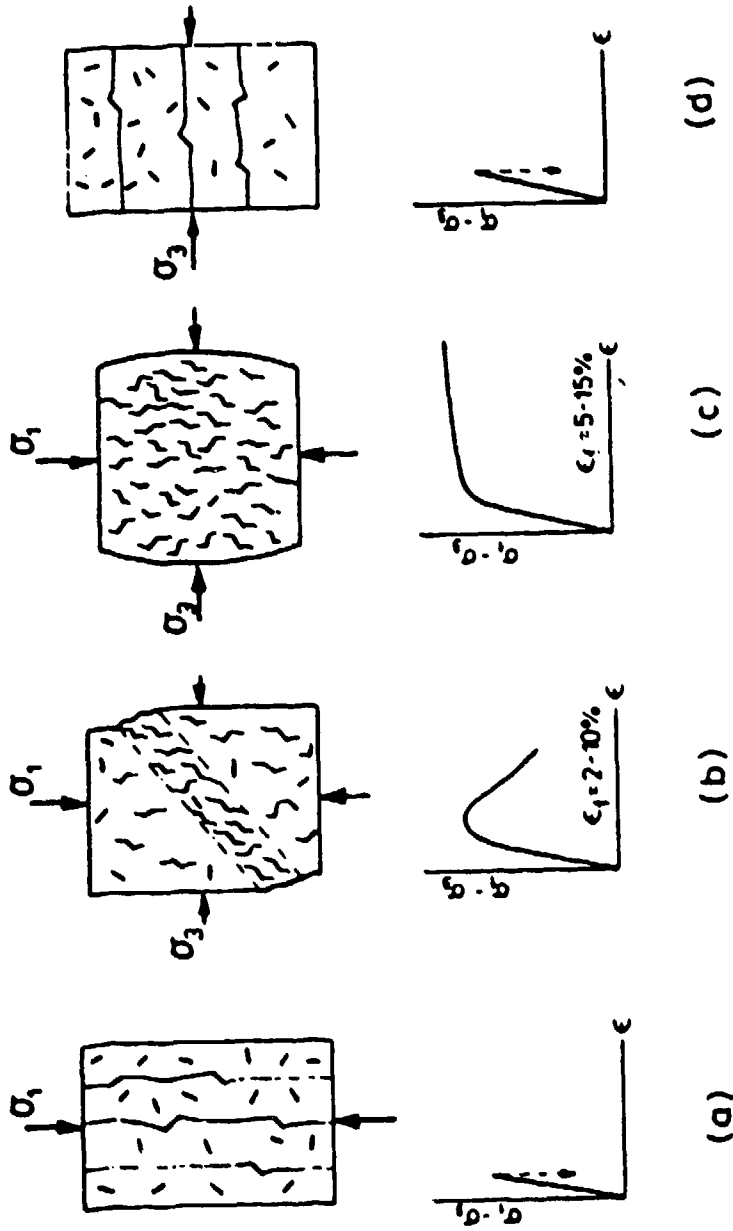


Fig.2.2.Failure modes in compression of brittle materials.(a) and (d): slabbing, due to the propagation of a small number of cracks parallel to the principal compression direction, (b): shear-zone formation by microcrack interaction and (c): near-homogeneous deformation by distributed microcracking. (From Ashby and Hallam [66]).

microcracks [65]. When the density of the pre-existing flaws is high, as for example in the case of rocks etc, many microflaw-secondary crack systems can interact synergistically to cause overall fracture. The form of the final failure depends on the level of the confining transverse compressive stress. At low to intermediate confining stress levels a sample with uniformly distributed microflaws would be expected to fail in a shear mode when a number of flaw-secondary crack systems combine en-echelon to form a shear zone [65,68] as shown in fig 2.2b. However, it is possible for a specimen to fail by "slabbing" if it contains a small number of large flaws (of size many times the grain size). In this case the secondary cracks can grow long enough parallel to each other and to the direction of the maximum compressive stress to cause final fracture. It is thus possible to distinguish between extrinsic and intrinsic compressive failure [65], depending on whether final failure was due to a single crack (or a very small number of non-interacting cracks) initiated at an inherent large flaw or due to the interaction of a large number of small cracks initiated at numerous small microstructural flaws such as grain boundaries, micropores, etc. At higher levels of confining compressive stress a large number of secondary cracks initiate and the specimen displays substantial dilatancy and pseudo-plasticity with large scale deformation as shown in fig.2.2c [68]. In the case of compression under moderate confining pressure, the experimental evidence suggests that the effective fracture energy which is now in an in-plane shear Mode II can be several orders of magnitude higher than the tensile fracture toughness K_{Ic} [65].

It must be noted that under very high confining pressures, most brittle, crystalline inorganic solids can undergo true plastic deformation by dislocation glide even at low temperatures [65]. Thus, this discussion of compressive fracture limits itself to pressures up to approximately the compressive strength of the materials in question.

Both from the scientific and industrial point of view the understanding of compressive fracture of brittle solids and the establishment of specific constitutive relations for inelastic deformation between the various

parameters is extremely important. Failure by compressive fracture can occur in a wide range of applications, from ones that do not in general have catastrophic consequences, such as rock machining operations, to cases where failure can have catastrophic consequences such the stability of mine shafts, various civil engineering applications and even the stability of missile casings [65]. Thus, constitutive equations and a detailed understanding of compressive fracture can help in solving a variety of problems both in designing using brittle materials and in constructing failure surfaces for particular materials which can give direct information on the stress state at failure.

The theoretical developments of brittle fracture in compression have followed two complementary approaches: the phenomenological approach which is based on the deformation behaviour of the material and tries to relate the total deformation of the material or deformation increments with the pressure and the effective stress. In these models (reviewed in [65]) the shear localization due to the co-operative interaction of a number of flaw-microcrack systems is treated as a volume phenomenon in which the onset of instability can be hastened by initial flaws. In this respect they are empirical continuum models and the material behaviour is described by parameters obtained from averages of physical quantities. Recently Costin and co-workers [69-71] have developed a phenomenological model of the damage mechanics of compressive fracture using a continuum model based on the mechanics of microcrack growth and interaction. By considering experimental results, they showed that they could use the model (incorporating a number of adjustable parameters) to simulate the behaviour of brittle rock under relatively complex states and predict, at least qualitatively, the location and orientation of major fractures at high levels of damage.

The alternative approach is the mechanistic approach in which the initiation and growth of cracks under compression is modelled by considering the stress concentrations at sharp pre-existing flaws in the material and is treated using standard Fracture Mechanics in the same way as tensile cracks. However,

whereas the initiation and initial propagation stress is well understood [e.g. 62-64,72,73], the subsequent progressive synergistic interaction of a number of small neighbouring flaw-microcrack systems which leads to either a shear zone or gross deformation is less well understood. A number of reports [74,80] have established that extrinsic failure can occur when a large body under compression is subjected to compression and that in the case of a large number of flaw-microcrack systems the shear-zone instability develops when the length of individual cracks is comparable to their spacing. Kachanov [81] has attempted to develop a physical theory of inelastic behaviour of rocks by considering the initiation and propagation of the secondary microcracks and showed that inelastic behaviour resulting from crack face sliding and crack propagation is generally path-dependent and, like plasticity, can be described only for arbitrary stress histories by incremental relations. His model does not consider the applied stress modification by the extension of the microcracks and thus it cannot be extrapolated to the condition for microcrack interaction and shear zone formation.

The micromechanics of compressive microfracture under triaxial conditions have also been modelled recently by Nemat-Naser and Horii [63] and Ashby and Hallam [66] who considered analytically the growth and subsequent interaction of microcracks initiated at pre-existing sharp flaws inclined to the direction of maximum compressive stress and Sammis and Ashby [68] who developed an analytical model for the initiation and propagation of microcracks from spherical pores in 2 and 3 dimensions. The theoretical models for both extreme types of flaws (spherical pores and sharp cracks) lead to approximately identical expressions for the crack initiation relationship between the axial stress σ_1 and the radial stress $\sigma_3 = \sigma_2$, ($\sigma_1 > \sigma_3$) which can be written as:

$$\sigma_1 = c_1 \sigma_3 - c_0 \quad 2.1$$

where the constants c_1 and c_0 depend on the nature of the flaws.

When cracks nucleate from spherical holes the constant c_1 was predicted to be about 3.1 to 3.4 [68] and when they nucleate from cracks it has been predicted [63,66] to depend on the coefficient of friction between the sliding

faces, μ , and may range for example between approx. 2.5 and 3.5. if μ ranges between 0.5 and 0.7. Experimental results on crack initiation in Westerly granite (quoted in [81]) suggest a value of c_1 of approx. 2.8 for both pores and cracks. The constant c_0 is predicted to depend in both cases on the fracture toughness K_{IC} and the flaw size $2a$. When the flaws are spherical pores, $c_0 = 1.6K_{IC}/\sqrt{\pi a L_0}$, where $2a$ is the diameter of the pores and L_0 is a measure of the roughness of the pore (the length of the initial cracks associated with the pore). When the flaws are sharp cracks, $c_0 = 3.1K_{IC}/\sqrt{\pi a}$ where $2a$ is the length of the inclined crack. The experimental data on crack initiation quoted in [82] indicated a value for c_0 of ≈ 60 MPa which would indicate a crack half length of ≈ 0.85 mm which is not unreasonable. Thus it appears that the above models are supported by data on crack initiation in rocks under triaxial compression. The fact that the form of the equation 3.1 as well as the constants are almost identical for both extreme types of flaw, indicates that eqn. 2.1 may be considered as a general criterion equation for damage initiation in compression [82]. In the present work, data on crack initiation in Plaster of Paris specimens of various densities and flaw sizes subjected to uniaxial compression appear to support equation 2.1 as well, as discussed later in this section.

Ashby and co-workers [66,68] treated interactions by considering the "bending" of the ligaments of non-fractured material between microcracks but it was successful only in the case of extensive overlap between cracks. Very recently they extended this physical approach and have succeeded in the construction of fracture initiation and failure surfaces and have paved the way for the development of a theory of damage mechanics of brittle solids [82]. This has enabled the stress-strain and failure characteristics of various materials under compression to be derived from a knowledge of only their elastic properties and defect population and distribution.

In the case of hydrostatic compression, the applied hydrostatic stress, p , on a porous brittle material gives rise to an anisotropic stress distribution in the material around a spherical flaw of radius a as shown schematically in fig.2.3a. This deformed region can be represented by a deformed sphere of

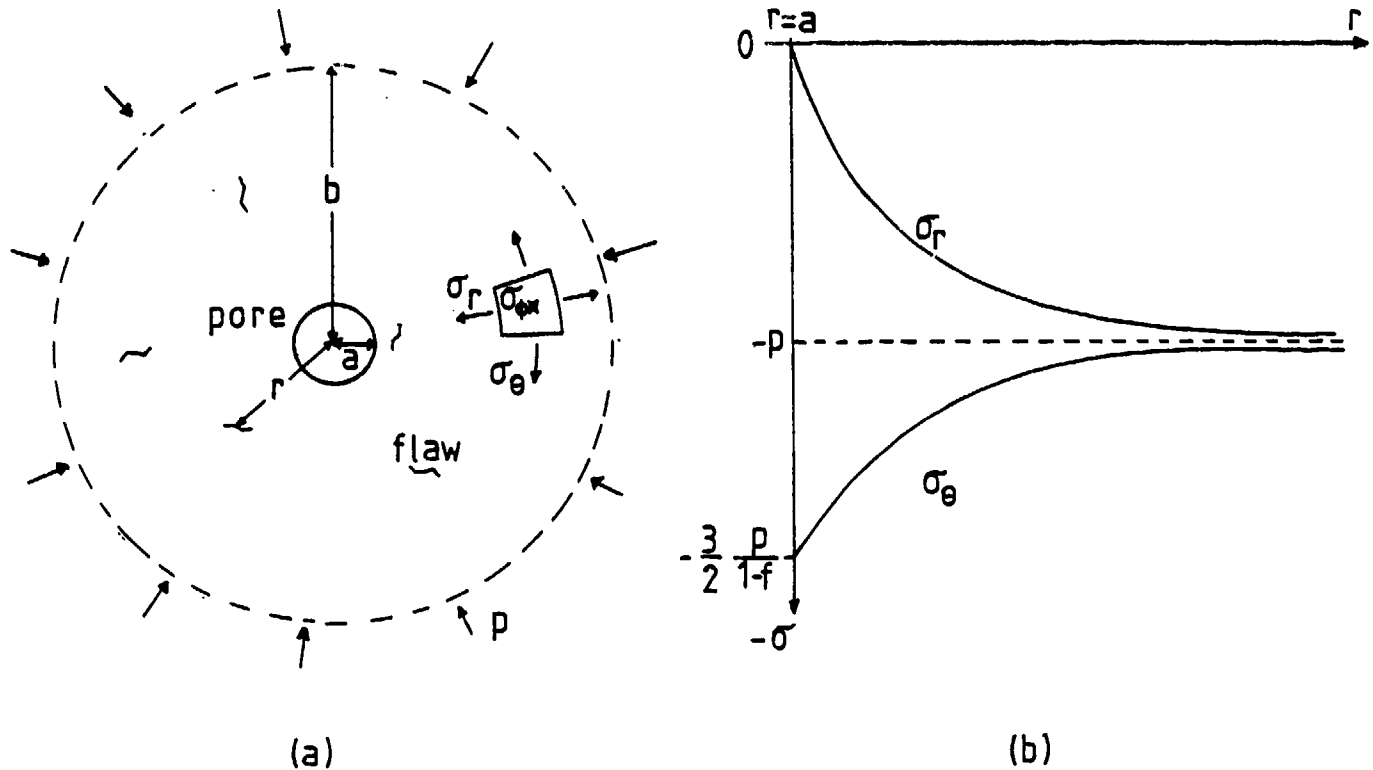


Fig.2.3. Stresses around a spherical pore subjected to hydrostatic pressure p (a) and (b) their variation with distance from pore r (equations 2.2).

radius $b \gg a$. The stresses in a unit volume of the deformed sphere can be represented by the radial stress σ_r and the two equal tangential stresses σ_θ and σ_φ . It can be shown [83] that the stresses around a spherical hole subjected to hydrostatic compression are given by:

$$\sigma_r = -p \frac{b^3 (r^3 - a^3)}{r^3 (b^3 - a^3)} \quad 2.2a$$

$$\sigma_\theta = \sigma_\varphi = -p \frac{b^3 (a^3 + 2r^3)}{2r^3 (b^3 - a^3)} \quad 2.2b$$

According to these relations, as we move away from the pore all stress components asymptotically approach the hydrostatic stress level, $-p$, but, whereas the radial component, σ_r , decreases from 0 at $r = a$ to $\approx -p$ at $r = b$, the tangential components increase from a minimum value $= -3/2 p/(1-f)$ (where $f = a^3/b^3$ is the volume fraction of pores in the material) at the pore

surface, $r = a$, to $\approx -p$ at $r = b$ as shown in fig.2.3b. The presence of a maximum of tangential stress at the surface of the pore means that fracture under hydrostatic compression will initiate near the surface of the largest pore present in the material.

Applying the fracture nucleation equation 2.1 (which still holds with the stresses σ_r and σ_θ replaced by the corresponding radial and tangential components of the applied hydrostatic stress as long as $|\sigma_r| > |\sigma_\theta|$) to the case of hydrostatic compression of porous brittle materials, we find (since σ_r is less compressive than σ_θ):

$$\sigma_\theta = c_1 \sigma_r - c_0 \quad 2.3$$

where $c_1 \approx 3.1$ and $c_0 = \frac{1.6 K_{IC}}{\sqrt{\pi a_p} L_0}$ as before for holes.

Substituting for σ_r and σ_θ we obtain:

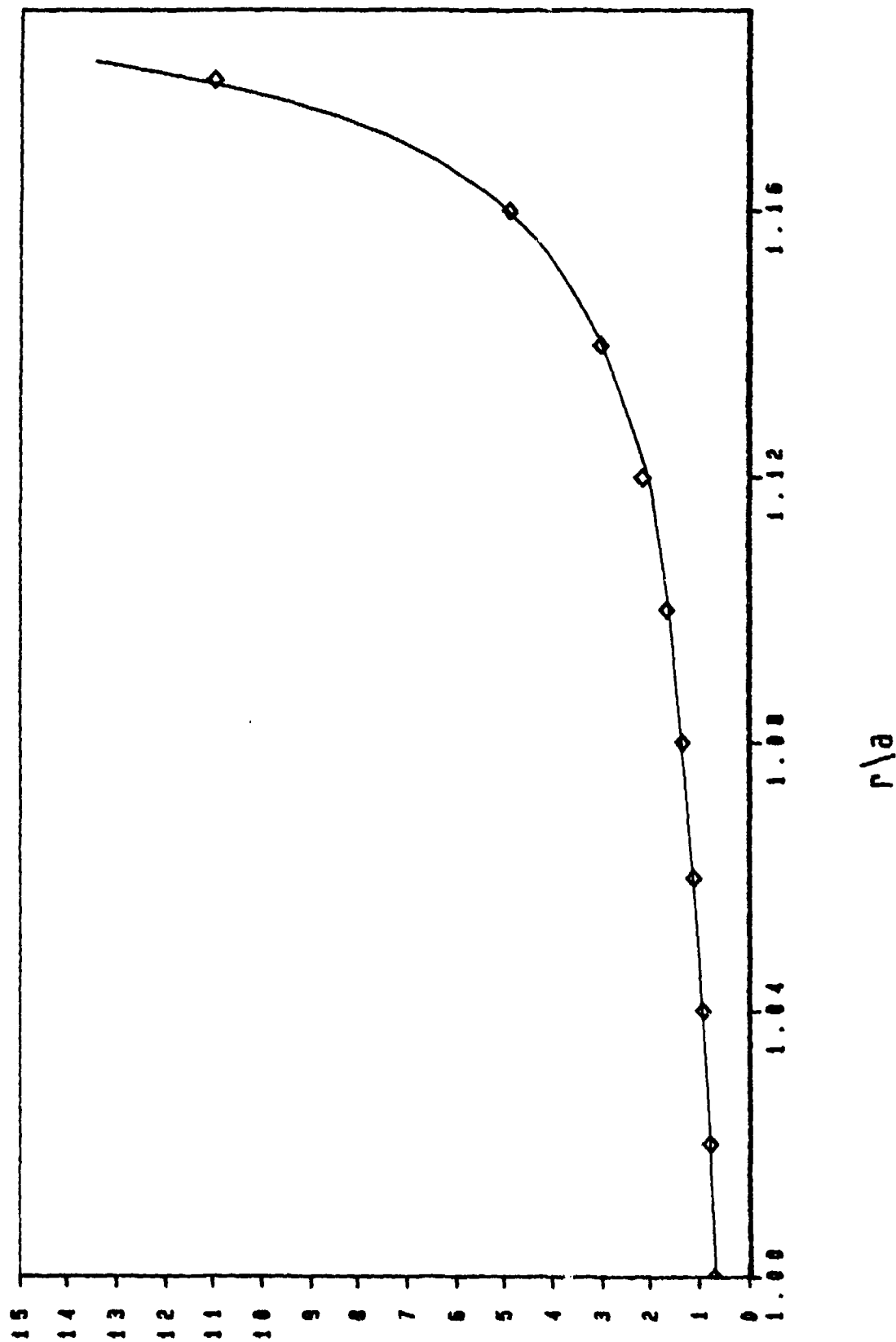
$$-p_{in} \frac{b^3 (a^3 + 2r^3)}{2r^3 (b^3 - a^3)} + c_1 p_{in} \frac{b^3 (r^3 - a^3)}{r^3 (b^3 - a^3)} = -c_0 \quad 2.4$$

using $f = \frac{a^3}{b^3}$ and solving for p_{in} (the hydrostatic stress for fracture initiation) we finally find:

$$p_{in} = \frac{2r^3/a^3 (1-f)c_0}{1+2c_1-2(c_1-1)r^3/a^3} \quad 2.5$$

The dependence of equation 2.5 on r/a allows us to calculate the value of p_{in} that would be required to initiate fracture at various distances from the hole surface as a function of the volume fraction of holes, f and the fracture toughness of the material, K_{IC} . Fig.2.4. shows that p_{in} increases sharply and

Hydrostatic Compr. Fracture Init. Model



Pin Units: $[1-f]C_o$

Fig.2.4.Dependence of hydrostatic fracture initiation stress on r/a according to equation 2.5.

reaches an asymptote at $r/a = \sqrt{(1+2c_1)/(2c_1-2)}$ (≈ 1.2 for $c_1 \approx 3.1$) at which point fracture would be expected to initiate.

The above model predicts that an enclosed cavity will collapse under hydrostatic compression by fracture near its surface and, once the collapse has initiated, it will continue, due to the effective increase in its size, a . Thus, for a material failing due to the collapse of spherical pores, the fracture initiation stress should be close to or coincide with the final fracture stress. This is observed frequently in the case of rock drilling and similar operations. In the present work the fracture initiation and final fracture surfaces were measured for specimens of Plaster of Paris under hydrostatic compression and the results appear to support the above model as will be discussed later in this section.

2.2. Brief review of the literature on the compressive fracture of ceramics.

The experimental investigation of the compressive strength and failure characteristics of ceramics is imperative both for the provision of strength data for the design of ceramic load-bearing components and structural elements and for the provision of accurate microstructural data to enable theoreticians to construct new theories on compressive fracture and to test existing theories. The current and potential applications of ceramics range from high-strength high-temperature applications such as jet and internal combustion engine components to high-wear resistance applications such as those relating to impact and erosion. In most applications the components are subjected to very complex stress situations involving both compressive and tensile stresses. The main difficulty in measuring the compressive strength characteristics of brittle materials concerns the need for very accurate alignment procedures in order to avoid any bending moments on the specimens. This invariably has resulted in large fluctuations between results reported in the literature for similar materials.

Although a fairly large amount of information on the failure characteristics of brittle structural materials with large densities of pre-existing faults,

such as rock and concrete, has been reported in the literature [61,63,65,72-80], only a very limited number of studies on the compressive strength [84-91] and the microstructural failure characteristics [92-94] of "high-technology" ceramics has been reported. All the data found in the literature have been summarized in Table 2.1.

The first reported careful measurement of the uniaxial compressive strength was of a low density Al_2O_3 ceramic [91] using cubic specimens compressed by lubricated WC-Co anvils and resulted in a very high compressive strength for this type of specimen (see Table 2.1). Another early systematic investigation of the compressive strength of 99.5% Al_2O_3 under various multiaxial stress states [86] utilised straight walled tubular specimens for both uniaxial and biaxial compression tests and found that the ratio of uniaxial compressive strength to tensile strength was 7.5 whereas the ratio of biaxial compressive stress to tensile strength was as high as 22. At about the same time Sedlacek [87] carried out compressive and tensile strength measurements on rings of similar material (99.5% Al_2O_3 , grain size $\approx 20\mu\text{m}$, $\rho \approx 3.85\text{g/cm}^3$) and reported a compressive to tensile strength ratio of ≈ 14 .

Later, Sines and Adams [84,88-90] developed very accurate experimental techniques for measuring the uniaxial and biaxial compressive strengths of strong very brittle materials such as ceramics. They measured the compressive and tensile strength of thin tapered walled cylinders of identical material to that used in [86,87] and found that the biaxial compressive strength was only $\approx 5\%$ higher than the uniaxial compressive strength (actually the 1:0.01 compressive strength) and approx. 18 times the tensile strength. It was reported that for that specimen configuration and loading geometry (the specimen had a gauge wall thickness of $\sim 3\text{mm}$) the compressive strength of the material did not vary significantly with transverse compressive load. This was in contradiction with the previous published work but they explained their results by suggesting that previous investigators may not have paid enough attention to the extreme difficulty in aligning the loading system in uniaxial tests. Their results show little scatter and it appears that the scatter

Table 2.1. Literature results on the compressive strength of ceramics

Material	Axial fracture strength, GPa	Ref.
<u>Uniaxial Compression</u>		
99.5% Al_2O_3 : 1/4" ground cube	3.1	91
99.5% Al_2O_3 : open-ended thin-walled rings	3.09 ± 0.25	87
99.5% Al_2O_3 : open-ended thin-walled rings	1.75	86
99.5% Al_2O_3 : short rods	$3.0 - 3.8 *$	92
"82% Zirconia" : thin-walled cylinders	0.16 ± 0.01	84
<u>Biaxial Compression ($\sigma_{\theta\theta}:\sigma_{zz}$)</u>		
99.5% Al_2O_3 : open-ended thin-walled rings (1:0.5)	3.0	86
99.5% Al_2O_3 : thin-walled cylinders (1:0.01) \$	3.40 ± 0.15	88
99.5% Al_2O_3 : thin-walled cylinders (1:0.1) \$	3.75 ± 0.08	88
99.5% Al_2O_3 : thin-walled cylinders (1:0.5) \$	3.55 ± 0.16	88
99.5% Al_2O_3 : thin-walled cylinders (1:0.8) \$	3.64 ± 0.1	88
99.5% Al_2O_3 : thin-walled cylinders (1:1) \$	$3.21 \pm 0.16 @$	88

* : increases with incr. strain rate, @ : cracked on preloading

\$: stress rate $\approx 2.5 \text{ MPa/sec} \approx 7 \times 10^{-6} \text{ sec}^{-1}$

decreases with increasing transverse compressive stress as one would expect assuming weakest-link failure statistics [88]. The observed independence of failure level to confining stress level contrasts with the findings of the strong dependence of compressive strength on transverse stress for rock and concrete and will be discussed briefly later.

Adams and Sines [90] also investigated the onset of spalling in their tubular Al_2O_3 specimens and found that spalling away from the ends of the specimens initiates at only 25% of failure stress and that a considerable proportion of the surface area of the specimens is spalled at failure. They calculated that a very large number of flaws ($\approx 10^6$ to $\approx 10^7$) initiate cracks prior to final failure.

The effects of strain-rate, temperature and environment on the uniaxial compressive strength of high density Al_2O_3 were studied by Lankford [92,93] using cylindrical rod specimens taking care to avoid misalignment problems and adverse effects of specimen preparation flaws. He reported that the compressive strength increased monotonically with strain rate (up to 45% over nine orders of magnitude increase in $\dot{\epsilon}$) but no significant difference was observed in different environments (air, H_2O and inert atmosphere). The effect of temperature in the range -200°C to 900°C was more complex and similar to the effect on the tensile strength [93]. The strength was observed to decrease with increasing temperature, increase suddenly to a maximum at approx. 200°C and then decrease again. The extrapolated strength at absolute zero was indicated as 4.2 GPa as compared to an ambient temperature value of ≈ 3 GPa. He also carried out acoustic emission and SEM microscopic investigations of deformed specimens and reported that the rate dependent mechanism is deformation twinning which is thermally activated, initiates at 25%-50% of the failure stress level and nucleates microcracks at twin/grain boundary intersections. He found that crack growth is not important until the later stages of microfracture coalescence. It was suggested that twinning was one of the mechanisms of crack nucleation beneath sharp indenters, during impact of sharp particles in erosive situations (in which twinning and associated lateral crack formation [95,96] can persist to high impact velocities) and possibly during tensile deformation at low temperatures.

The compressive strength of only two other ceramic materials was found in the literature: Sines and Adams [84] reported the results of careful experiments on the uniaxial compressive and tensile strength of "82% dense Zirconia" (no other information given) using their specimen configuration as used for the Al_2O_3 tests and found a compressive to tensile strength ratio of ≈ 7.5 . Tappin et al [85] reported biaxial measurements on reaction-sintered SiC tubular specimens. They measured the tensile/tensile and tensile/compressive failure stress for as-sintered, notched and indented specimens and found that although the compressive-tensile fracture ratio at the same transverse tensile stress was approximately constant in all cases at ≈ 6 , the absolute value of the fracture stress decreased from the untreated to the notched to the indented specimens.

The effects of compressive cycling on the crack growth of various ceramics (Al_2O_3 and MgO-PSZ) has been reported by Suresh and co-workers (see e.g. [94]) who found that the application of cyclic compressive loads to notched plates of ceramics leads to stable crack growth in a direction perpendicular to the compressive direction. These findings seem to corroborate the findings reported by Lankford [96] in connection with the nucleation of lateral microcracks at points of compressive impact by sharp particles. They calculated that a far-field compressive stress induces a tensile residual stress at the notch tip and, by considering a number of different brittle systems, developed a generalized constitutive formulation to explain the phenomenon.

Comparison between the compressive fracture characteristics of ceramics and rocks.

It would be instructive to compare the findings reported above on the compressive behaviour of ceramics to those reported for rocks and cements in order to try to arrive at any possible correlations between the bulk and microstructural compressive failure characteristics and the density and distribution of flaws in a brittle material.

Because of their extreme importance in engineering and earth sciences, rocks and concrete are the most widely studied brittle materials both in terms of their compressive failure characteristics and their deformation behaviour. By their nature and processes of formation rocks contain a very large density and wide distribution of flaws such as pre-existing macro- and microcracks, pores, weak grains and interphase boundaries which have been found to be strong crack initiators [65]. The large density of flaws results in a large initial compressive compliance which decreases sharply with increasing applied compressive stress to the level of the compliance of an uncracked solid sample [65,75]. The compressive strength of rocks has been found to be strongly dependent on confining compressive stress with up to a ten-fold increase in compressive strength achieved by a small increment in the mean stress as discussed in [65] and shown in fig.2.5. Similar results have also

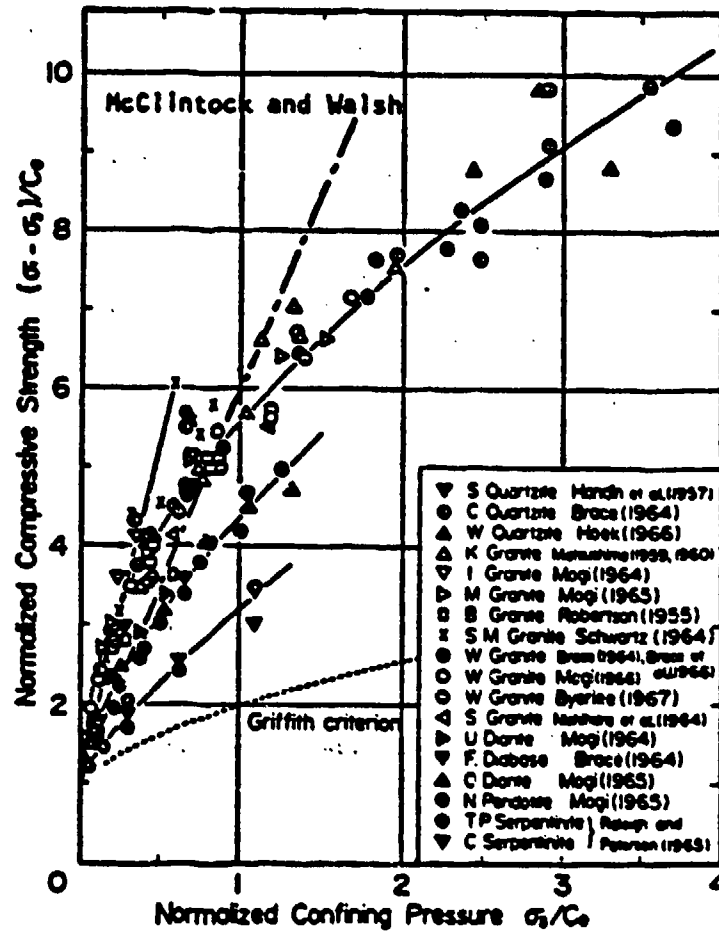


Fig.2.5. Experimental results and comparison with various theories on the relation between compressive strength and confining pressure for rocks tested at room temperature (Ohnaka, 1973). (Referred to in [65]).

been reported for concrete [65]. Brace and co-workers (reported in [65] and [75]) have shown that brittle rocks tested in triaxial compression show dilatancy when the difference between the maximum stress and the transverse stress ($\sigma_1 - \sigma_3$) reaches 1/3 to 1/5 of the maximum value. Significant increase in void density which results in dilatation is due primarily to inelastic deformation in the radial direction which has been attributed to stress-induced microcracking parallel to σ_1 . SEM studies of the micromechanics of dilatancy and compressive fracture by in-situ [97] or post failure [65,75] techniques have shown that the stress-induced cracks are sharp-tipped, relatively straight, are oriented approximately parallel to the maximum compressive stress and are mostly transgranular. Tapponier and Brace [75] have concluded that dilatancy is primarily the consequence of two types of fracture: the widening and extension of pre-existing flaws and the initiation and propagation of cracks at sites with high contrast in elastic moduli such as transverse grain boundaries between different materials. All microstructural studies of compressive fracture indicate that the stress-induced cracks are the result of Mode I growth in tension with no evidence of either Mode II or Mode III growth of pre-existing microcracks prior to the onset of failure. This agrees with the predictions of the microcrack extension models driven by the shear offset of pre-existing cracks. Significantly, localized deformation extending over a continuum element with grains of all mineral types was not observed in any SEM investigation until the sample had been deformed well into the post-failure stage [65]. Thus it appears that a continuum description of the mechanical behaviour of a brittle polycrystalline material such as rock is adequate only over a continuum element large enough for the effects of grain scale inhomogeneity and anisotropy to average out.

The contrasting results on the effects of transverse confining pressure on the compressive strength of rocks and ceramics as discussed above appear to indicate that the crack nucleation and propagation characteristics in the two different classes of brittle materials may be governed by the nature, density and distribution of pre-existing flaws in the samples. As reported by Lankford

[96], crack nucleation and propagation in a high-density high-strength Al_2O_3 ceramic, which contains a very small density of pre-existing microcracks, is governed mainly by the amount of deformation twinning and not as much by extension of pre-existing microcracks as evidenced from his acoustic emission deformation studies. Thus, crack initiation in high density materials appears to be less dependent than the propagation of these cracks, on the level of any transverse compressive stress confining the specimen. The results reported by Sines and Adams suggest however that even crack propagation of initiated cracks is not inhibited to any significant degree by confining pressure. In contrast, the compressive fracture characteristics of rocks, cement and other materials with large densities of pre-existing flaws of various sizes, depend primarily on the extension of existing microcracks by shear offset. Any confining transverse compressive stress would be expected to increase significantly the frictional force across pre-existing crack faces and thus increase the compressive stress needed to initiate and propagate wing cracks in the material. In this regard it would be particularly important to carry out in-situ SEM compressive fracture studies of brittle materials with a wide range of flaw and microcrack distribution in order to ascertain whether there is a threshold microcrack density and/or size at which deformation twinning stops playing an important role in the fracture process and sigmoidal extension of existing microcracks begins to predominate. The future work in this project will attempt to address this question.

2.3. Experimental study of the failure characteristics of a model brittle material.

In order to study the failure mechanisms of brittle materials under compression it was decided to avoid high strength "real" materials that present the normal preparation difficulties and study a model brittle material that could be manufactured easily. The motivation behind this line of action was the need to investigate the effects of flaw distribution and density on the compressive and tensile failure characteristics and possible correlations with the micromechanics of failure.

A number of considerations were taken into account in deciding the material to be used for these studies:

- a. It should be easy to manufacture to various densities.
- b. It should easily allow the incorporation of controlled density and distribution of flaws.
- c. It should not display any microplasticity up to the fracture load.
- d. It should have low enough strength in tension and compression to enable strength measurements at easily accessible loads under various stress states.

A material that appears to incorporate the above properties is Calcium Sulphate Hemihydrate or Plaster of Paris and it was decided to use it as the model brittle material for these studies.

2.3.1. The material

Plaster of Paris is essentially Calcium Sulphate Hemihydrate, $\text{CaSO}_4 \cdot \frac{1}{2} \text{H}_2\text{O}$ and is made by heating gypsum between 120°C - 160°C :



When plaster of Paris is mixed with water the reverse reaction takes place: water is reabsorbed with the formation of gypsum. This takes place by the production of localised regions of gypsum because hemihydrate has about five times the solubility of gypsum in water. The reaction is exothermic and

results in a coherent mass through the interlocking needle shaped gypsum crystals. From the above equation it can be seen that only 18.6wt% water is needed for rehydration. Because the amount of water used in setting far exceeds the amount required for rehydration to enable casting, the excess water evaporates which results in a highly porous product. The true density of the hemihydrate is about 2750 kg/m³ and that of the dihydrate about 2320 kg/m³, so a contraction on setting would be expected but the arrangement of the crystals is such that setting results in a volume expansion of approx. 0.5% (in the case of a mixture of P/W = 100/70 [98]). Some of the properties of the material as found in the literature are tabulated in Table 2.2

Table 2.2. Some properties of Plaster of Paris reported in the literature [98].

Properties of dried mixture with P/W wt.ratio = 100/70

Molecular weight (CaSO ₄ = 93.8%, H ₂ O = 6.2%)	154.16	[99]
Density, Kg/m ³	1.06	
Ult. Compr. Strength, MPa	12.76	
Modulus of rupture, MPa	7.4	
Internal surface area, m ² /kg	~500	
Mean pore radius, μm	~2	
Volume porosity,	~50%	
Permeability to air, cm ² s ⁻¹ /cm water	2x10 ⁻³	
Permeability to water, cm ² s ⁻¹ /cm Hg	10 ⁻⁴	

Set plaster of Paris is very sensitive to any temperature treatment as the hydrated gypsum crystals lose water and convert to hemihydrate with very serious loss in mechanical properties as detailed in the Appendix [98].

The CaSO₄.¹/₂ H₂O starting powder was obtained from British Drug House. All specimens were made by mixing thoroughly a predetermined amount of CaSO₄.¹/₂ H₂O (determined from the preliminary investigations) with distilled water, removing all air trapped in the suspension and casting into split

rectangular (approx.size 10x10x100mm) or cylindrical (approx.size 10mm diameter x 80mm height) moulds shown in fig.2.6 and allowing them to cure for a minimum period of 7 days until fully cured. The effects of curing time, powder to water ratio, curing temperature etc on some mechanical and elastic properties of the specimens are included in the Appendix. Specimens of higher density than that of the as-cast specimens were obtained by forcing some of the water out of the mould immediately after casting. The morphology of as-cast and higher density specimens is shown in fig.2.7. The material appears to be predominantly mechanically bonded with probably some degree of weak chemical bonding between the grains due to the low solubility of CaSO_4 in water. Figure 2.7 shows clearly the high degree of cross-linking and the very high degree of microporosity between the grains due to the water used in the casting process. The grains have a high aspect ration (up to approx. 10) and average size of approx. $2\text{-}3\mu\text{m}$ x $10\text{-}15\mu\text{m}$. SEM examination of the grains after large amounts of deformation indicated that the grains are brittle without any evidence of microplasticity. In addition, the samples contain small numbers of approximately spherical pores probably due to trapped water during casting, which decrease in size with increasing bulk density of the material, as shown in fig.2.8. These pores were found to be the main sources of failure in the material. Great care was taken always during production to avoid contamination of the specimens during casting, such as lint, dust etc.

Determination of the theoretical packing density of the material.

It was found necessary to determine the maximum theoretical density of cast material in order to obtain a quantitative measure of the total porosity of the specimens. The density of set plaster varies widely with preparation conditions and so it was not possible to rely on the density given in the literature. In addition, because of the rehydration reaction the final theoretical density of the material may not be equal to the theoretical density of gypsum. The determination was carried out by compressing constant amounts of water reacted and dried $\text{CaSO}_4 \cdot \frac{1}{2} \text{H}_2\text{O}$ powder isostatically under increasing pressure up to approx. 500MPa and then measuring the density of the

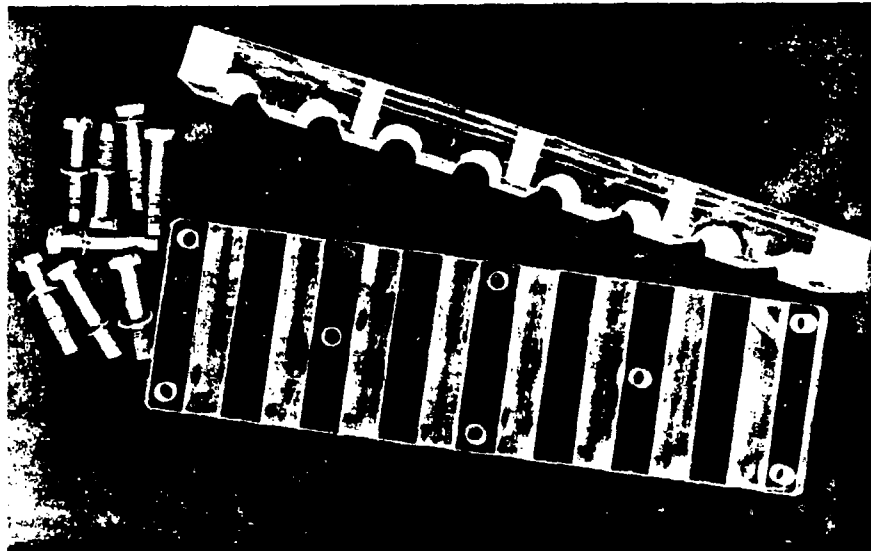


Fig.2.6. One of the split plastic moulds used to cast the CaSO_4 specimens.

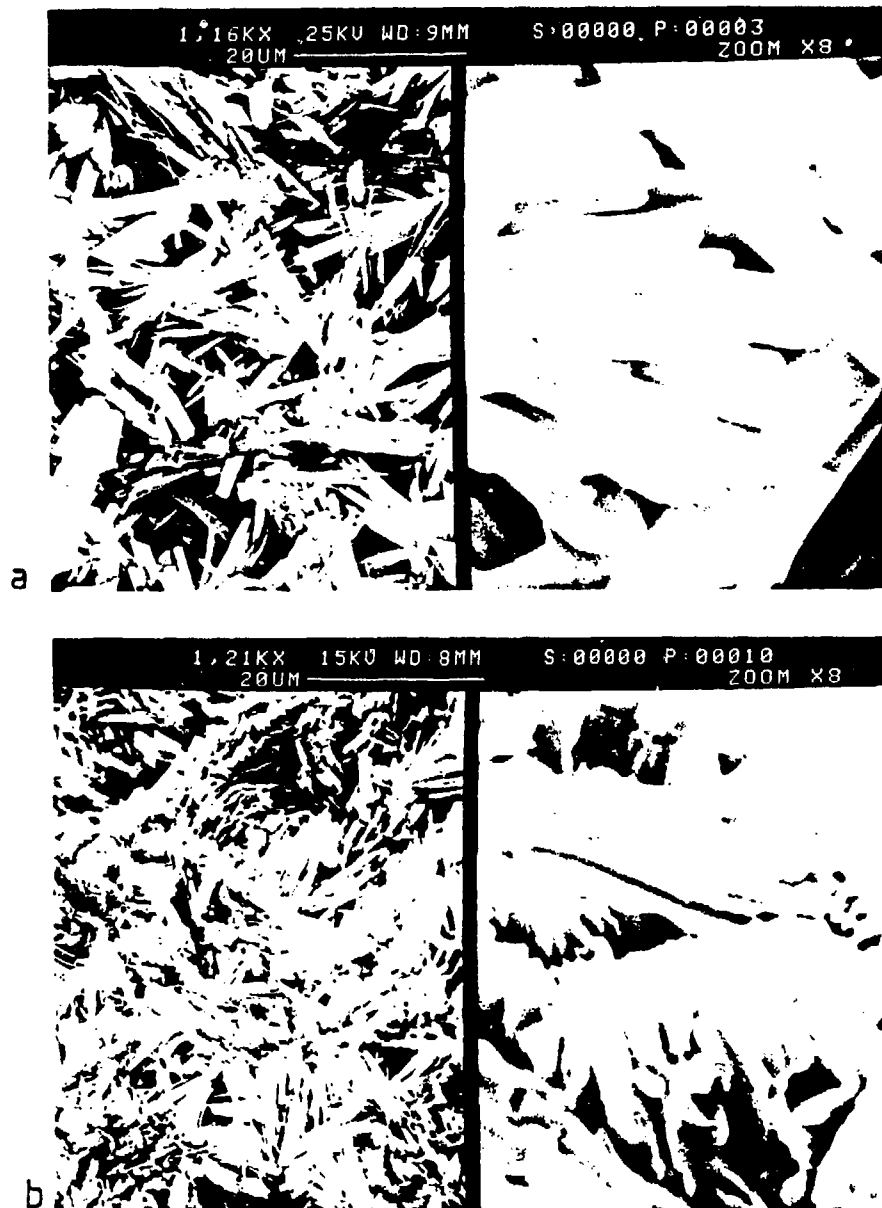
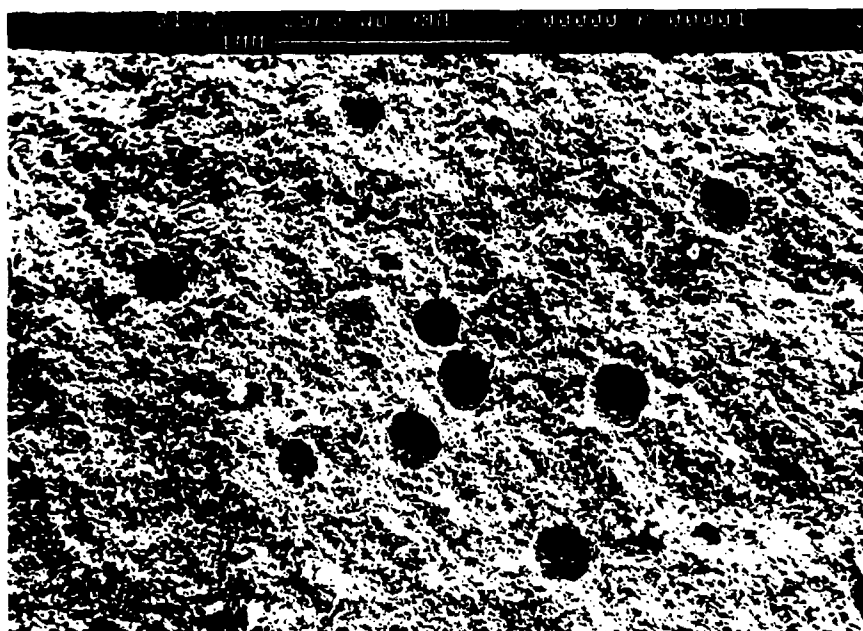
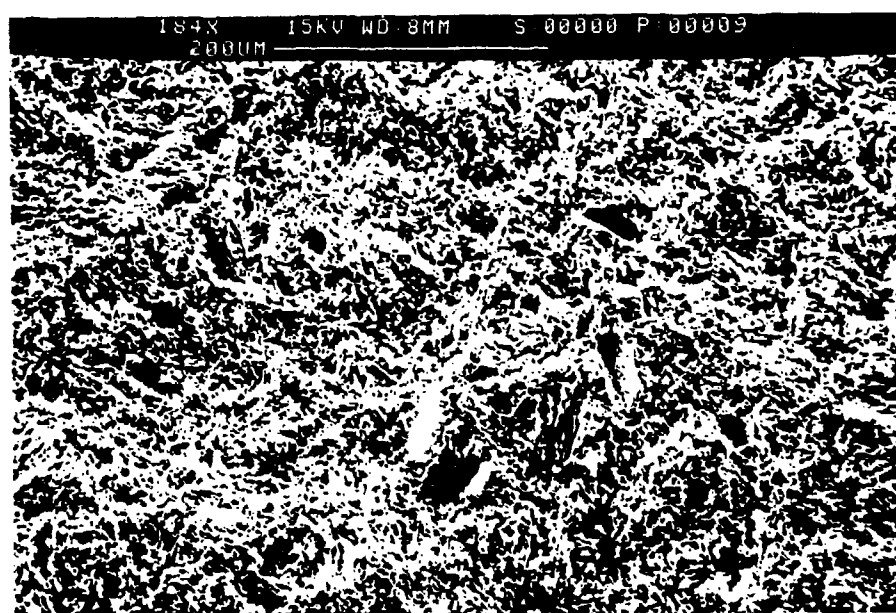


Fig.2.7. Morphology of the Plaster of Paris specimens: a): 50% relative density and b): 70% density.



a



b

Fig.2.8.Low-magnification photographs of fracture surfaces of (a): 50% relative density and (b): 70% relative density specimens.

resulting compacts. The results are shown in fig.2.9. By extrapolation the maximum theoretical density of cast material was determined to be 2.35 kg/m³.

As mentioned, the material contains a large number of spherical pores produced by water trapped in the mixture during casting. These pores were found to decrease in size for the higher density material. From fractographic analysis of fractured specimens it is obvious that they play a major role in the fracture process under all loading conditions. In order to compare the data for crack initiation under compression with the predictions of Ashby et al [66,68], the mean pore size as a function of the density of the specimens was determined by measuring a number of pores (minimum 5 randomly selected fracture surfaces) for each density level. The results are shown in fig.2.10.

2.3.2. The mechanical and elastic properties of the material.

Due to the sensitivity of the elastic and mechanical properties of the material to the various processing parameters and environmental factors (see Appendix) and the scarcity of any reliable information in the literature, it was decided to measure the elastic and the mechanical properties of the material as functions of the relative density and associated pore size prior to investigating its failure characteristics. The properties measured included: the Young's modulus (by four-point bending (E_{bend}) and under uniaxial compression (E_{comp})), the modulus of rupture under 3- and 4-point bending (MOR_3 and MOR_4), the fracture toughness, K_{IC} , by 4-point straight-edge-notched-beam (SENB), the uniaxial tensile strength (σ_t) and the uniaxial compressive strength (σ_c). In addition, the compressive strength under purely hydrostatic conditions was also measured, in order to construct the failure surface of the material and compare with the theoretical predictions (the compressive strength under triaxial axisymmetric conditions will be measured in the immediate future). The results for the as-cast material are summarised in Table 2.3.

CaSO4: Density versus Compaction Pressure

71

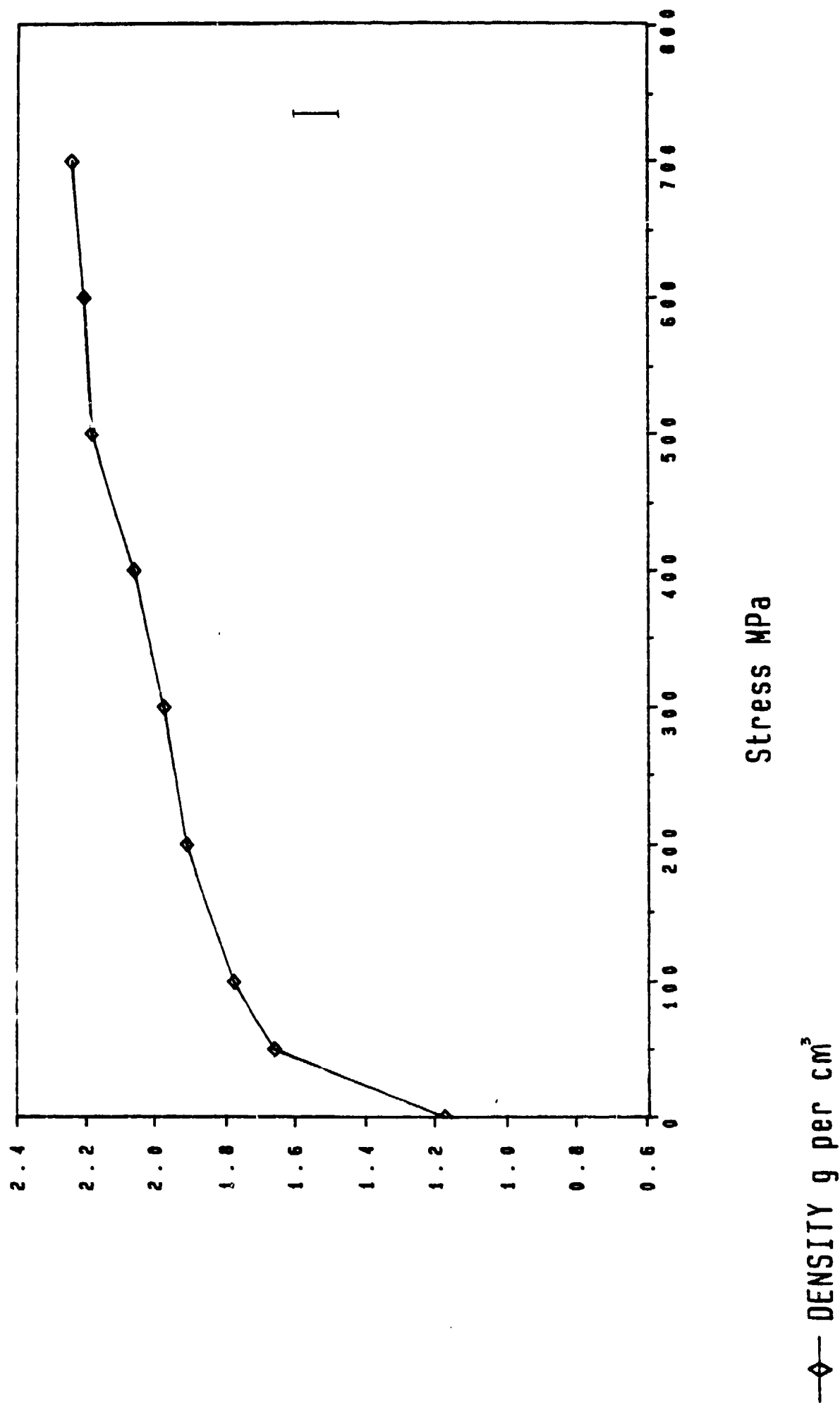
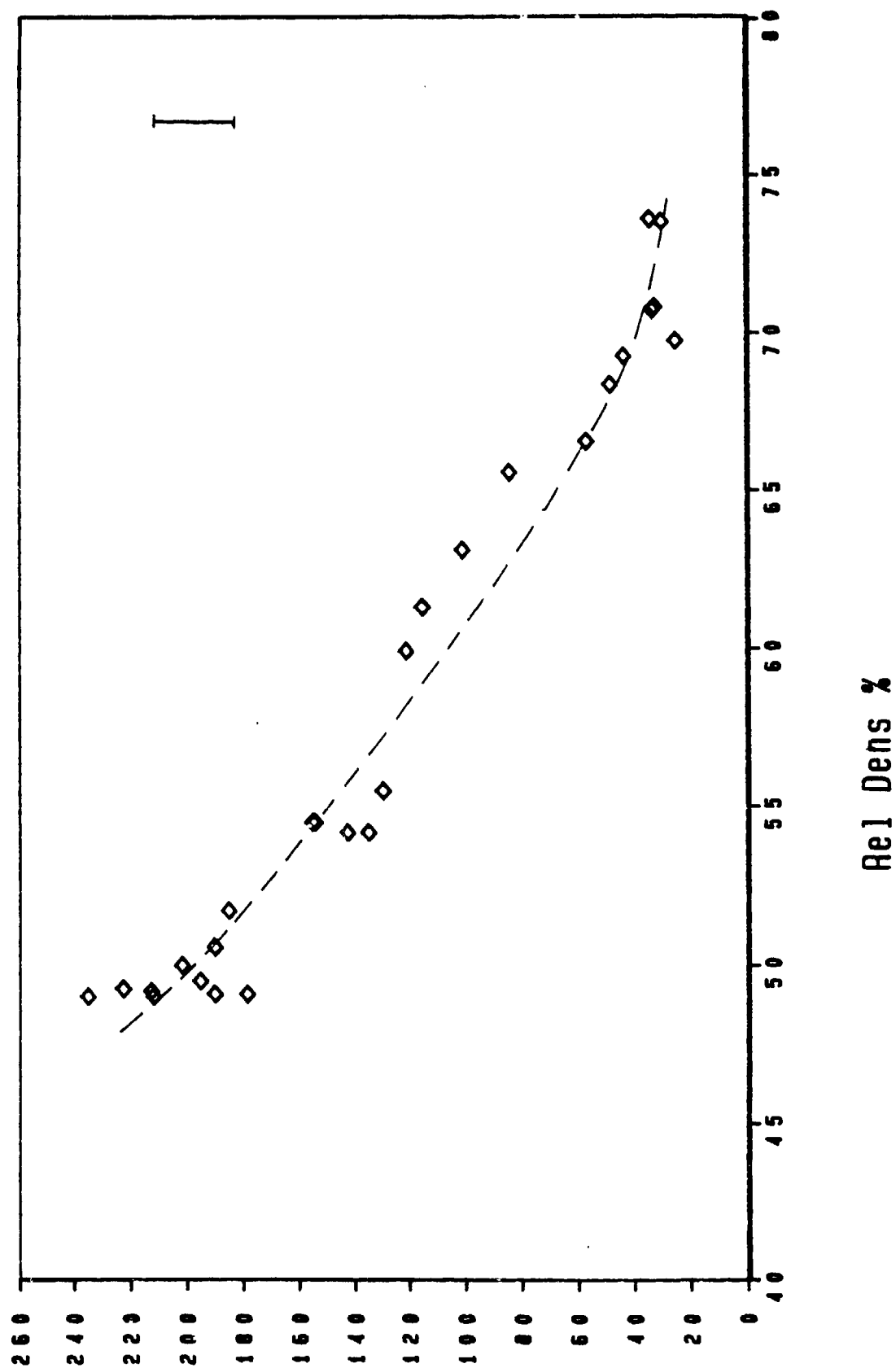


Fig.2.9.The effect of compacting pressure on the density of dry CaSO₄ powder.

CaSO₄: Pore diameter (μm) vs Rel Density



◇ Pore diam μm

Fig.2.10. Macropore diameter as a function of relative density of hydrated Plaster of Paris.

Table 2.3. Summary of the properties of the as-cast material.

<u>Processing parameters.</u>	
Ratio of powder to water, by weight	100:62.5
Curing time, minimum, days	7
Curing temperature, °C	20 ± 5
Relative humidity during curing, %	60 ± 20
<u>Physical properties</u>	
Theoretical density, g/cm ³	2.35
Density, g/cm ³	1.17 ± 0.03
Total porosity content, %	51 ± 2
Mean diameter of spherical macropores, μm	212 ± 18
Mean diameter of micropores, μm	2 ± 1
Mean grain size, μm	3 x 15
<u>Elastic and Mechanical properties.</u>	
Young's modulus, GPa (bending)	4.5 ± 0.1
Young's modulus, GPa (uniaxial compression)	4.6 ± 0.3
Modulus of rupture (3-point bending, 75% water), MPa	5.5 ± 0.7
Modulus of Rupture (4-point bending), MPa	5.8 ± 0.6
Weibull modulus,	6.2
Fracture toughness (SENB), MPam ^{1/2}	0.14 ± 0.015
Uniaxial compressive strength, MPa	14.6 ± 0.9
Hydrostatic compressive strength, MPa	19.2 ± 1.4
Uniaxial tensile strength, MPa	3.2 ± 0.6

a. The bending experiments.

These experiments were carried out to measure both the three- and four-point bending modulus of rupture of the material as well as the Young's modulus in bending. They were carried out using rectangular specimens of cross section 10 ± 0.1mm x 10 ± 0.1mm and a length of approx. 90mm. All the specimens were very lightly ground using 1000 grade SiC paper prior to testing in order to remove the outer layer of the specimens which was found to have a different morphology to the bulk of the specimens. The parallelism of the specimens was within 0.1% (0.01mm). The MOR tests were carried out on a rigid bending jig used predominantly for testing ceramics on an INSTRON 100kN testing press with a 0-100N load cell at a loading rate of 50μm/min and the MOR values were

calculated using the well-known equations:

$$MOR_3 = \frac{Psd}{8I} \quad 2.6$$

$$MOR_4 = \frac{P\Delta s d}{8I} \quad 2.7$$

where

P = fracture load (N)

s = the roller span in the case of $MOR_3 = 51.0\text{mm}$ in all experiments.

Δs = the difference between major and minor spans in MOR_4 .

I = 2nd moment of area of specimen = $bd^3/12$ (b = width of specimen)

d = height of specimen.

All the specimens displayed purely elastic behaviour up to fast fracture and no plasticity was evident in any of the tests. The determination of the Young's modulus of the material was carried out by calibrating the load-extension characteristic of the material using a precision ground steel specimen of identical size to the $CaSO_4$ specimens and calculating the gradient dP/dx of the load-deflection curve. For these measurements it was found necessary to cycle the specimens a minimum of six times by loading to approx. 70% of fracture load until the gradient of the load-deflection reached a maximum (usually after approx. three cycles), prior to calculating the gradient of the curve. This is thought to be due to the need for "bedding in" the specimens on the rollers of the bending jig. It was found that cycling reduced the fracture load substantially probably due to some fatigue microcracking and thus the MOR measurements were carried out on fresh specimens. The Young's modulus for four-point bending was calculated using basic elastic deflection theory as:

$$E_{\text{bend}} = \frac{dP}{dx} \frac{\Delta s^3}{4bd^3} \quad 2.8$$

The final values of MOR_3 , MOR_4 and E_{bend} for the as-cast specimens are tabulated in Table 2.3. and the variation of MOR_4 with relative density and associated pore size is shown in fig.2.11. The variations of the above quantities with processing parameters are discussed in the Appendix.

CaSO4: MOR4 vs Rel Density

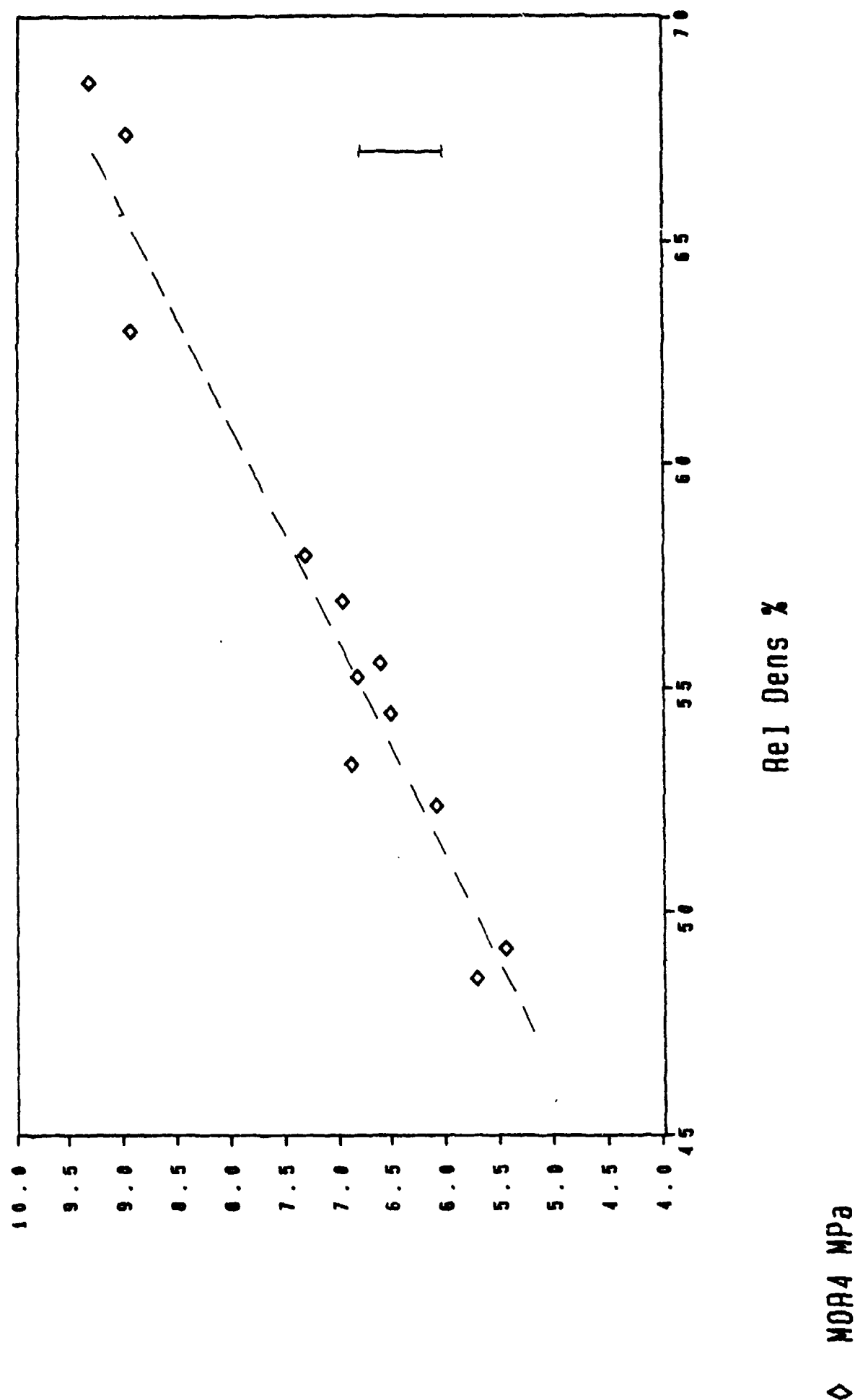


Fig.2.11. Modulus of Rupture in 4-point bending as a function of the relative density.

b. The fracture toughness tests.

The measurement of the fracture toughness of a weak material such as this presents special problems mainly related to the effect of a finite radius of curvature of the notch. However, the microstructure of the material ensured that although the notching of the specimen was carried out using a sharp razor blade of tip radius approx. 0.03mm, there was always a sharp microcrack beneath the notch of depth comparable to the grain size. This was corroborated by the relative insensitivity of the fracture toughness to small variations in notch width. The fracture toughness measurements were carried out on identical rectangular specimens as the ones used for the bending tests in four point-bending using a straight edge notch beam configuration on the INSTRON 100kN testing press using a 0-100N load cell. The loading rate was kept constant at 50µm/min. The calculation of K_{Ic} was carried out using the analysis of Strawley and Gross [100]:

$$K_{Ic} = \frac{P}{b\sqrt{d}} \frac{\Delta s}{d} \frac{3r\sqrt{\alpha}}{2(1-\alpha)^{3/2}} \quad 2.9$$

where $r = 1.9887 - 1.326\alpha - (3.49 - 0.68\alpha + 1.35\alpha^2)\alpha(1-\alpha)/(1+\alpha)^2$

$\alpha = a/d$, a = notch depth

P = load at fracture, N.

b = width of specimen

d = height of specimen

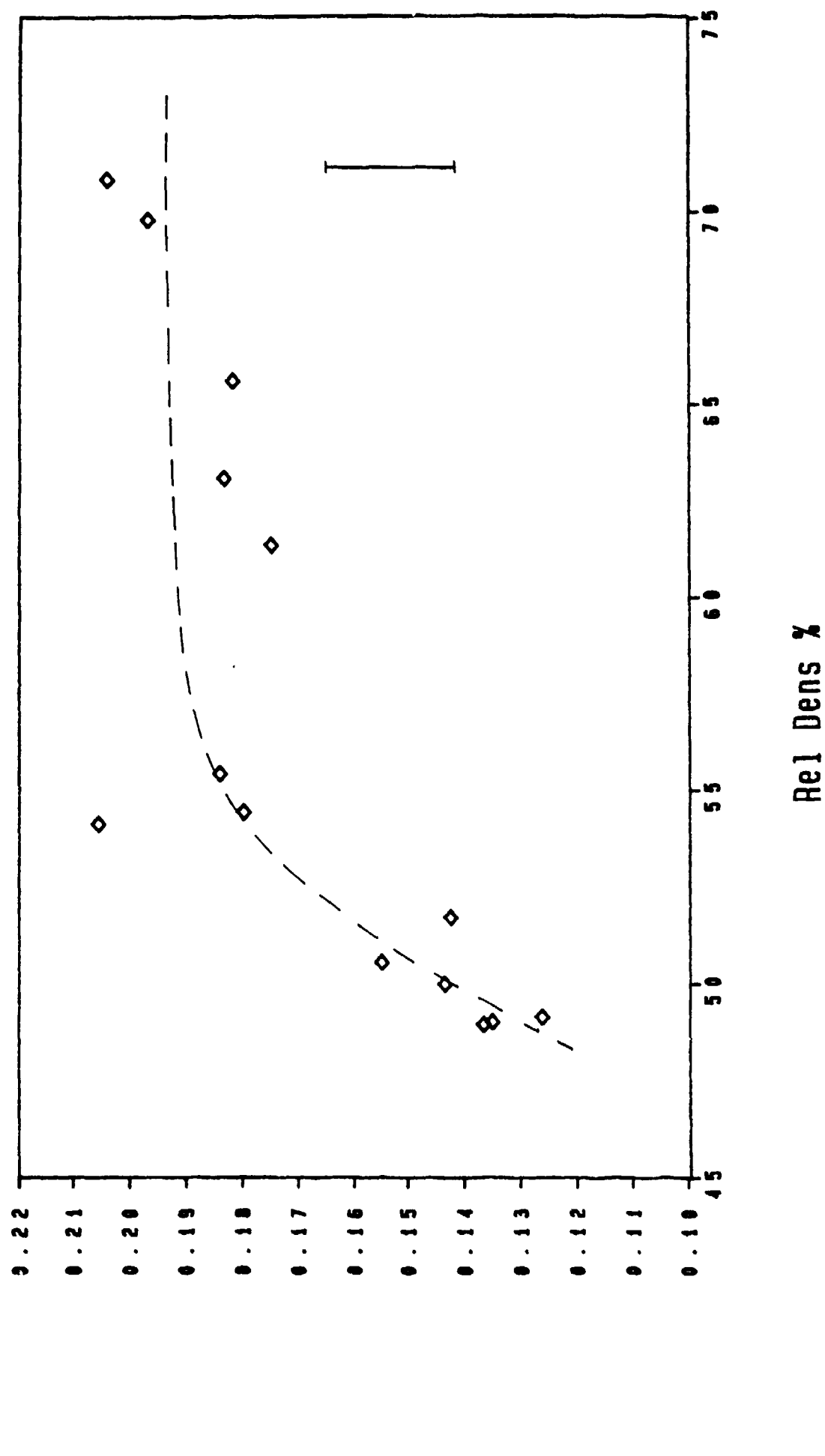
Δs = span difference in 4-point bending.

The K_{Ic} value for as-cast material is included in Table 2.3. The variation of K_{Ic} with relative density and associated pore size is shown in fig. 2.12. The variation of K_{Ic} with processing parameters is discussed in the Appendix.

c. The tensile strength tests.

These proved to be the most difficult tests to carry out due to the extreme difficulty in aligning the samples and their very low strength. In order to

CaS04: Kic vs Rel Density



◇ K_{IC} $\text{MPa m}^{1/2}$

Fig.2.12.Fracture Toughness, K_{IC} , as a function of the relative density.

avoid any misalignment bending stresses as well as premature cracking of the specimens in the grips, special rubberised split grips were designed which provided effective gripping of the specimens without high hoop stresses. The tests were carried out with cylindrical gauged specimens on the INSTRON 100kN testing press using a 0-100N load cell with self-aligning specimen holders at a loading rate of 50 μ m/min. The specimens were aligned extremely carefully and only results of specimens that fractured in the middle of the gauge length were accepted. The specimen shape and size is shown in fig.2.13 together with the rubberized grips. In all tests the specimens displayed pure elastic behaviour without any evidence of plasticity up to the fracture load. The results are tabulated in Table 2.3 and the variation of σ_t with relative density and associated pore size is shown in fig.2.14. No experiments were carried out on the effect of processing parameters on the tensile strength.

d. The uniaxial compression tests.

These tests were carried out on cylindrical as-cast and high density specimens using the INSTRON 100kN testing press with a 0-5kN load cell at a loading rate of 100 μ m/min. To avoid possible misalignment problems the specimens were prepared very carefully prior to testing by grinding the ends manually on 1000 grade SiC paper using a specially designed spring loaded polishing jig. This preparation procedure resulted in parallelism to better than 5 μ m/cm and perpendicularity with respect to the sides of better than 0.2°. To avoid chipping and spalling of the ends of the specimen and reduce friction between anvils and specimen surface, soft paper shims were used in all tests. All the tests displayed a significant amount of dilatation after macrofracture initiation (as evidenced by a sudden change in the gradient of the load-contraction curve) and, near final fracture the specimen displayed very strong pseudo-plastic characteristics. On failure, the load dropped by approx. 20%-25% of fracture load and then displayed cyclic behaviour indicating very stable crack propagation. In most cases the cyclic behaviour continued even after a total strain of up to 15% with only minor reduction in the load range between min and maximum, as shown in fig. 2.15 which is a load-contraction curve for one of the tests. Later in-situ optical and SEM

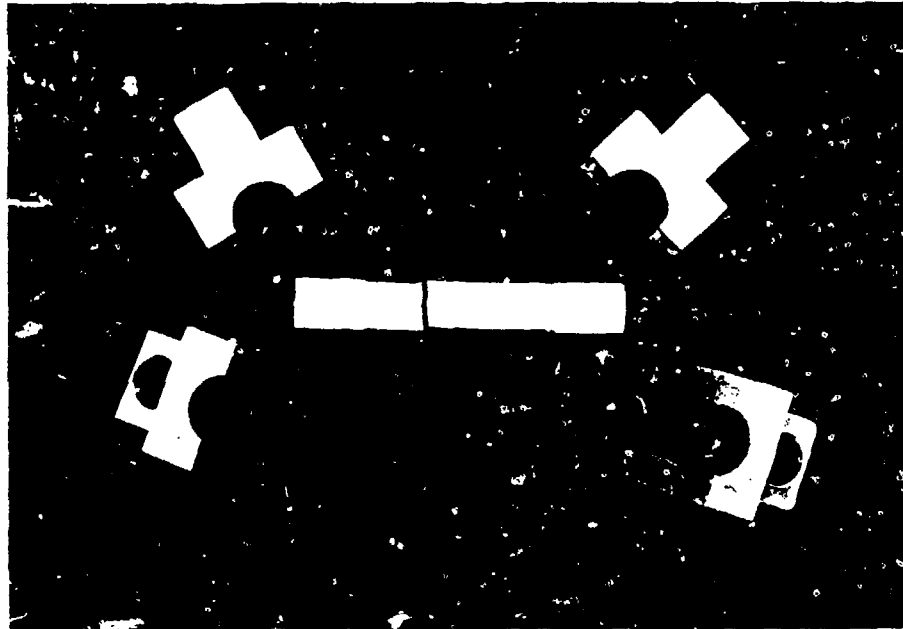
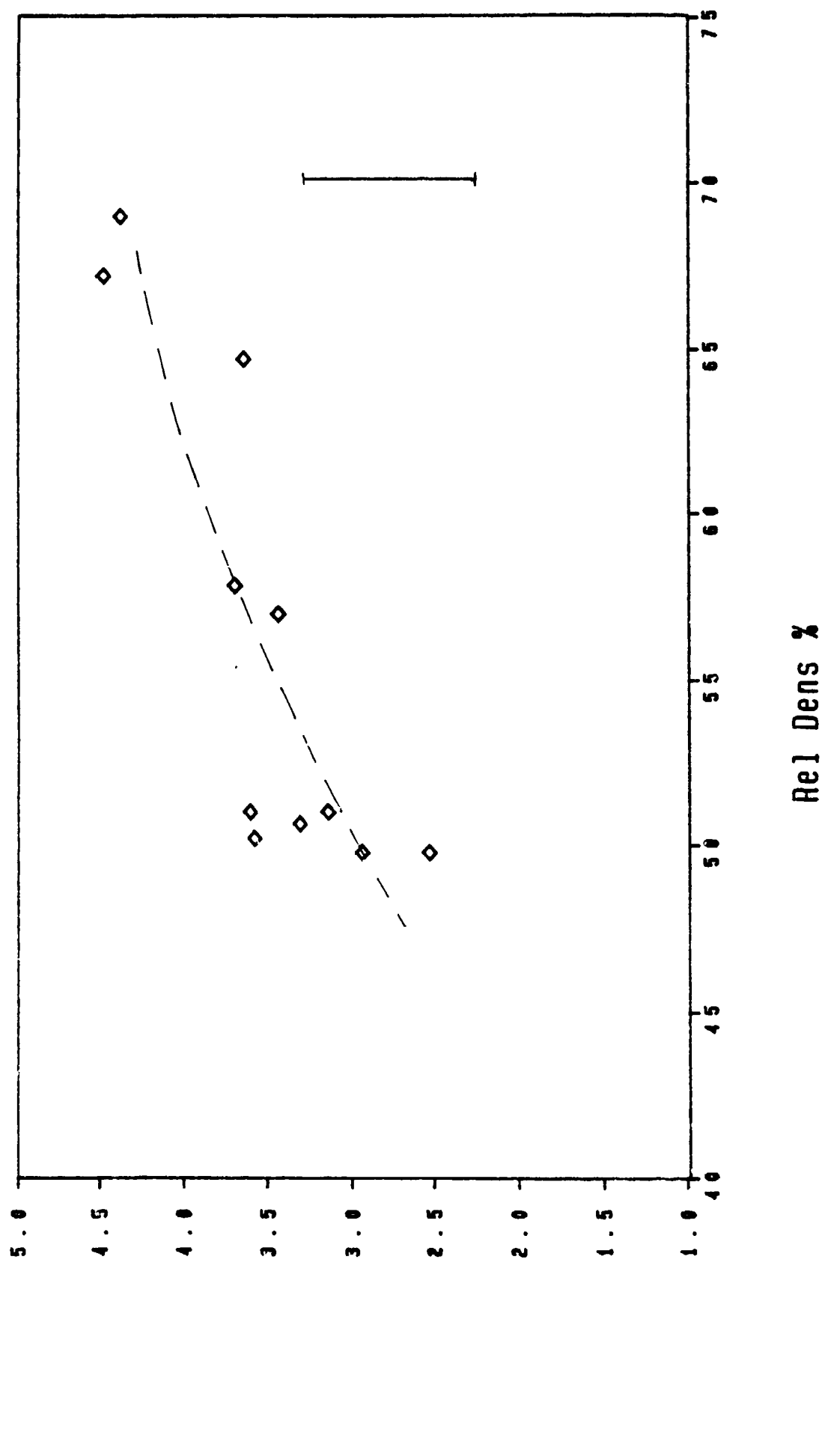


Fig.2.13.One of the tensile specimens used for measuring the tensile strength.

CaS04: Tensile strength vs Rel Density



◇ Fract Stress MPa

Fig.2.14.Tensile strength as a function of relative density.

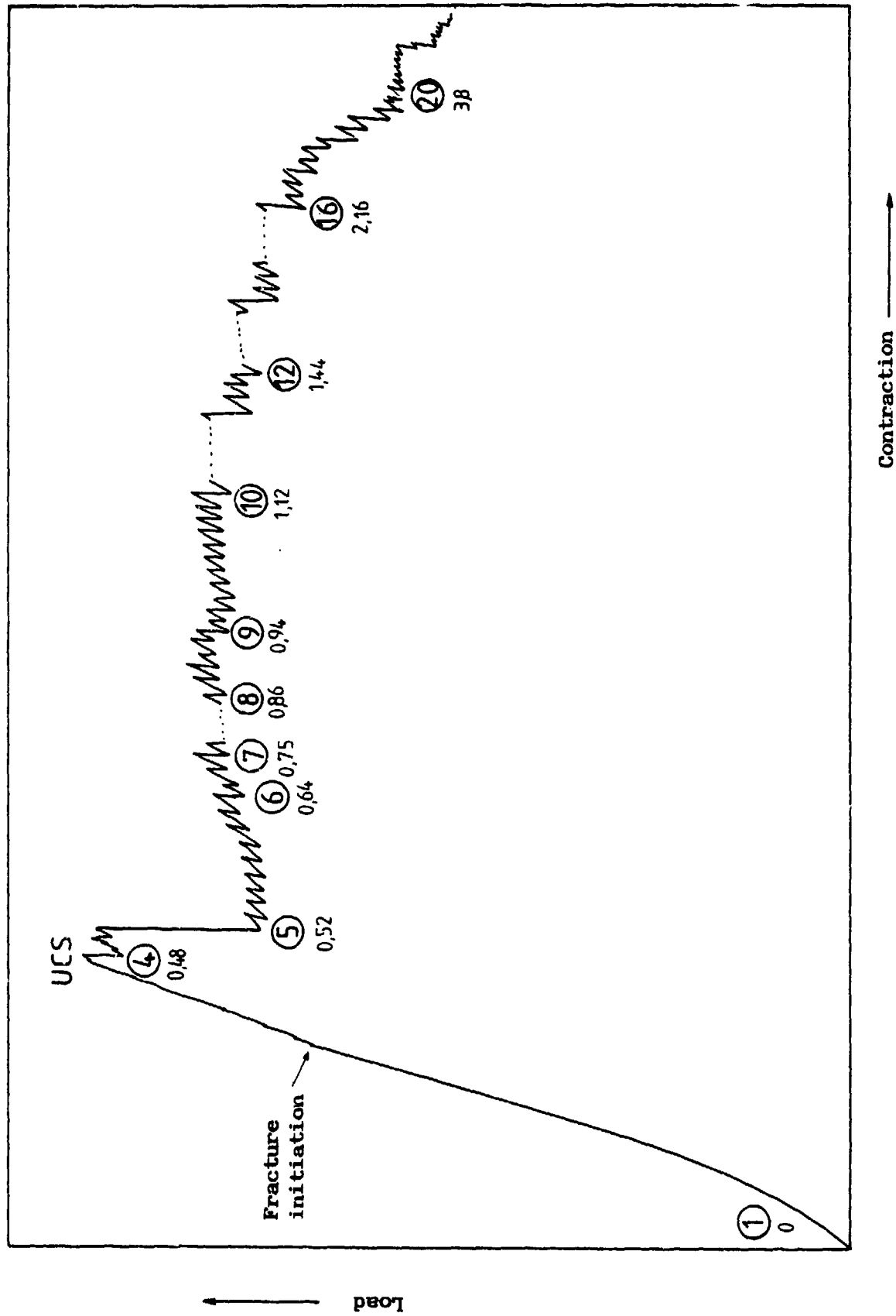


Fig. 2.15. Load-contraction curve for a specimen tested in uniaxial compression. Circled numbers refer to optical photographs in fig. 2.25. Numbers below circles are nett strain (%).

observations of the fracture process indicated that in most cases the initial drop in load corresponded to a shear crack at approx. 30° to the compression axis whereas the load cycling corresponded to the development of longitudinal and further shear macrofractures.

The Young's modulus, E_{comp} , of the specimens was calculated from the gradient of the load-contraction curve after calibrating the system with a precision ground WC-Co cylindrical sample of similar dimensions. The Young's modulus obtained from these tests was found to be very close to the value obtained from the bending tests. The final results for the as-cast specimens are included in Table 2.3. The variation of compressive fracture initiation and final fracture stress and Young's modulus with relative density and associated pore size are shown in fig.2.16 and 2.17 resp. The variation of the compressive strength and Young's modulus with processing parameters is shown in the Appendix.

e. The hydrostatic compression tests.

These tests were carried out as part of the construction of the failure surface of the material (see next section) and in order to compare the results with the theoretical predictions. The specimens used for these tests were short cylinders of approx. size 10mm diameter x 10mm height. The isostatic compression conditions were achieved by enclosing the specimens in a double latex rubber sheath and then pressurizing the encapsulated specimens in distilled water in specially designed PTFE capsules in a high-pressure vessel as shown in fig.2.18. This arrangement has been used successfully before by one of the authors to compress single crystals up to pressures of more than 1 GPa. This is achieved by the use of the double "O" rings to form a compressive seal with the PTFE plug and cup. The arrangement ensures also that no air is trapped in the capsule since it seals hydrostatically only on application of a significant pressure. The tests were carried out on the INSTRON 100kN testing press with a 0-100kN load cell at a load rate of $100\mu\text{m}/\text{min}$. All the specimens displayed an elastic response up to the point of fracture initiation which was evidenced by a change in linearity of the curve with associated small steps.

CaS04: UCS and Fract Init vs Rel Density

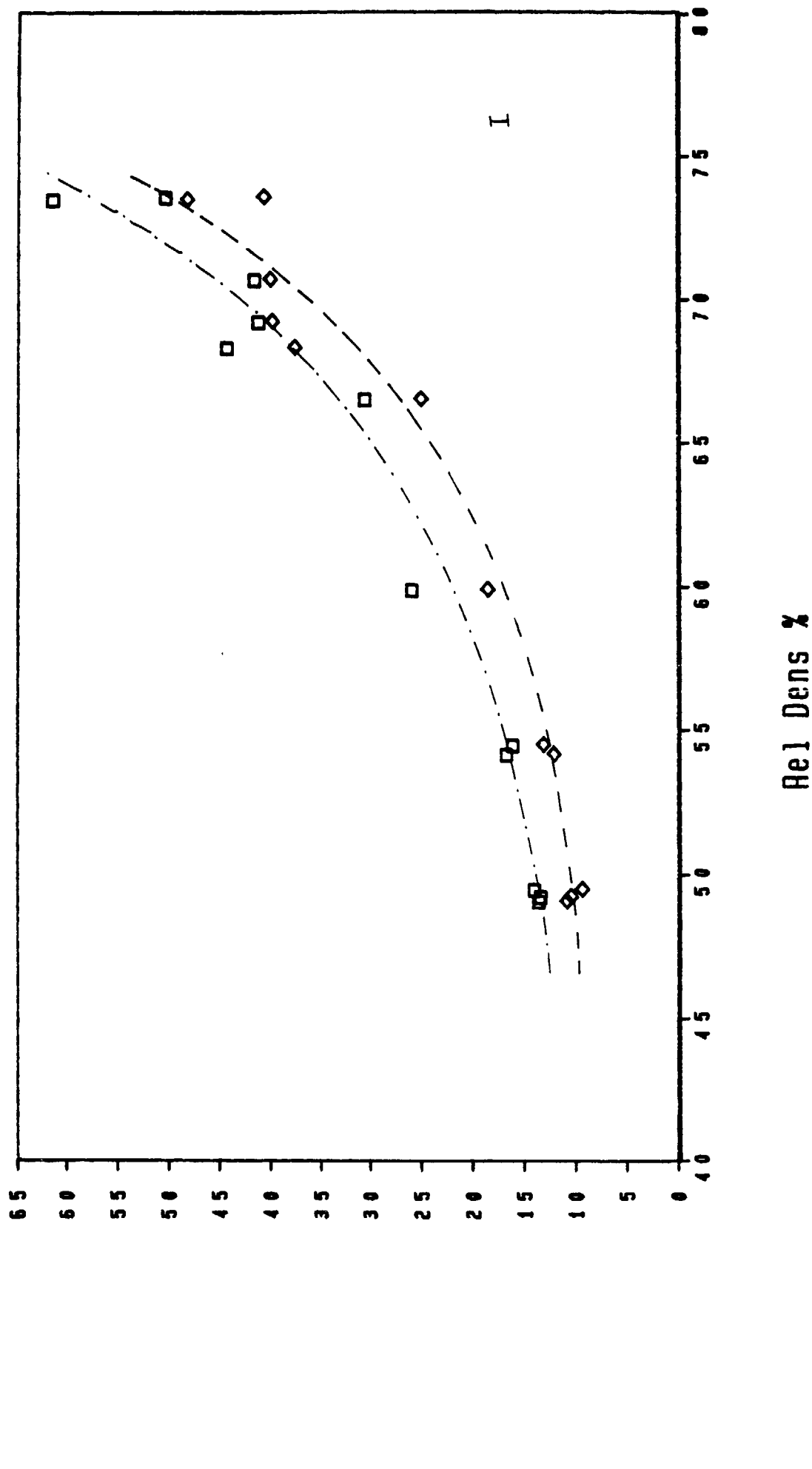
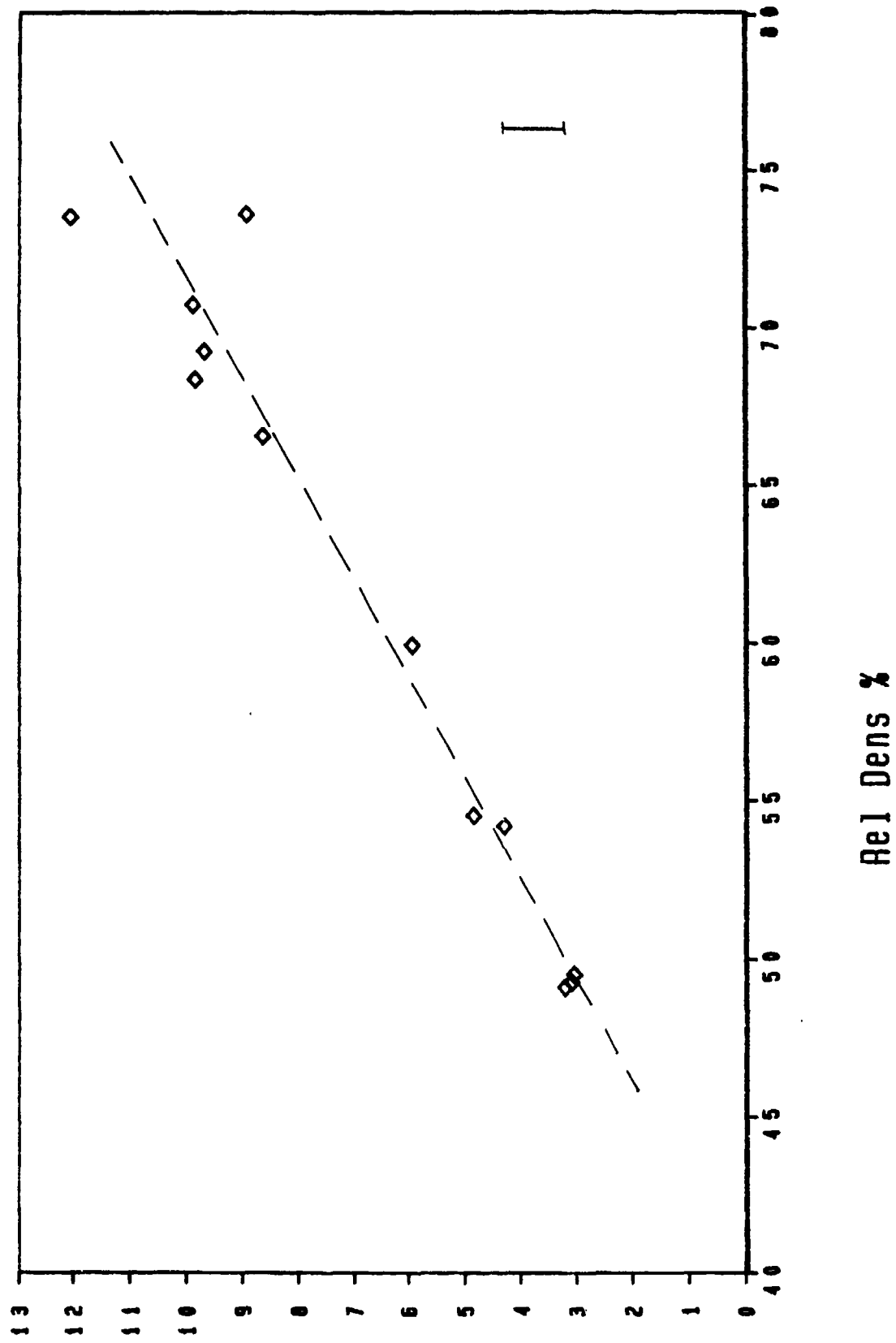


Fig.2.16.Uniaxial compressive strength and fracture initiation stress (first non-linearity of σ - ϵ curve) versus relative density.

CaSO4: Ecomp vs Rel Density



◇ Ecomp. GPa

Fig.2.17. Young's Modulus in uniaxial compression as a function of relative density.

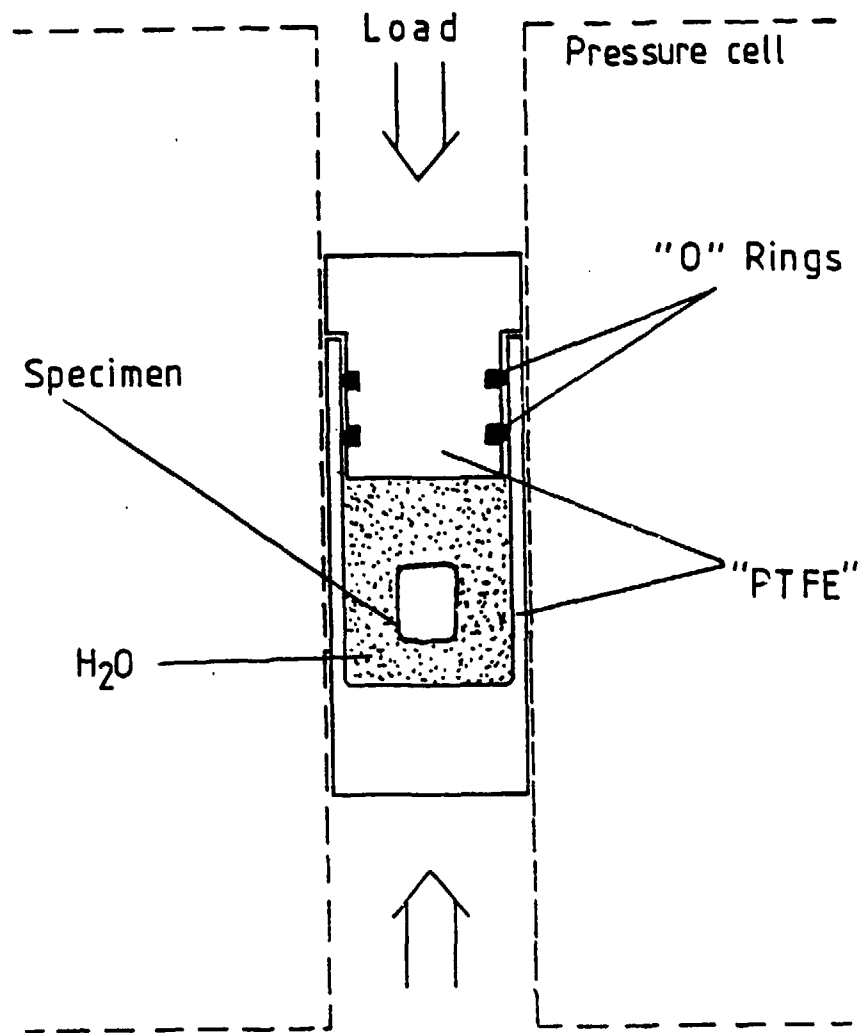


Fig.2.18. The PTFE cell used in the Hydrostatic compression experiments

In addition, some pseudoplasticity was observed prior to final collapse. At final collapse the load dropped by varying amounts depending on the specimen probably due to different size of the fracture initiating pores. After this initial collapse the load recovered slowly to load levels higher than the initial collapse value as the specimen was compacted by the hydrostatic stress as shown schematically in fig.2.19. Some cycling was observed after the initial collapse in this case as well but the load fluctuations ranged over a smaller amplitude. The final results for the as-cast material are tabulated in table 2.3 and the variation of α_{hydr} with relative density and associated pore size is shown in fig.2.20.

f. The axisymmetric compression tests.

These tests have been planned to be carried out in the immediate future in order to try to obtain information on triaxial compressive stress failure characteristics and thus they will only be introduced here very briefly. They will be carried out on enclosed specimens using the compression cell arrangement shown in fig 2.21. The confining pressure will be provided hydrostatically by a hydraulic piston enclosing the main piston which will provide the axial compressive stress. The failure characteristics will be monitored by recording changes in the axial load-contraction curve under various confining pressure conditions.

2.3.3. The failure surface.

The failure surfaces of the material at three density levels have been calculated from the results obtained above and are shown in fig.2.22. where it has been assumed that the failure characteristics are symmetric about $\sigma_1 = \sigma_3$. It can be seen that the failure envelope increases very significantly with decreasing porosity content (from 50% porosity to approx. 30% porosity) (or pore size). The stress for fracture initiation appears to be approx. 80% of the maximum stress at fracture in the case of uniaxial compression and about 60% in the case of hydrostatic compression depending on the density of the material, whereas the fracture initiation stress under tension coincides with the maximum stress at fracture as would be expected for a brittle material.

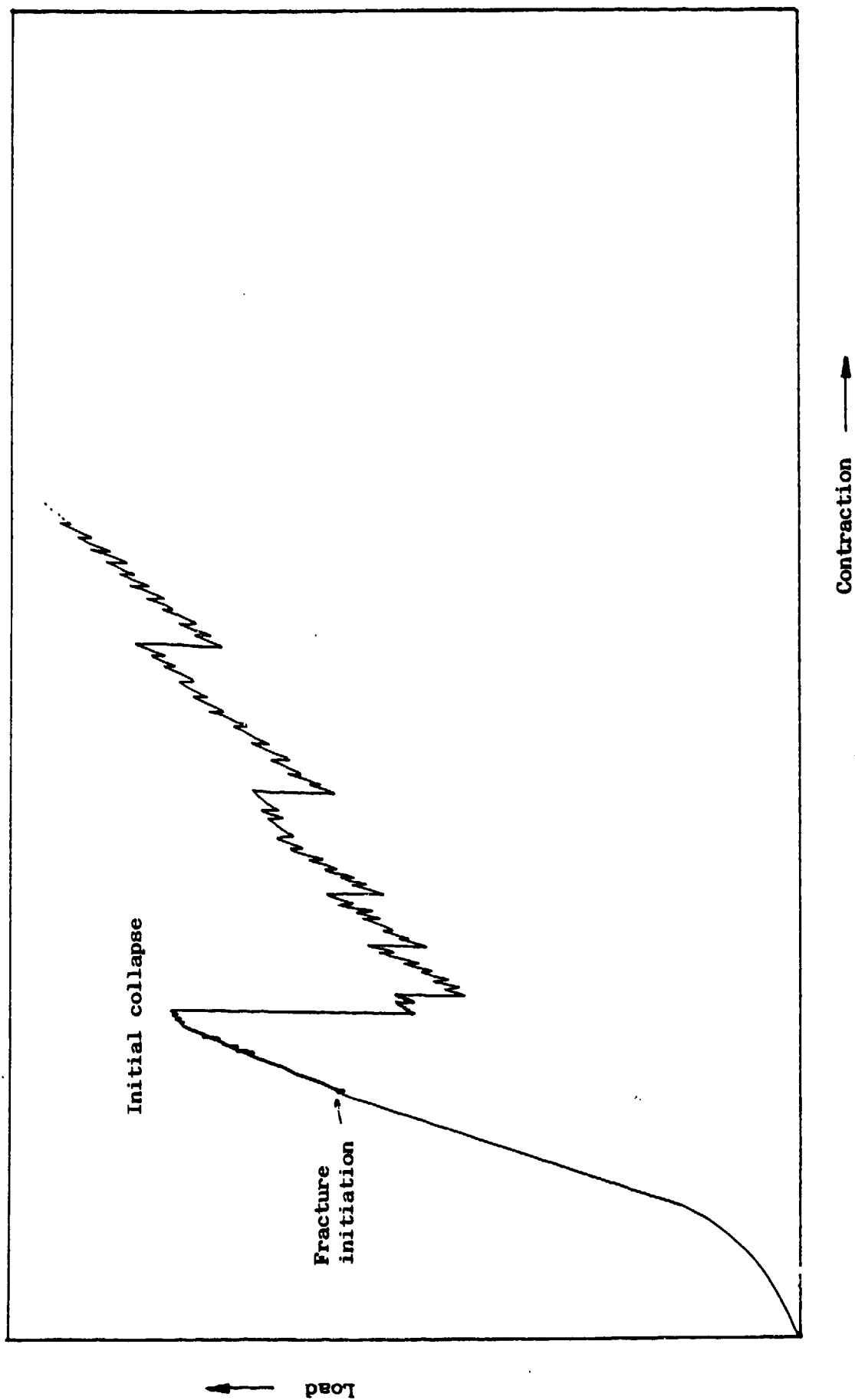


Fig. 2.19. Load-contraction curve for a specimen tested in hydrostatic compression.

CaSO4: UCS (hydr) and Fract Init vs Rel Dens

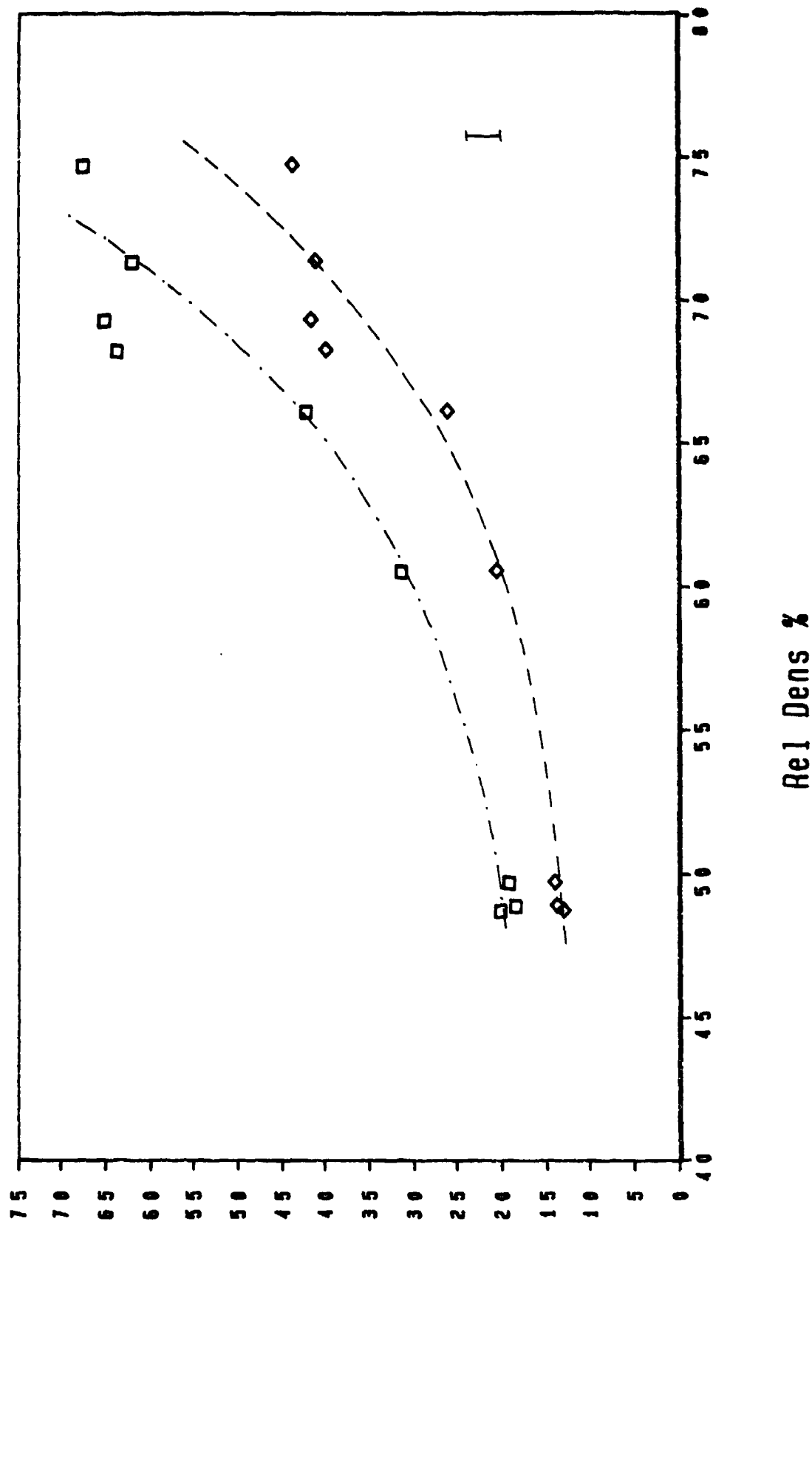


Fig.2.20.Ultimate hydrostatic compressive strength and fracture initiation stress as a function of the relative density.

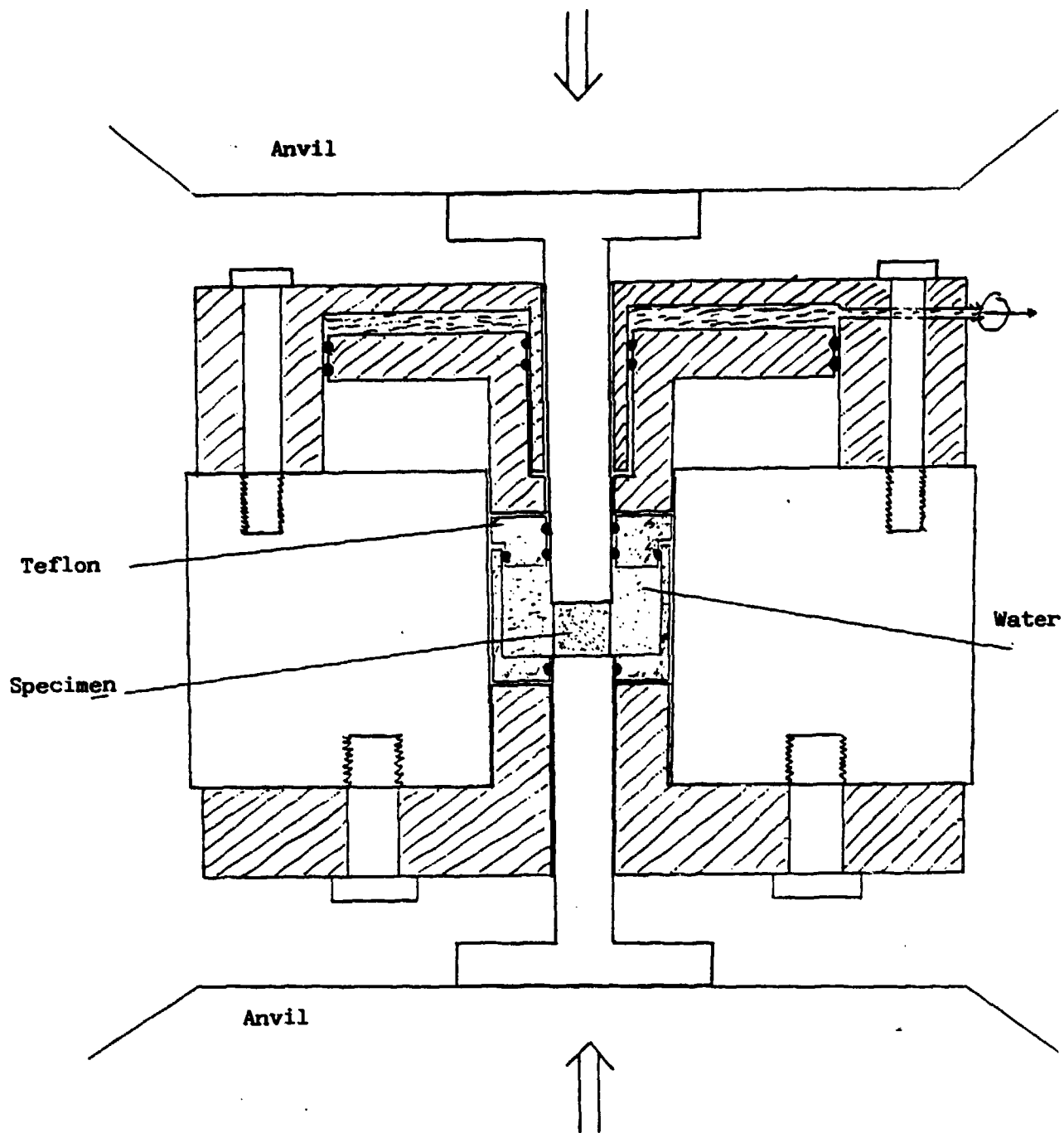


Fig.2.21. The proposed triaxial pressurization arrangement

CaSO4:Fracture initiation surfaces

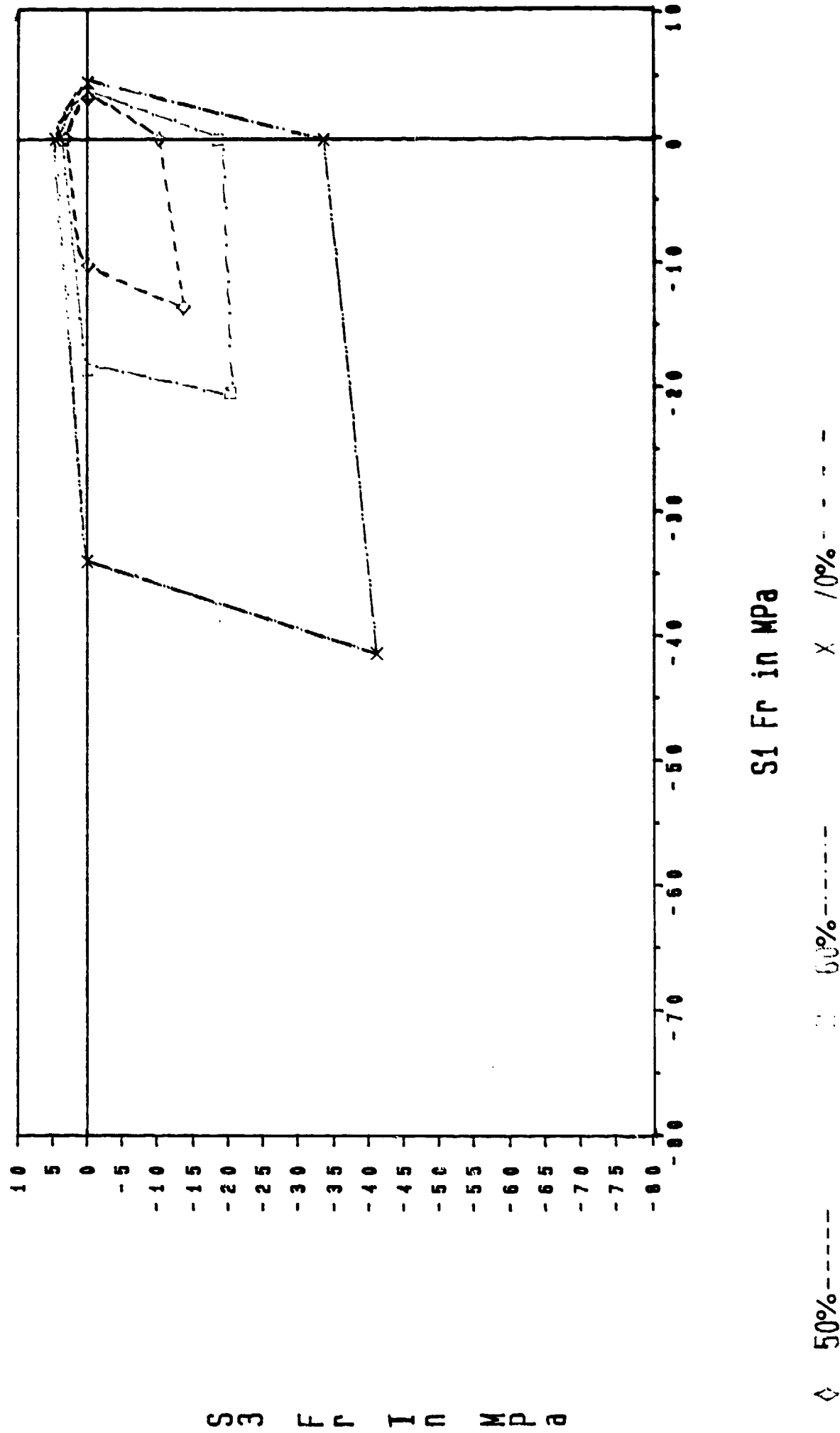


Fig.2.22a.Fracture initiation stress surfaces for Plaster of Paris for three densities.

CaSO4: Final fracture surfaces

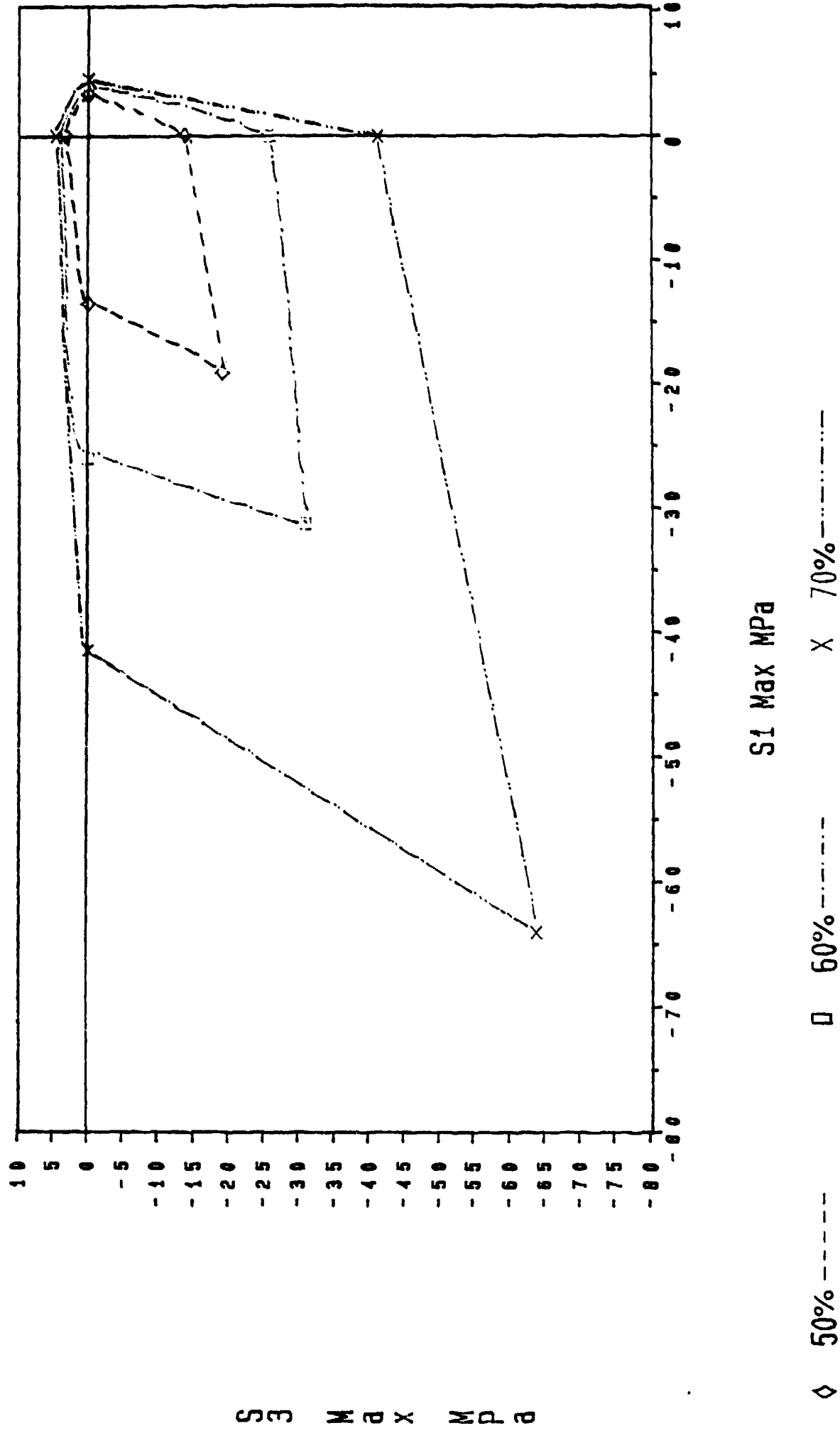


Fig.2.22b.Final fracture surfaces for Plaster of Paris of various densities.

The present results may be compared with the predictions of Ashby and co-workers [66,68] on the initiation of compressive fracture:

In the case of uniaxial compression $\sigma_3 = 0$ and equation 2.1 simplifies to:

$$\sigma_1 = -1.6K_{IC}/\sqrt{\pi a_p} L_0 \text{ (holes) or } \sigma_1 = -3.1K_{IC}/\sqrt{\pi a_c} \text{ (cracks)} \quad 2.10$$

where a_p and a_c are the dimensions of pores and the cracks respectively.

and thus a plot of uniaxial fracture initiation stress (as determined by the first non-linearity of the load-contraction curve) versus $K_{IC}/\sqrt{\pi a}$ should be linear through the origin and yield a "best-fit" value for L_0 . The plot is shown in fig. 2.23 and shows that the fracture initiation model fits the observations very well and the calculated (best-fit) value for L_0 is ≈ 1.5 . which is reasonable considering the morphology of the material (the needle-like crystals increase the effective flaw size of a pore by many times and thus the far-field effect can be considered as large crack).

In order to compare the hydrostatic compression model introduced in section 2.1 above (equation 2.5) with the results obtained in this work, the hydrostatic fracture initiation stress, p_{in} has been plotted versus $(1-f)K_{IC}$ in fig.2.24. It is clear that the results can be described quite well by a linear relation through the origin as suggested by the model. From this graph the "best-fit" value of r/a is ≈ 1.2 which agrees with the "critical" r/a value predicted by the model and with the value of L_0 found for the uniaxial compression case above. Thus fracture initiation in this material occurs very close to the pore surface as predicted by the model. More work will be carried out in this regard to assess further the feasibility of this model.

Due to the fact that no triaxial axisymmetric experiments have been carried out as yet, it is not possible to fully analyse the failure surface with respect to the effects of stress system and microstructure on the failure characteristics. It will be analysed and discussed in detail in the near future.

Uniaxial Compression Fracture Initiation

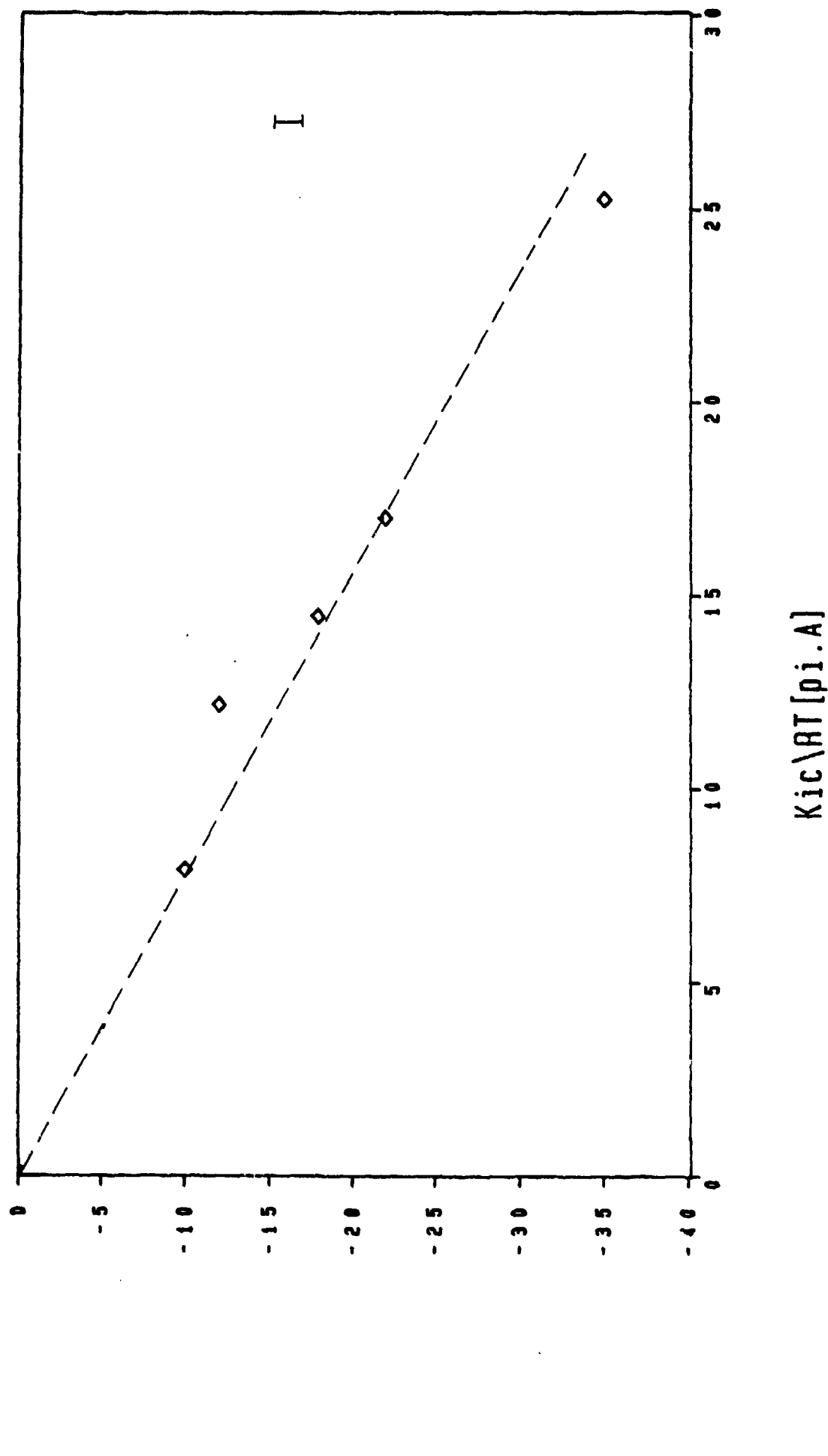


Fig.2.23.Uniaxial fracture initiation stress of Plaster of Paris: Comparison with model of Sammis and Ashby [70].

Hydrost. Compression Fracture Initiation

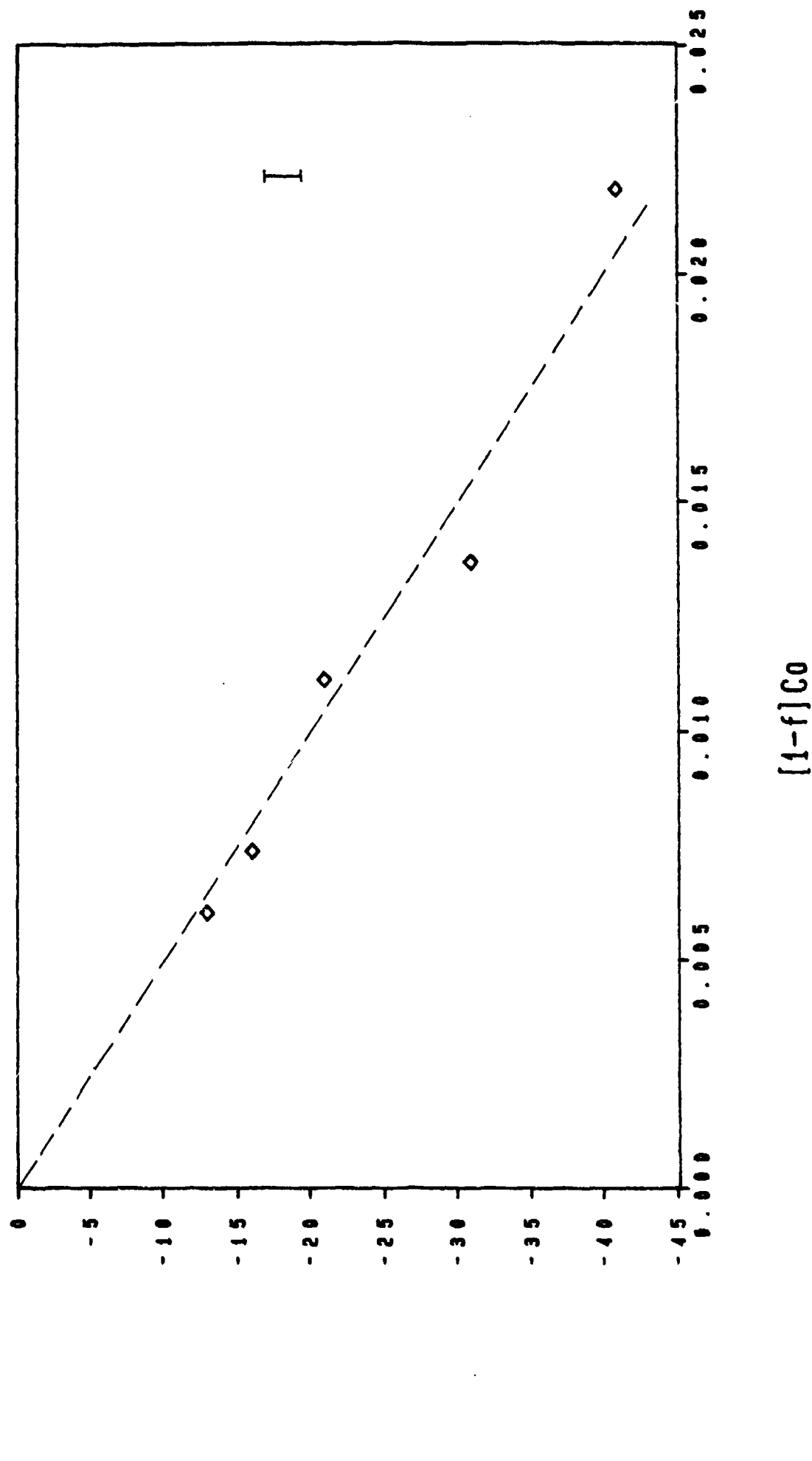


Fig.2.24. Hydrostatic Fracture initiation stress of Plaster of Paris:
Comparison with pore model proposed in section 2.1.

2.3.4. In-situ optical and SEM observations of fracture under compression and the compressive fracture characteristics of $\text{CaSO}_4 \cdot \frac{1}{2} \text{H}_2\text{O}$.

In order to study the fracture characteristics of the material under compression two in-situ studies of fracture under uniaxial compression were carried out, firstly with optical microscopy and secondly in the Scanning Electron Microscope. In the case of optical microscopy this involved the use of a 35mm camera fitted with a macro-lens to enable focusing at a long distance at a maximum magnification of approximately 4x. A number of photographs were taken for a number of compression tests at irregular intervals and one set of results are shown in fig.2.25 which corresponds to the load-contraction curve shown schematically in fig.2.15. In the case of the SEM studies the specimens were compressed using an instrumented compression jig shown in fig.2.26 especially designed for uniaxial compression with capabilities of compression at low load rates. All the in-situ tests were recorded on video which, in conjunction with the load-contraction diagram, enabled accurate analysis of the fracture process. The specimens used for the in-situ observations were rectangular to enable accurate focusing during observation. A series of photographs of an SEM in-situ test of an as-sintered specimen is shown in fig.2.28.

By examining these figures and taking into consideration the fracture characteristics of all the specimens a number of observations may be made for uniaxial compression:

a. In most cases fracture was initiated by the formation of a shear macrocrack which was oriented at approximately 30° - 45° with the compression axis. In many cases this shear crack was axisymmetric resulting in a cup-and-cone type of failure as shown clearly in fig.2.27a. This initial crack precipitated a load drop of approx. 25% of fracture load. In almost all cases the shear crack nucleation site could be identified as a large flaw on the surface (pore etc) (fig.2.28).

b. In some cases, on increasing strain, there was a small recovery of the load ($\approx 10\%$) and a further drop due to the propagation of a second shear crack

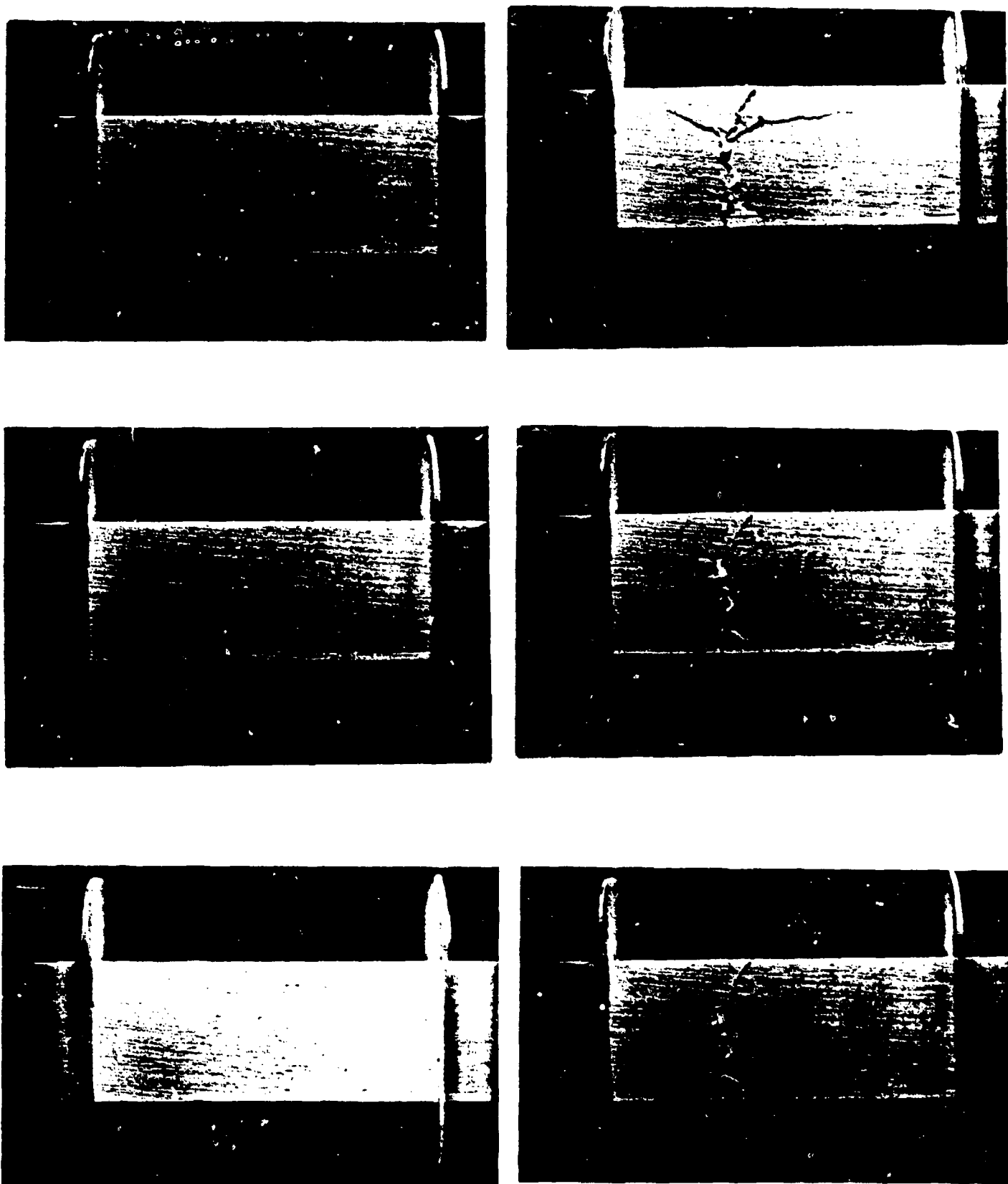


Fig.2.25.Sequence of optical photographs of a Plaster of Paris specimen being tested under uniaxial compression. Refer to fig.2.15. for the relevant load-contraction curve.

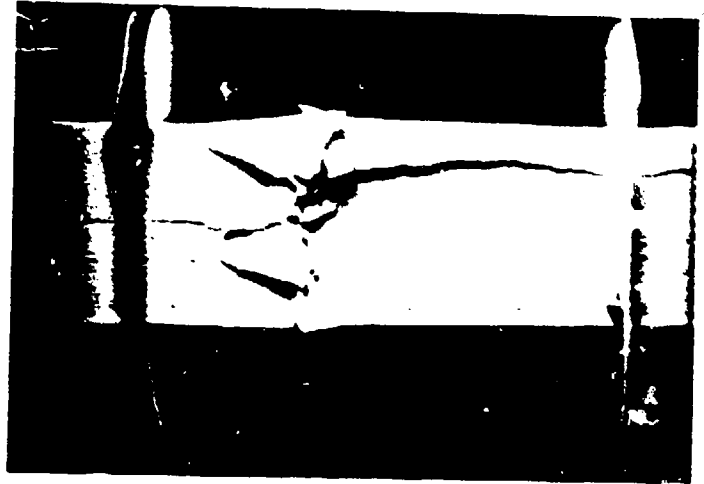
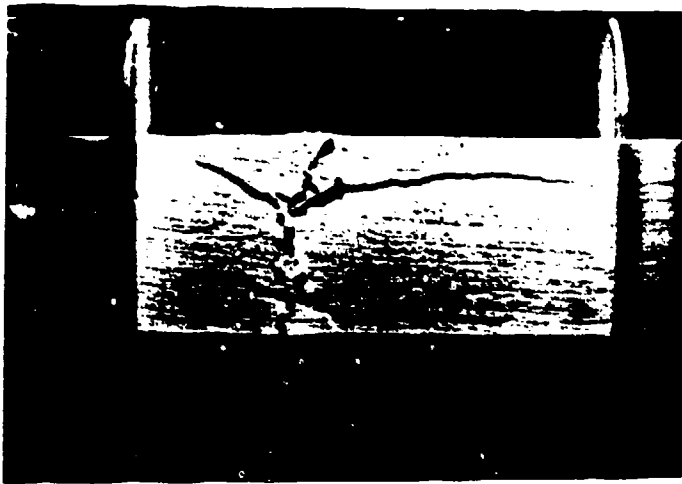
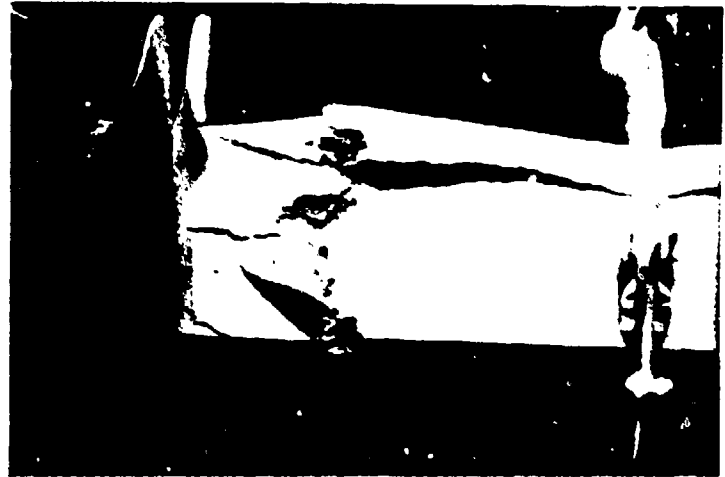
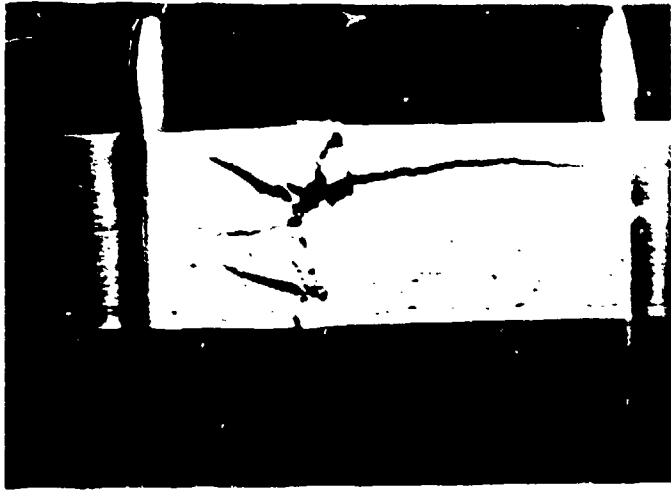


Fig.2.25. continued.

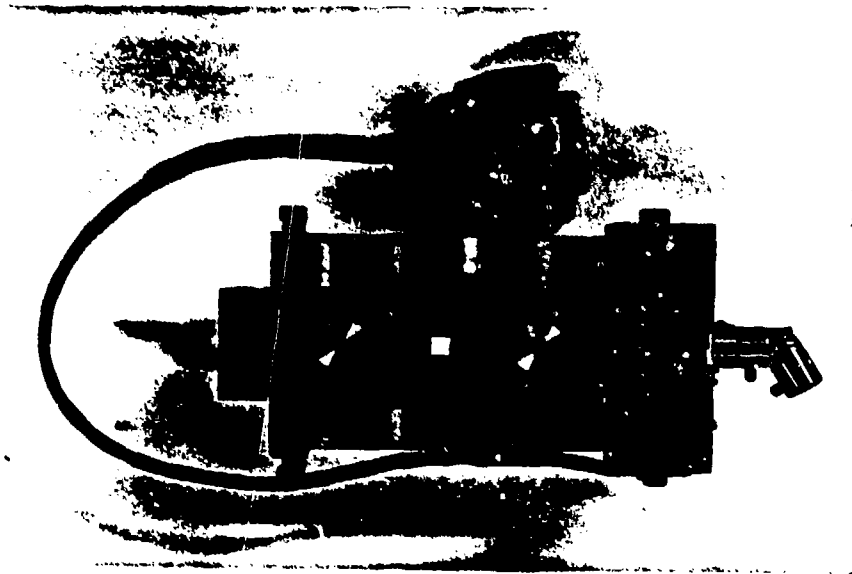


Fig.2.26.The low-stress compression jig used for the in-situ SEM observations.
The cubic specimen is visible in the centre of the jig.

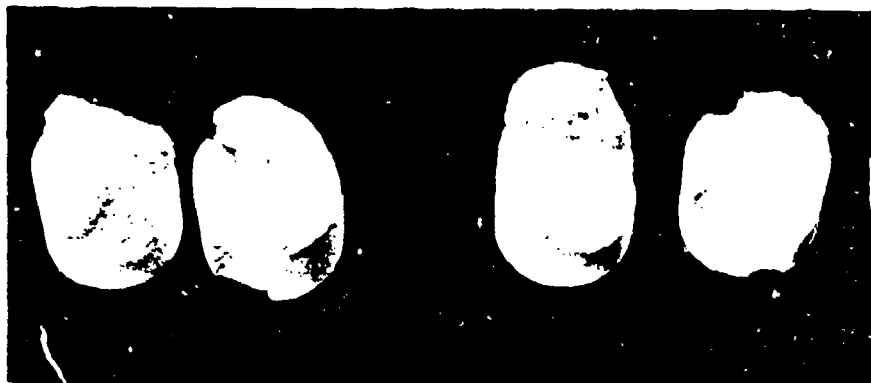


Fig.2.27a.Shear zone formation during
uniaxial compression of Plaster of Paris.
Note the almost complete "cup-and-cone"
type fracture of the specimen on the left.

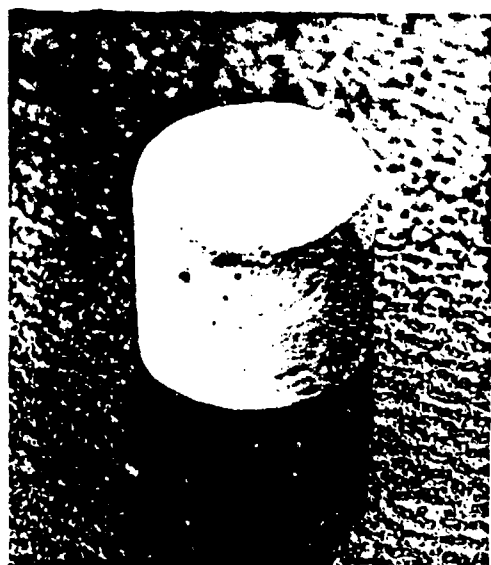
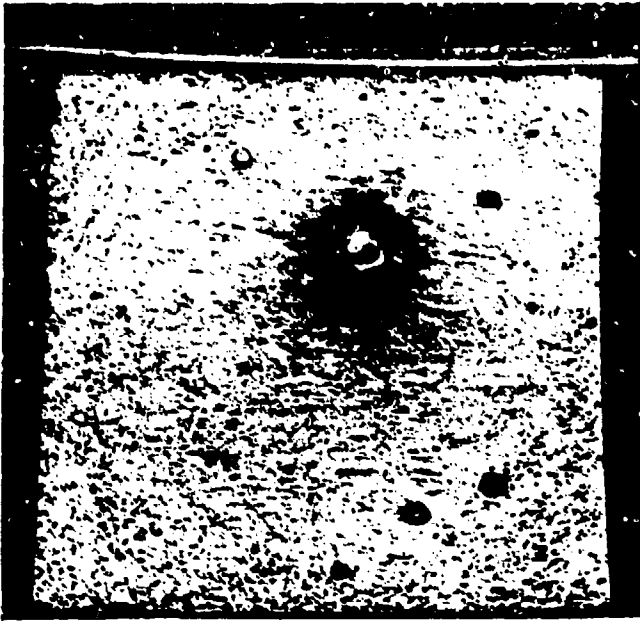


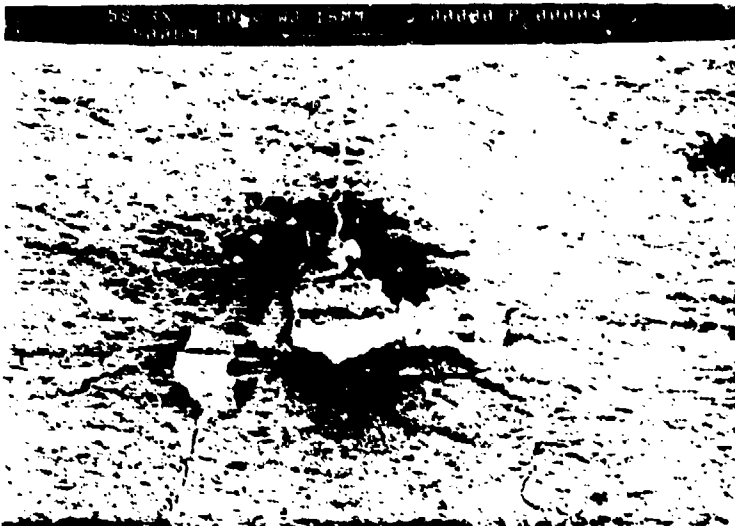
Fig.2.27b.Specimen after initial collapse
in interrupted hydrostatic compression test.
Fracture initiation site is visible near top
surface.



a



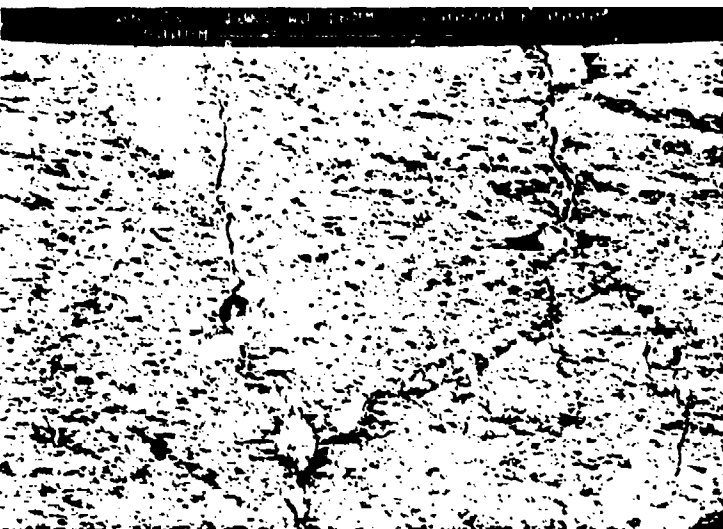
b



c



d



e



f

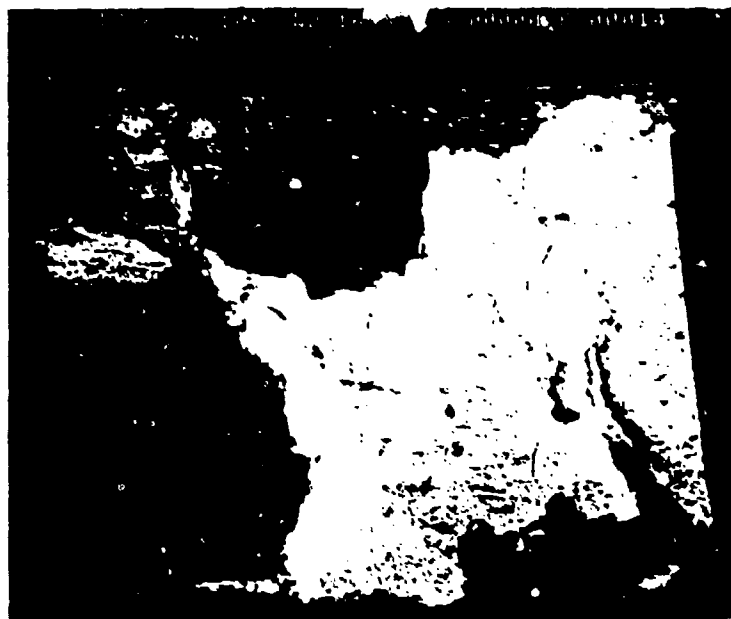
Fig.2.28. In-situ SEM uniaxial compression of Plaster of Paris. (a): unloaded specimen, (b)-(f) after approx 0.5% strain, ((c)-(f): details of (b)), (g): after approx.1.2% strain, (h): after approx.2% strain and (i): after 2.5% strain (near final collapse).



g



h



i

Fig.2.28. continued.

usually associated with the first (fig.2.28). The first crack may or may not continue propagating.

c. On further increase in strain the process enters a stable phase with extensive load cycling during crack propagation, with the load in some cases reaching 95% of fracture load as shown in fig.2.15. During this period longitudinal cracks start nucleating and propagate parallel to the axial (compression) direction as shown in fig.2.25 and 2.28b-g. This is the longest stage and may continue up to strains of $\approx 10\%$. Throughout this stage the specimen has substantial load carrying capacity.

d. The final stage is reached when the longitudinal cracks have propagated stably to the ends of the specimen and slabbing of the specimen has become severe as shown in the last frames of figs.2.25 and 2.28. At this point the load decreases significantly as the specimen loses load carrying capacity.

Due to the nature of the material it was not possible to carry out extensive high magnification SEM examination of the specimens, but it appeared that there was very little interaction between cracks unless they were very close to one another. In many cases new cracks were observed to initiate very close to existing cracks and propagate stably parallel to one another without obvious interaction.

In the case of hydrostatic compression, some specimens were examined after interrupted tests as well as after final collapse. Fig.2.27b shows a specimen from a test interrupted after initial collapse. The fracture initiation region is shown clearly near the top surface marking the presence of a sub-surface pore. Some specimens examined after initial collapse but before reaching a high stress level were observed to have been reduced to a form akin to coarse agglomerate powder. Specimens allowed to reach high stress levels were observed to form high density compacts but of low strength probably due to the presence of air in the specimen.

It is planned to continue the microstructural fractographic analysis in the near future with the aim of clarifying the underlying mechanisms involved in the fracture process.

PLANS FOR FUTURE WORK

It is planned to continue both aspects of the work reported in this report in order to complete the investigations on the micromechanics of the R-curve behaviour of ceramics and the characterization and utilization of CaSO_4 as a model ceramic material.

In the first case it is also planned to carry out K_{Ic} -crack length measurements using short Double Cantilever Beam specimens in-situ in the SEM in order to check and verify the present findings and to investigate the effects, if any, of loading geometry on the R-curve behaviour of the material. A "jig" for this purpose has already been built and is currently being tested. In addition, it is planned to carry out a number of high resolution in-situ experiments in an advanced SEM in order to try to study more clearly the bridges observed between the crack faces.

In the case of the $\text{CaSO}_4 \cdot \frac{1}{2} \text{H}_2\text{O}$ modelling experiments, it is planned to continue and extend the work by investigating the effects of various coherent and incoherent inclusions on the mechanical properties and the fracture characteristics of the material. It is hoped to be able to utilize the material to model the damage mechanics theory developed recently.

In addition to the above, it is planned to initiate investigations on the compressive fracture of structural ceramics both from the microstructural and mechanistic point of view. In this respect, a new "jig" has already been designed and is being built for in-situ SEM compression studies at high stresses in order to study the micromechanics of ceramic compressive fracture. The investigations will encompass a number of different ceramic materials as well as composite ceramics.

ACKNOWLEDGEMENT

The research reported in this document was made possible through the support of the United States Air Force Office of Scientific Research under grant number AFOSR-87-0307.

REFERENCES

1. A G Evans and T G Langdon, "Structural ceramics", Prog. Mater. Sci., 21(1976)171-441.
2. R W Davidge, Mechanical behaviour of ceramics, Cambridge University Press, Cambridge, England, 1979.
3. J F Knott, Fundamentals of Fracture Mechanics, Butterworths, London, 1973.
4. S M Wiederhorn, "Mechanical and thermal properties of ceramics", ed. J B Wachtman, Jr., Nat. Bur. Stand. (US), Special Publ. no. 303, 1969, pp 217-41.
5. R W Rice, R C Pohanka and W J McDonough, "Effect of stresses from thermal expansion anisotropy, phase transformations and second phases on the strength of ceramics", J.Am.Ceram.Soc., 63(1980)703-710.
6. A G Evans and G Tappin, "Effects of microstructure on the stress to propagate inherent flaws", Proc.Br.Ceram.Soc., 20(1972)275-97.
7. Fracture mechanics of ceramics, volumes 1-5, eds. R C Bradt, D P H Hasselman and F F Lange, Plenum, New York, 1974, 1975, 1978, 1980 and 1983.
8. R W Rice, S W Freiman and J J Mecholsky Jr., "The dependence of strength-controlling fracture energy on the flaw size to grain size ratio", J.Am.Ceram.Soc., 63(1980)129-136.
9. R W Rice, S W Freiman and P F Becher, "Grain size dependence of fracture energy in ceramics: I Experiment", J.Am.Ceram.Soc., 64(1981)345-350.
10. R W Rice and S W Freiman, "Grain size dependence of fracture energy in ceramics: II A model for non-cubic materials", J.Am.Ceram.Soc., 64(1981)350-354.
11. T E Adams, D J Landini, C A Schumacher and R C Bradt, "Micro- and macrocrack growth in Alumina refractories", Am.Ceram.Soc.Bull., 60(1981)730-735.
12. N Clausen, B Mussler and M V Swain, "Grain size dependence of fracture energy in ceramics", J.Am.Ceram.Soc., 65(1982)C14-C16.
13. B Mussler, M V Swain and N Clausen, "Dependence of fracture toughness of Alumina on grain size and test technique", J.Am.Ceram.Soc., 65(1982)566-72.
14. B J Pletka and S M Wiederhorn, "A comparison of failure predictions by Strength and Fracture Mechanics techniques", J.Mater.Sci., 17(1982)1247-68.
15. A V Virkar, D K Shetty and A G Evans, "Grain size dependence of strength", J.Am.Ceram.Soc., 64(1981)C56-C57.

16. D B Marshall and B R Lawn, "Residual stress effects in sharp contact cracking : I", J.Mater.Sci., 14(1979)2001-12.
17. D B Marshall, B R Lawn and P Chantikul, "Residual stress effects in sharp contact cracking : II", J.Mater.Sci., 14(1979)2225-35.
18. W Kreher and W Pompe, "Increased fracture toughness of ceramics by energy dissipative mechanisms", J.Mater.Sci., 16(1981)694-706.
19. H Hubner and W Jillek, "Sub-critical crack extension and crack resistance in polycrystalline Alumina", J.Mater.Sci., 12(1977)117-125.
20. Y Fu and A G Evans, "Microcrack zone formation in single phase polycrystals", Acta Metall., 30(1982)1619-1625.
21. A G Evans and K T Faber, "Crack growth resistance of microcracking brittle materials", J.Am.Ceram.Soc., 67(1984)255-60.
22. K T Faber and A G Evans, "Crack deflection processes: I Theory" and "II Experiment", Acta Metall., 31(1983)565-576 and 577-584.
23. R Knehans and R Steinbrech, "Memory effect of crack resistance during slow crack growth in notched Al_2O_3 bend specimens", J.Mater.Sci.Lett., 1(1982)327-329
24. R Steinbrech, R Knehans and W Schaarwachter, "Increase of crack resistance during slow crack growth in Al_2O_3 bend specimens", J.Mater.Sci., 18(1983)265-270.
25. R F Cook, B R Lawn and C J Fairbanks, "Microstructure-strength properties in ceramics: I Effect of crack size on toughness", and "II Fatigue relations", J.Am.Ceram.Soc., 68(1985)604-615 and 616-623.
26. M V Swain, "R-curve behaviour in a polycrystalline Alumina material", J.Mater.Sci.Lett., 5(1986)1313-1315.
27. P L Swanson, C J Fairbanks, B R Lawn, Y-W Mai and B J Hockey, "Crack interface grain bridging as a fracture resistance mechanism in ceramics: I, Experimental study on Alumina", J.Am.Ceram.Soc., 70(1987)279-289.
28. Y-W Mai and B R Lawn, "Crack interface grain bridging as a fracture resistance mechanism in ceramics: II, Theoretical Fracture Mechanics model", J.Am.Ceram.Soc., 70(1987)289-94.
29. R F Cook, C J Fairbanks, B R Lawn and Y-W Mai, "Crack resistance by interfacial bridging: its role in determining strength characteristics", J.Mater.Res., 2(1987)345-356.
30. H Wieninger, K Kromp and R F Pabst, "Crack resistance curves of alumina at high temperatures", J.Mater.Sci., 22(1987)1352-1358.

31. R W Steinbrech and O Schmenkel, "Crack-resistance curves of surface cracks in Alumina", J.Am.Ceram.Soc., 71(1988)C271-C273.
32. C-H Hsueh and P F Becher, "Evaluation of bridging stress from R-curve behaviour for non-transforming ceramics", J.Am.Ceram.Soc., 71(1988)C234-C237.
33. R F Krause Jr., "Rising fracture toughness from the bending strength of indented Alumina beams", J.Am.Ceram.Soc., 71(1988)338-43.
34. A Reichl and R W Steinbrech, "Determination of crack-bridging forces in Alumina", J.Am.Ceram.Soc., 71(1988)C299-C301.
35. S J Burns and M V Swain, "Fracture toughness of MgO-PSZ specimens with K_{R} -curve behaviour from transformation toughening", J.Am.Ceram.Soc., 69(1986)226-30.
36. M V Swain, "R-curve behaviour of MgO-PSZ and its significance to thermal shock", in Fracture Mechanics of Ceramics, vol 6, eds R C Bradt, A G Evans, D P H Hasselman and F F Lange, Plenum Press, New York, 1983, pp355-369.
37. D B Marshall and M V Swain, "Crack-resistance curves in MgO-PSZ", J.Am.Ceram.Soc., 71(1988)399-407.
38. A G Evans and R M Cannon, "Toughening of brittle solids by Martensitic Transformations", overview no. 48, Acta Metall., 34(1986)761-800.
39. D R Clarke, "Microfracture in brittle solids resulting from anisotropic shape changes", Acta Metall., 28(1980)913-924.
40. G Sines, "Rationalised crack growth and time-to-fracture of brittle materials", J.Am.Ceram.Soc., 59(1976)370-371.
41. R W Davidge, J R McLaren and G Tappin, "Strength-Probability-Time (SPT) relationships in ceramics", J.Mater.Sci., 8(1973)1699-1705.
42. T Okada, G Sines and D Green, "Crack origins and microcracking in delayed fracture of Alumina", J.Am.Ceram.Soc., 65(1982)C64-C65.
43. G Sines and T Okada, "Flaws responsible for slow cracking in the delayed fracture of Alumina", J.Am.Ceram.Soc., 66(1983)228-232.
44. H P Kirchner and J M Ragosta, "Crack growth from small flaws in large grains in Al_2O_3 ", J.Am.Ceram.Soc., 63(1980)490-95.
45. G Vekinis and S B Luyckx, "On the relationship between the length of Palmqvist cracks and residual surface stresses in WC-Co", NDT Int., 19(1985)89.
46. J O Outwater and D J Gerry, "On the fracture energy of glass", U S Naval research Laboratory, Report on Contract no. NONR3219(01) (X), August 1966.

47. J A Kies and B J Clark, in Fracture 1969, Proc.2nd Int.Conf.Fracture, ed. P L Pratt, Chapman and Hall Ltd, London, 1969, pp. 483-491.
48. D P Williams and A G Evans, "A simple method for studying slow crack growth", J.Test.Eval., 1(1973)264-270
49. B J Pletka, E R Fuller,Jr. and B G Koepke, "An evaluation of double torsion testing-Experimental", in Fracture Mechanics Applied to Brittle Materials", ASTM STP 678, ed.S W Freiman, 1979, pp 19-37.
50. A G Evans, "A method for evaluating the time-dependent failure characteristics of brittle materials-and its application to polycrystalline alumina", J.Mater.Sci., 7(1972)1137-1146.
51. A G Evans, "Fracture Mechanics determinations", in Fracture Mechanics of Ceramics, vol 1, ed.R C Brandt, D P H Hasselman and F F Lange, Plenum, New York, 1974, 17-48.
52. T A Michalske, M Singh and V D Frechette, "Experimental observation of crack velocity and crack front shape effects in double-torsion Fracture Mechanics tests", in Fracture Mechanics Methods for Ceramics, Rocks and Concrete, ASTM STP 745, eds. S W Freiman and E R Fuller, 1981, pp.3-12.
53. D A Porter and K E Easterling, Phase transformations in metals and alloys, publ. Van Nostrand Reinhold (UK), 1981.
54. T H Mao, P W R Beaumont and W C Nixon, "Direct Observations of Crack Propagation in Brittle Materials", J.Mater.Sci.Lett., 2(1983)613-616.
55. P A Smith, D G Gilbert and A Poursartip, "Matrix cracking of composites inside an SEM", J.Mater.Sci.Lett., 4(1985)845-847.
56. M T Kortschot, P W R Beaumont, W C Nixon and B Bretton, "Fibre-Epoxy composite observed by dynamic SEM", University of Cambridge, Engineering Department, Report No: CUED/C-Mats/TR.136, February 1987.
57. C Cm Wu, R W Rice and P F Becher, "The character of cracks in Fracture Toughness measurements of ceramics", in Fracture Mechanics methods for Ceramics, Rocks and Concrete, ASTM STP 745, eds. S W Freiman and E R Fuller Jr., 1981, pp.127-140.
58. A A Griffith, "The phenomena of rupture and flow in solids", Phil.Trans.Roy.Soc.Lond., A221(1920)163.
59. E Orowan, "Fracture and strength of solids", Rep.Prog.Phys., 12(1949)185.
60. G R Irwin, J.Appl.Mech., 24(1957)361.
61. J C Jaeger and N G W Cook, Fundamentals of Rock Mechanics, Methuen, London, 1969.
62. A A Griffith, "The theory of rupture", Proc. 1st Int. Congress on Applied Mechanics, eds. C B Biezeno and J M Burgers, J Waltman Publ., Delft, Holland, 1924, p 55.

63. S Nemat-Nasser and H Horii, "Compression-induced nonplanar crack extension with application to splitting, exfoliation and rockburst", J.Geophys.Res., 87(1982)6805-6821.
64. F A McClintock and J B Walsh, Proc. 4th U S Nat.Congress Appl.Mech., 2(1962)1015.
65. National Academy of Sciences Report NMAB 404, Committee on Fracture in Compressive Stress Fields, "Fracture in compression of brittle solids", August 1983.
66. M F Ashby and S D Hallam, "The failure of brittle solids containing small cracks under compressive stress states", Acta Metall., 34(1986)497-510.
67. S D Cooksley, "Yield and fracture surfaces of brittle solids", PhD thesis, Cambridge University, 1984.
68. C G Sammis and M F Ashby, "The failure of brittle porous solids under compressive stress states", Acta Metall., 34(1986)511-526.
69. L S Costin, "Damage mechanics in the post-failure regime", Mech.Mater., 4(1985)149-160.
70. L S Costin and C M Stone, "Analysis of triaxial testing using a fracture damage model", Proc.Roy.Soc.Expt.Mech., Spring conference, New Orleans, LA, June 1986.
71. L S Costin, "A microcrack model for the deformation and failure of brittle rock", J.Geophys.Res., 88(1983)9485-9492.
72. S A F Murrell, "A criterion for brittle fracture of rocks", in Rock Mechanics, ed. C Fairhurst, Proc. 5th Symp. Rock Mech., New York, 1963, Pergamon, pp 563-577.
73. S A F Murrell, "The effect of triaxial stress systems on strength of rocks", J.Roy.Astr.Soc., 10(1965)231-281.
74. D Griggs and H Handin, in Rock Deformation, eds. D Griggs and J Handin, chap. 13, Geol.Soc.Am.Mem., 79(1960)347.
75. P Tapponier and W F Brace, "Development of stress-induced microcracks in Westerly Granite", Int.J.Rock Mech.Min.Sci.Geomech.Abstr., 13(1976)103-112.
76. W R Wawersik, "Detailed analysis of rock failure in compression tests", PhD thesis, University of Minn., Minneapolis, USA, 1968.
77. W R Wawersik and W F Brace, "Post-failure behaviour of a granite and diabase", Rock Mech., 3(1971)61-85.
78. W R Wawersik and C Fairhurst, "A study of brittle rock failure in laboratory compression experiments", Int.J.Rock Mech.Min.Sci.Geomech.Abstr., 7(1970)561-575.

79. D K Hallbauer, H Wagner and N G W Cook, "Some observations concerning the macroscopic and mechanical behaviour of quartzite specimens in stiff, triaxial compression tests", *Int.J.Rock Mech.Min.Sci.Geomech.Abstr.*, 10(1973)713-725.
80. M S Paterson, "Experimental rock deformation-The brittle field", Springer, Berlin, 1978.
81. M L Kachanov, "A microcrack model of rock inelasticity, Part 1: Frictional sliding on microcracks", *Mech.Mater.*, 1(1982)19.
82. M F Ashby and C G Sammis, "The damage mechanics of brittle solids in compression", Cambridge University, Engineering Department, Report No: CUED/C-Mats/TR. 144, July 1988.
83. R J Roark and W C Young, "Formulas for stress and strain", 5th edition, McGraw-Hill, New York, 1975.
84. G Sines and M Adams, "Compression testing of ceramics", in *Fracture Mechanics of Ceramics*, vol 3, eds. R C Bradt, D P H Hasselman and F F Lange, Plenum, New York, 1978.
85. G Tappin, R W Davidge and J R McLaren, "The strength of ceramics under biaxial stresses", in *Fracture mechanics of Ceramics*, vol 3, eds. R C Bradt, D P H Hasselman and F F Lange, Plenum, New York, 1978.
86. L J Broutman and R H Cornish, "Effect of polyaxial stress states on failure strength of Alumina ceramics", *J.Am.Ceram.Soc.*, 48(1965)519-524.
87. R Sedlacek, "Investigation of elasticity and strength of ceramics subjected to tensile and compressive loads", Tech.Rept. AFML-TR-68-231, Stanford Research Institute, Menlo Park, Calif., August 1968.
88. M Adams and G Sines, "Determination of biaxial compressive strength of a sintered Alumina ceramic", *J.Am.Ceram.Soc.*, 59(1976)300-304.
89. M Adams and G Sines, "Methods for determining the strength of brittle materials in compressive stress states", *J.Test.Eval.*, JTEVA, 4(1976)383-396.
90. M Adams and G Sines, "Spalling and cracking in Alumina by compression", *J.Am.Ceram.Soc.*, 60(1977)221-226.
91. E Ryshkewitch, *Oxide Ceramics*, Academic Press, New York, NY, 1960, pp.135-142.
92. J Lankford, "Compressive strength and microplasticity in polycrystalline alumina", *J.Mater.Sci.*, 12(1977)791-796.
93. J Lankford, "Compressive microfracture and indentation damage in Al_2O_3 ", in *Fracture Mechanics of Ceramics*, vol 3, eds. R C Bradt, D P H Hasselman and F F Lange, Plenum Press, New York, 1978, pp. 245-255.
94. S Suresh and J R Brockenbrough, "Theory and experiments of fracture in cyclic compression: single phase ceramics, transforming ceramics and ceramic composites", *Acta Metall.*, 36(1988)1455-1470.

95. B R Lawn and M V Swain, "Microfracture beneath point indentations in brittle solids", J Mater.Sci., 10(1975)113-122.

96. A G Evans and T R Wilshaw, "Quasi-static solid particle damage in brittle solids I: observations, analysis and implications", Acta Metall., 24(1976)939-956.

97. M Batzle, G Simmons and R W Siegfried, J.Geophys.Res., 85(1980)7072.

98. A Dinsdale, "Pottery Science: Materials, processes and products", E Horwood, London, 1986.

99. F Singer and S S Singer, "Industrial Ceramics", Chapman and Hall, London, 1962.

100. J F Strawley and B Gross, in Cracks and Fracture, American Society for Testing and Materials Spec. Tech. Publ. No 601, 1976, pp. 559-579.

APPENDIX

The effects of processing parameters and heat treatment on the properties of Plaster of Paris specimens.

The mechanical properties of the Plaster of Paris specimens were found to be very sensitive to small variations in the processing parameters, such as water:powder ratio, curing time, curing temperature and ambient temperature and humidity during curing. In addition, the mechanical properties of the cast specimens were found to be affected by any subsequent heat treatments (such as those that could be used to accelerate curing etc), and testing procedures (such as cycling during bending tests). In order to quantify the above effects and thus establish the optimum processing and measuring procedures to be used to ensure reproducibility, extensive tests were carried out prior to any property measurement. The main results obtained are summarised in this appendix.

The effect of curing duration at room temperature and 40%-60% relative humidity on the Modulus of Rupture in 3-point bending of specimens prepared with a 75% water/powder ratio is shown in fig.A1. It can be seen that a minimum of 7 days' curing is required to ensure that the MOR reaches a constant value and thus all tests were carried out on specimens aged for a minimum of 7 days.

During measurements of the bending strength of the material, it was found that the stiffness and hence the measured Young's modulus increased significantly after cycling between loads of approx. zero to approx. 70% of fracture load, while the MOR measured was found to decrease sharply. This was probably due to the high stress concentrations existing at the roller-sample positions. The Young's modulus was found to reach a constant (plateau) value after about 6 cycles as shown in fig.A.2., which agrees with that obtained by uniaxial compression. The MOR, however, was found to decrease monotonically with cycling, possibly due to microcracking, giving erroneous values after cycling as shown in fig.A.3.

CaSO4: MOR3 vs Cure (75%H2O, No HT)

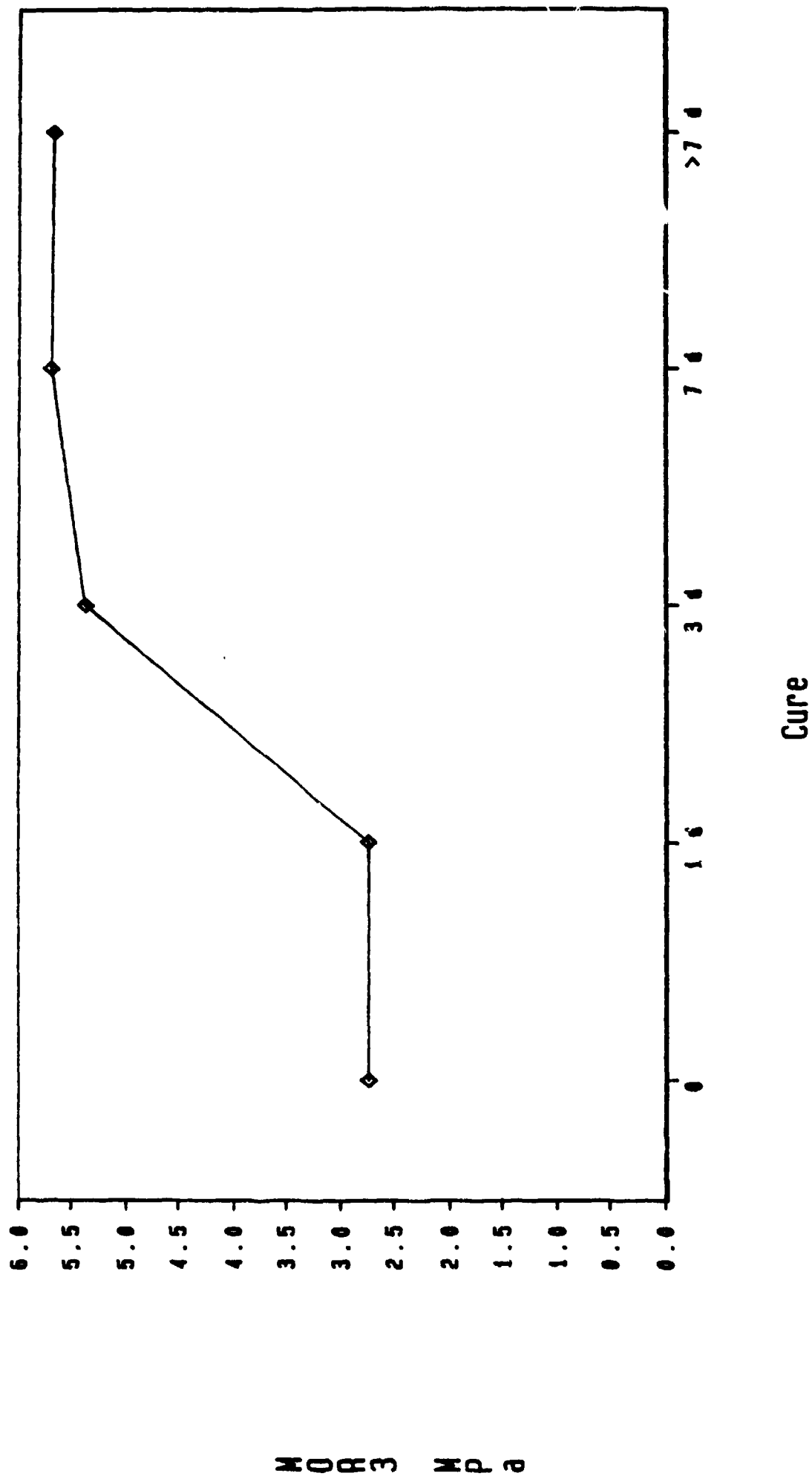
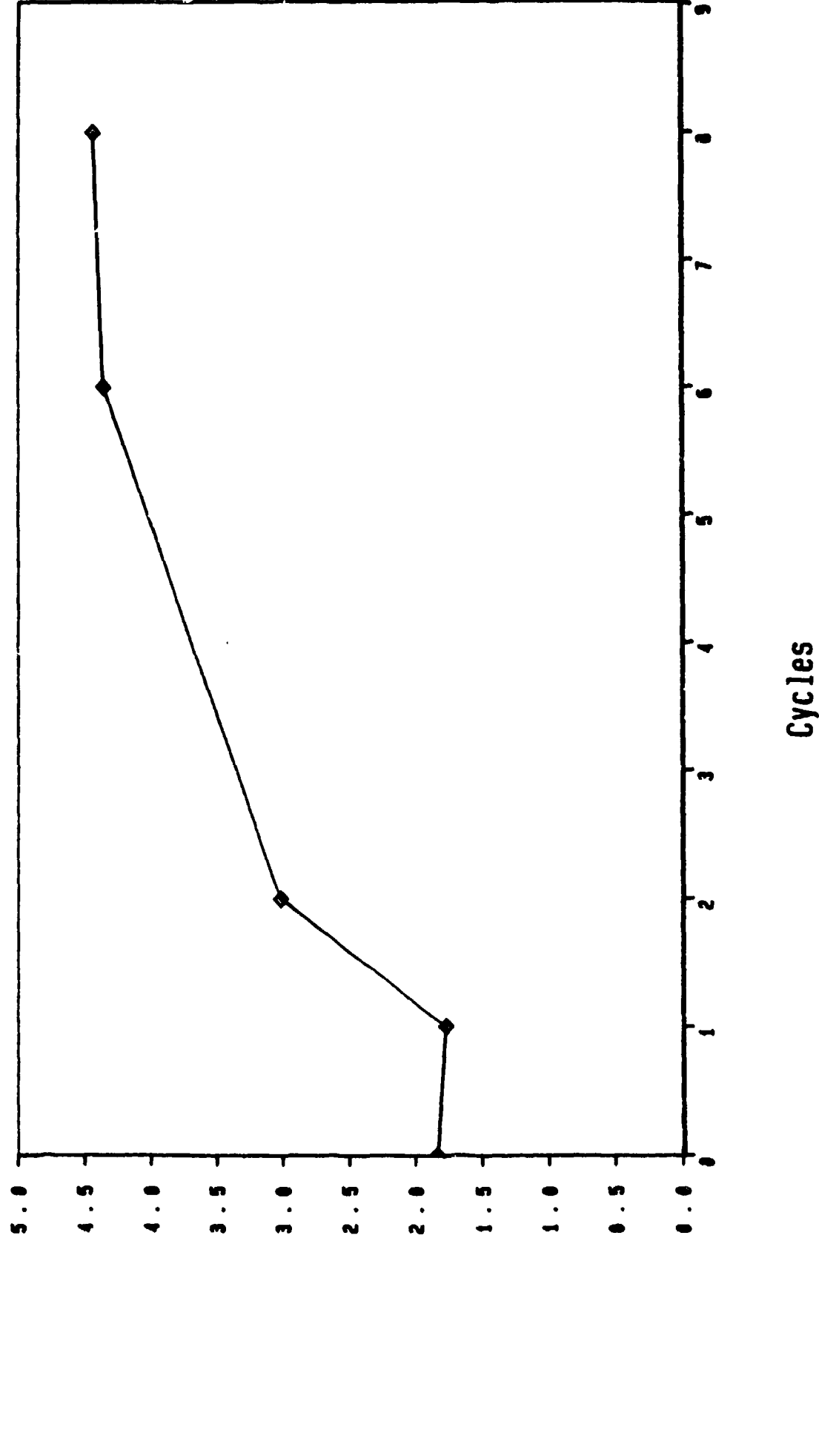


Fig.A1. Modulus of Rupture in 3-point bending as a function of curing time at ambient temperature and humidity.

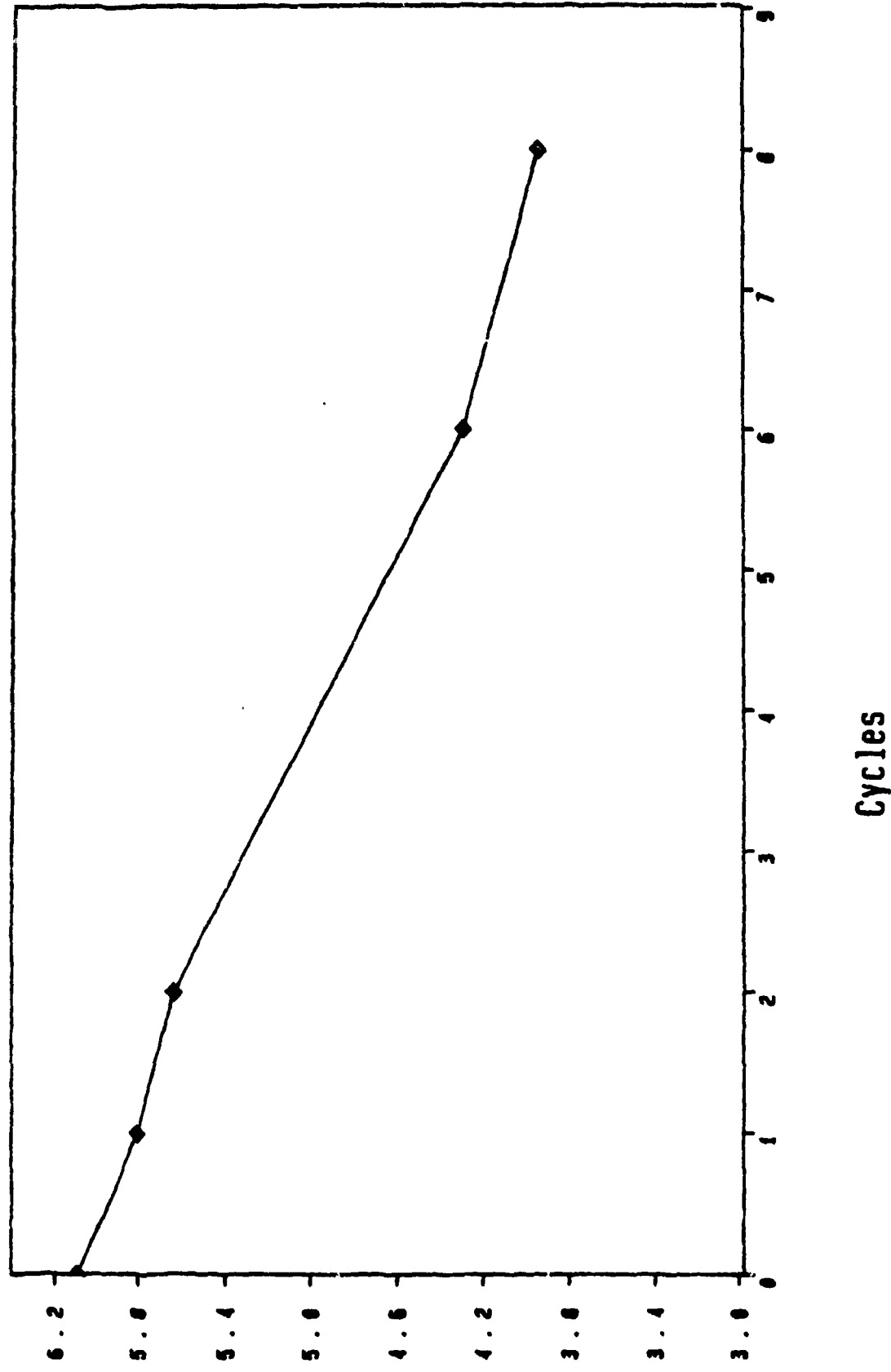
CaSO4: E (MOR4) vs Cycles (62.5% H2O, No HT)



—◇— E [MOR4] 6Pa

Fig.A2. Young's modulus from 4-point bending as a function of number of bending cycles.

CaSO4: MOR4 vs Cycles (62.5% H2O, No HT)



—◇— MOR4 MPa

Fig.A3. Modulus of Rupture in 4-point bending as a function of number of bending cycles.

The influence of subsequent heat treatments on the mechanical properties is shown in figures A.4 to A.8. It can be seen that, although heating at 50°C for prolonged periods does not substantially affect the properties, heat treatments at higher temperatures, even for short periods, have a very pronounced adverse effect on the MOR, Young's modulus, K_{IC} and compressive strength, due to the dehydration of the gypsum crystals. The effect of the water:powder ratio (62.5% to 75%) is also shown in these figures. The general effect of increasing the water content of the mixture is to decrease the mechanical and elastic properties, probably due to the larger porosity content.

From these results as well as other general observations on the influence of environmental factors on the properties of the material, it was decided to use a 62.5% water:powder ratio and cure the specimens firstly in the mould for 24 hours and then for a minimum of 7 days in the laboratory under ambient temperature conditions and relative humidity within the range of 40-60%.

CaSO4: MOR4 and E vs HT (62.5%H2O, 0 cycles)

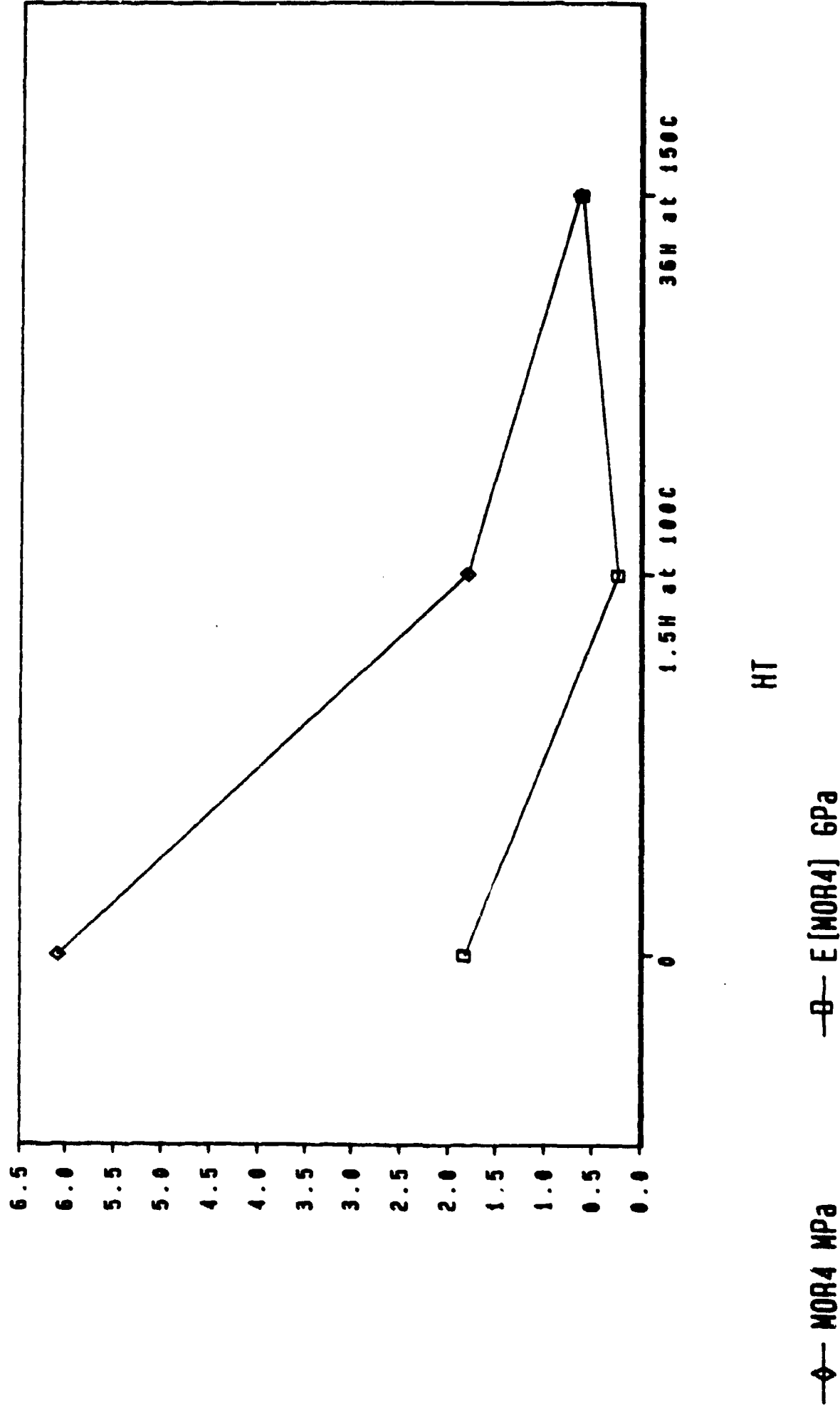


Fig.A4. Modulus of Rupture and Young's modulus in 4-point bending as functions of post-cure heat treatments.

CaSO₄:MOR4 and E vs HT (75%H₂O, 0 cycles)

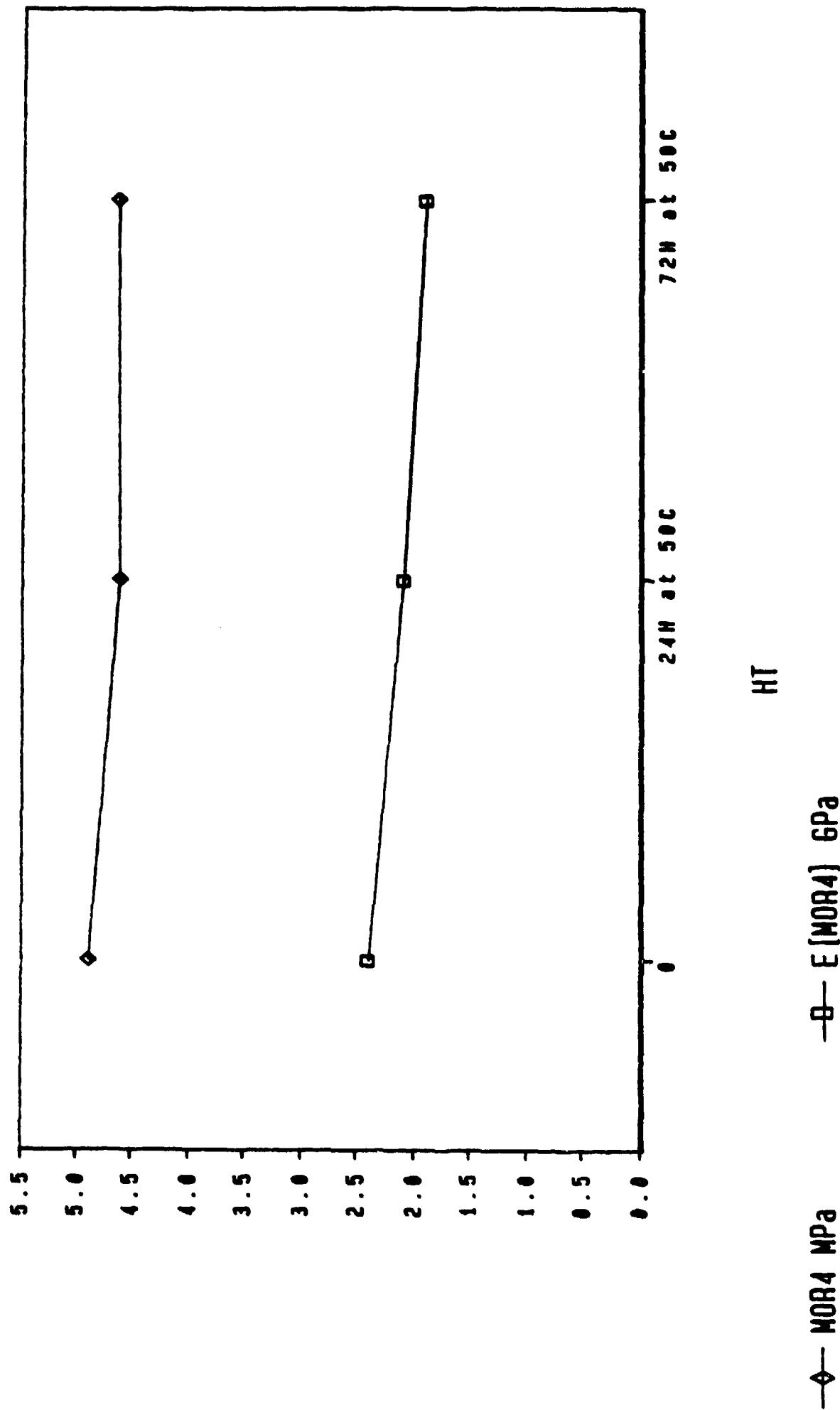
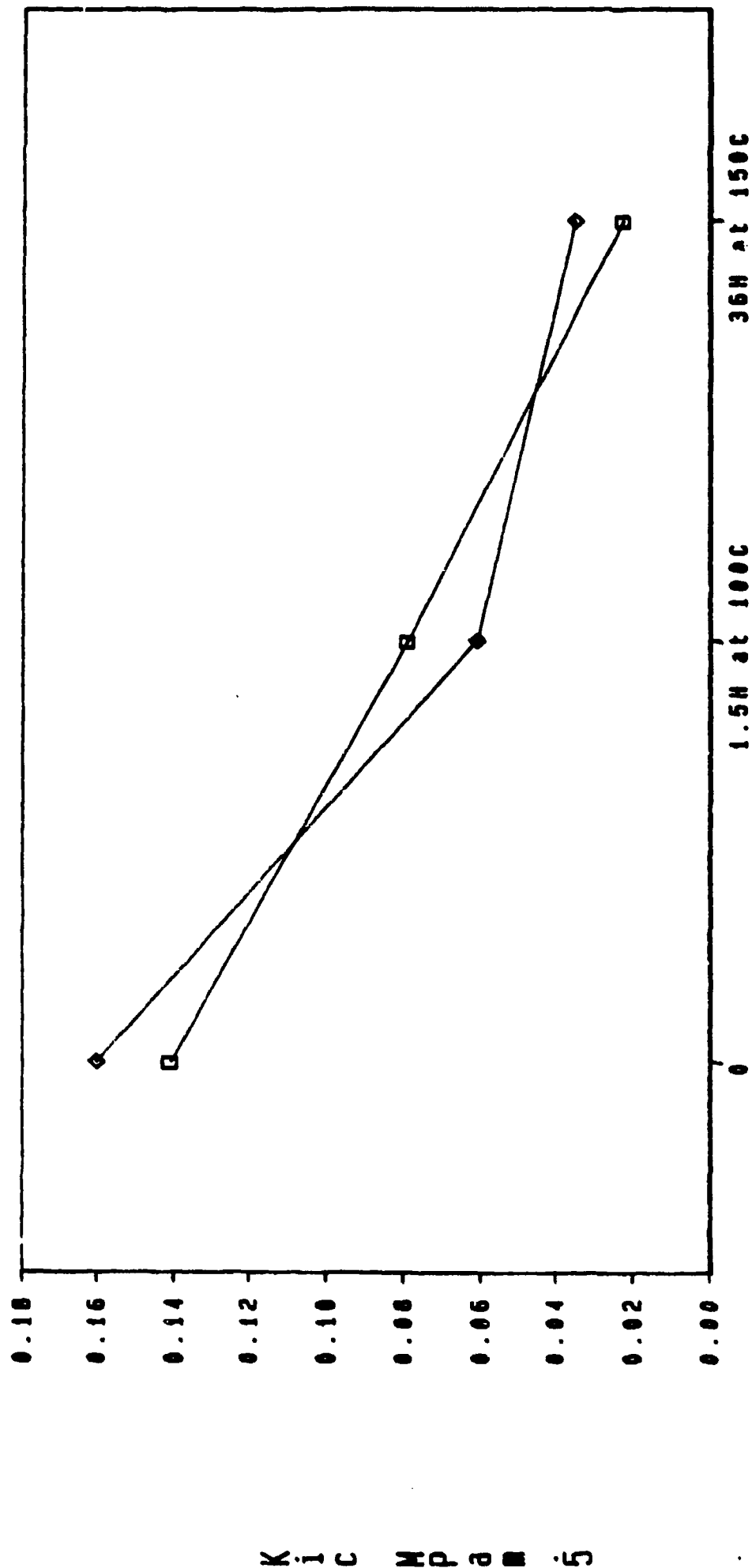


Fig.A5. Modulus of Rupture and Young's modulus in 4-point bending as functions of post-cure heat treatments at 50°C.

CaSO4:KIC vs HT (62.5% and 75% H2O)



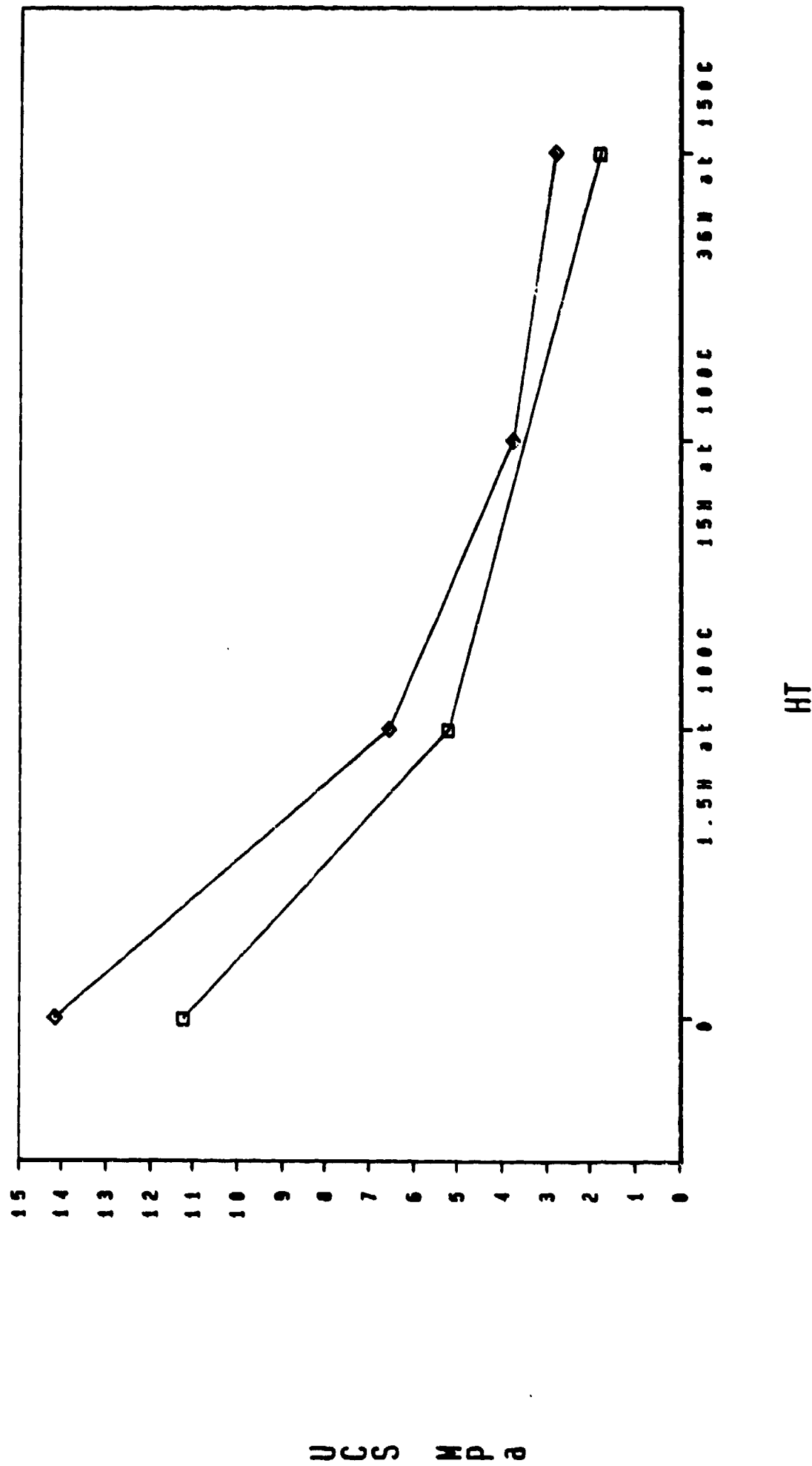
HT

—◇— 62.5

—□— 75

Fig.A6. Fracture toughness of as-sintered Plaster of Paris as a function of post-cure heat treatments.

CaSO4: UCS vs HT (62.5% and 75% H2O)

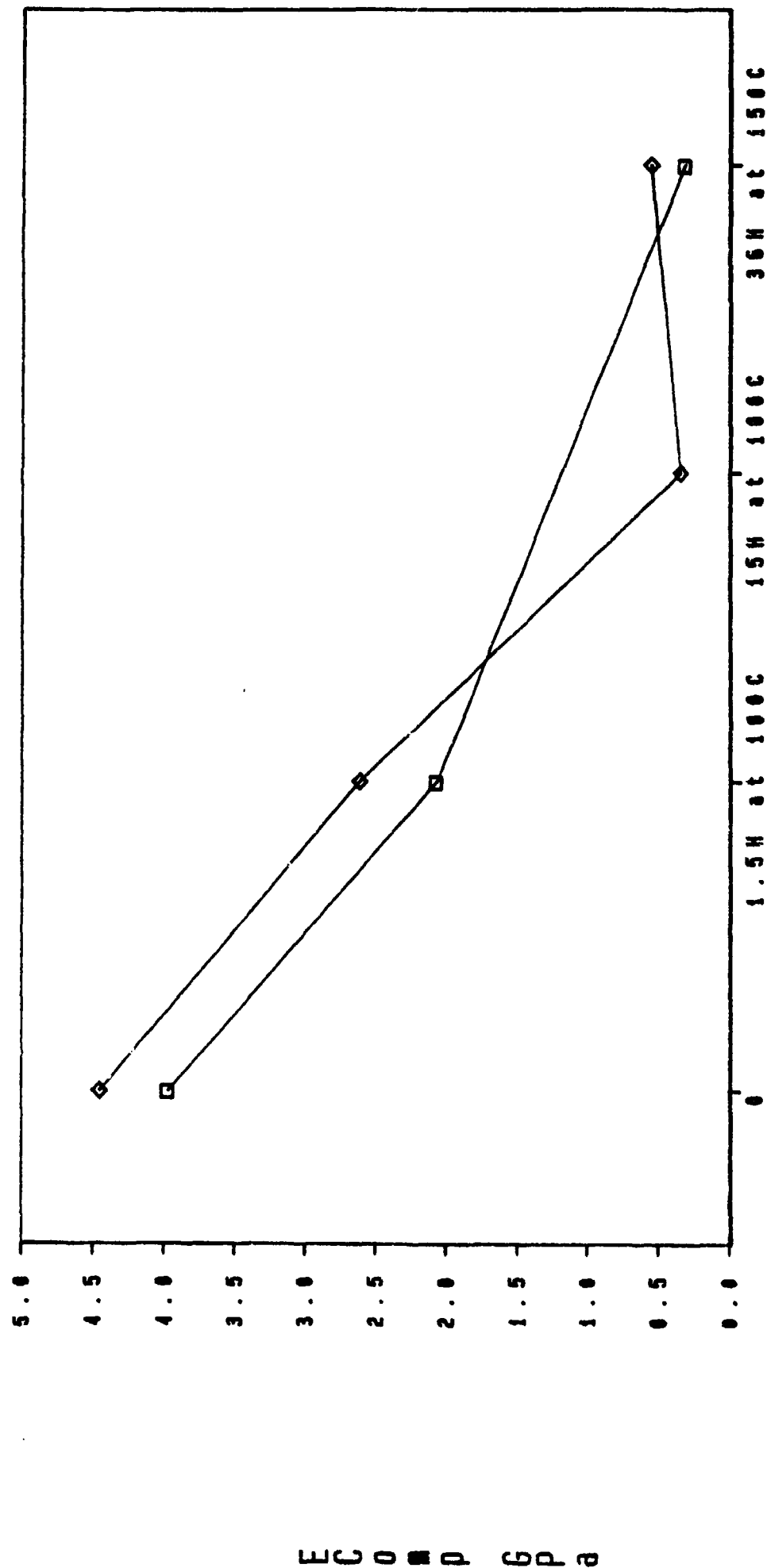


—◇— 62.5

—□— 75

Fig.A7. Uniaxial compressive strength of as-cast Plaster of Paris as a function of water/powder ratio and post-cure heat treatments.

CaSO₄:E(comp) vs HT (62.5% and 75% H₂O)



HT

—◇— 62.5

—□— 75

Fig.A8. Young's modulus in uniaxial compression as a function of water/powder ratio and post-cure heat treatments.